**University of Bath**

**PHD**

# Application of the Interfoam VoF Code to Coastal Wave/Structure Interaction

Morgan, Gerald

*Award date:*
2013

*Awarding institution:*
University of Bath

Link to publication

## Alternative formats
If you require this document in an alternative format, please contact:
openaccess@bath.ac.uk

Copyright of this thesis rests with the author. Access is subject to the above licence, if given. If no licence is specified above, original content in this thesis is licensed under the terms of the Creative Commons Attribution-NonCommercial 4.0 International (CC BY-NC-ND 4.0) Licence (https://creativecommons.org/licenses/by-nc-nd/4.0/). Any third-party copyright material present remains the property of its respective owner(s) and is licensed under its existing terms.

**Take down policy**
If you consider content within Bath's Research Portal to be in breach of UK law, please contact: openaccess@bath.ac.uk with the details. Your claim will be investigated and, where appropriate, the item will be removed from public view as soon as possible.

Download date: 05. May. 2023

# APPLICATION OF THE interFOAM VoF CODE TO COASTAL WAVE/STRUCTURE INTERACTION

Gerald C J Morgan

February 7, 2013

A thesis submitted for the degree of Doctor of Philisophy
University of Bath
Department of Architecture and Civil Engineering
September 2012

**COPYRIGHT**

Attention is drawn to the fact that the copyright of this thesis rests with its author. A copy of this thesis has been supplied on condition that anyone who consults it is understood to recognise that its copyright rests with the author and that they must not copy it or use material from it except as permitted by law or with the consent of the author.

This thesis may be made available for consultation within the University Library and may be photocopied and lent to other libraries for the purposes of consultation.

# ABSTRACT

The validation of the "interFoam" CFD model (part of the OpenFOAM) CFD library is described for a number of wave/structure interaction problems. The background to the research is described, including the reasons for the selection of a new, previously unvalidated CFD code for this purpose. The numerical aspects of the code are briefly reviewed as are some of its additional features including the simulation of porous media. The new wave-generating boundary condition, created as part of this project, is described.

The model is validated for the propagation of waves, including violent, breaking waves, using the widely-known "Dingemans" test case as well as new data for wave and focussed wave group propagation over a bar. The model is validated for wave interaction with surface-piercing structures by examining a test case for focussed wave-group impact on a surface-piercing cylinder with one near-breaking wave and a second, breaking, wave. The model is shown to perform well in these cases without the need for calibration and can therefore be considered to be a valuable design tool. It is also shown that in these cases the model can run sufficiently fast to be practical and economic for use as a design tool.

The model is validated for porous media with a case examining pore-pressure transmission through a porous breakwater. The model performs poorly without calibration, highlighting the high levels of uncertainty in the Darcy parameter, but once calibrated is found to produce accurate results in very reasonable time. A case study of a porous roundhead defence structure is also presented to further reinforce the practical usefulness of the model in design.

# ACKNOWLEDGEMENTS

This project was jointly funded by Great Western Research, the University of Bath and Edenvale Young Associates Ltd., whose financial support is gratefully acknowledged. The author is also indebted to his supervisors, Dr. Jun Zang and Dr. Andrew Heath from the University of Bath, Dr. Deborah Greaves from Plymouth University and Dr. Chris Whitlow from Edenvale Young Associates.

# CONTENTS

# 1 INTRODUCTION

## 1.1 Aims and Scope

This thesis presents four test cases and one case study designed to validate the "interFoam" Computation Fluid Dynamics (CFD) model for various problems in the field of wave/structure interaction. Both the validations and the case study have been conducted in such a way that they not only show the accuracy of the model, but also demonstrate the practicality of the model for use in real design problems.

This research is being conducted with a view to the creation of a detailed model of the process of the breaching of coastal defences and while this thesis only concerns itself with the validation of the model for general wave/structure interaction problems, much of the underlying reasoning for the selection of the modelling approaches used is predicated in requirements related to the simulation of coastal defence breaching.

Presented in this introductory chapter is a general overview of some of the problems in coastal and shallow-water wave/structure interaction and the reasoning behind the selection of the "interFoam" CFD model as a tool to meet the long-term goal of a model of defence breaching. Subsequent chapters cover the equations and numerics of the model, including discussion on the simulation of turbulence and porous media (chapter 2); two test cases validating the model against experimental data of waves propagating over submerged bars (chapter 3); a test case validating the model against experimental data of a breaking focussed wave group interacting with a surface-piercing cylinder (chapter 4); and a test case validating the model for the simulation of a rubble mound breakwater using the Darcy-Forchheimer equations along with a case study showing the qualitative use of this in a practical context (chapter 5). Finally, two chapters cover the conclusions that can be drawn from the research (chapter 6) and suggest a variety of topics for further research that could not be fully explored in the current work (chapter 7).

## 1.2 Coastal Wave Problems

### Wave Propagation

The accurate prediction of wave propagation over arbitrary bathymetry is a significant problem in coastal engineering and a large number of models exist for this purpose. The SWAN model is widely used in the industry for this purpose as are a number of other Boussinesq-equation–based codes such as that of Gobbi & Kirby (1999). These existing codes often have several limitations, however, that render them unsuitable for some problems. Many are unable to cope with discontinuities in the bathymetry or with complex, three-dimensional structures. Other researchers (Lara *et al.* (2008) or Westphalen *et al.* (2007), for example) have applied the Navier-Stokes equations to the problem using various CFD models. These too have often proved problematic with Westphalen *et al.* (2007) finding that the numerical dissipation in some commercial CFD codes made wave modelling extremely difficult.

The problem of wave propagation has practical implications in the design of almost all significant coastal structures as well as beaches and some structures in the near-offshore. The prediction of a wave climate at some location local to a coastal structure or landform is required in order not only to perform accurate assessments of the structural and geotechnical stability of the system but also to perform a wide variety of other assessments such as seakeeping in harbours, water quality or ecological modelling.

### Wave/Structure Interaction

Wave interaction with surface-piercing structures is a problem of some significance. Most practical man-made coastal structures are not fully submerged and are therefore subject to wave interaction and wave impact.

Traditional methods for assessing this type of interaction include the well-known Morrison equation (see e.g. Chadwick *et al.* (2004)) but this has been shown to significantly underestimate the effects in some cases. More complex models for wave diffraction around obstacles have been developed but require significant knowledge and skill to apply in a practical situation. (Zang *et al.* 2006, Zang *et al.* 2009)

CFD models are being increasingly used in this field as they demonstrate their wide range of applicability and flexibility to adapt to struc-

tures with complex three-dimensional geometries. (Greaves 2007, Loehner *et al.* 2007, Losada *et al.* 2008)

An ability to accurately model the processes of wave interaction with surface-piercing structures would not only aid in the structural design of such structures but also with a host of other associated problems such as the design of scour protection schemes, coastal defences and seakeeping.

## Breaking Waves

While rarely considered as a problem on their own, the process of wave breaking adds significant complexity to and wave/structure interaction or wave propagation problem in which it occurs. The processes of wave breaking are discussed extensively in a variety of textbooks (see e.g. Boccotti (2000)) but they have several characteristics that make them extremely difficult to model using simple approaches and that cause significant problems for structural designers.

One of the big problems with the modelling of wave breaking is that of air entrainment. As the crest of a breaking wave spills forwards it can trap a bubble of air. This air bubble will break up and locally change the density, viscosity and pressure of the water. Particular problems can result with surface-piercing structures if air becomes trapped against the face of a bluff structure. In these cases the air has nowhere to go and high pressures can be generated on the face of the structure.

Breaking waves that impact upon structures also bring other problems. In particular if a violently breaking wave "slams" into a structure the effect is very different to that of a much less violent wave of the same frequency. Structural design commonly considers the natural frequencies of resonance of a structure and ensures that loadings which excite these frequencies are both small and infrequent. Breaking waves, however, excite a very large number of frequencies in the structures that they hit, making this design process extremely difficult.

## Porous Media

Coastal structures tend to be made of materials which are (to a greater or lesser extent) porous. There are several good design reasons for this including that the porous materials dissipate much of the energy of waves, resulting in smaller run-ups on the structures. Large, loosely laid stones are also often much cheaper than an equivalent volume of non-porous material (e.g. concrete).

This poses a problem for modelling as there is no good, widely accepted methodology for modelling wave transformation within an arbitrary porous medium. There are two approaches: direct modelling, in which each individual stone and the gaps between them are modelled explicitly; and the Darcy-Forchheimer equations.

Direct modelling is occasionally possible in cases where the stones and gaps between them are very large and very regular. It is the most likely to give the correct answer but it has a significant practical drawback: it is very computationally expensive. As each gap has to be modelled, probably with several cells across it in CFD, the model scale is very significantly reduced and very fine grids become necessary.

The Darcy-Forchheimer equations are widely used in geotechnical engineering for the modelling of flow through soils however they are little validated for very coarse materials and rely on several assumptions (steady, non-rotational flow) which will normally make them unsuitable for use in wave-structure interaction calculations without careful calibration.

## 1.3 The Model

### Selection Criteria

As will be shown in the following chapters, wave propagation and interaction with structures is an extremely complex, three-dimensional process and any model will have to meet a wide range of criteria if it is to be able to realistically model the air entrainment and complex fluid movements associated with breaking waves.

From a preliminary review of the literature, the following key requirements were determined for a numerical model of the process. While it is clear that a model that fulfils all of the following criteria is some way off, both in terms of theory and in terms of computational practicality, it is useful to consider the requirements of a "perfect" model.

In the selection of the model consideration was also given to the features that would be required if this model were to fulfil its proposed long-term aim of informing the dynamic simulation of the breaching process.

#### Three-dimensional hydraulics

In both real-world and many laboratory scenarios waves are observed interacting with complex structures which cannot be readily simplified into

a two-dimensional problem. An example of this is the cylinder case discussed in chapter 4. A requirement for a fully three-dimensional model which can represent flows travelling around arbitrary, complex three-dimensional structures is therefore indicated. With currently known techniques, only physical modelling or a Navier-Stokes–based three-dimensional model with appropriate surface-capturing and turbulence schemes would be appropriate to meet this criterion.

Additionally, Allsop *et al.* (2007) remarks that many observed breaches occur at transitions in defences, indicating that asymmetry of geometry and therefore three-dimensional flow is a common critical case in real-world breaching scenarios.

**Direct simulation of water waves**

Wave impact can have an important effect on the initiation of damage to coastal defences (and hence their breaching) as has been shown by physical tests by van der Meer *et al.* (2006). Outside of direct physical modelling, there are two approaches by which water waves may be simulated: a direct solution of the hydraulics within each wave, or a solution for the parameters of the waves such as wavelength, $L$, and wave height, $H$, which are then superimposed on a solution for the mean water level. In cases for which an embankment or wall is only just overtopping or which feature wave breaking or wave impact, this latter method may not correctly simulate the overtopping or transformation behaviour of the waves. A direct simulation of the water waves is therefore required to correctly predict wave processes in very shallow water or in cases where water is overtopping or breaching a coastal defence.

**Accurate contact stresses**

The contact stress between the water and the structures with which it interacts is one of the critical values which will determine the nature of the wave interaction, the response of the structure and allow for predictions of defence failure. The hydraulic model must be able to calculate this accurately. Not only will this value affect the potential for erosion of an embankment, but it is also critical to slope stability, structural and overturning calculations. Additionally, it is likely that the value of the contact stress will be highly localised in both space and time: in a violent wave climate, the stress on a coastal structure will vary greatly between the top and bottom of a wave and in a structure with complex geometry and at transitional points, stress concentrations are likely to form.

**Close coupling of hydraulic and geotechnical models**

While the focus of many post-failure investigations is to find *the* failure mechanism, the majority of real failures are as a result of a combination of failure mechanisms (Allsop *et al.* 2007, Seed *et al.* 2008). For example, a piping or erosion failure may not be sufficient to compromise the defences alone, but may sufficiently weaken an embankment for a slope stability failure to occur. In order to accurately capture this combination of phenomena, the model must simulate the effects of all failure modes in parallel and allow these simulations to interact when scenarios in which breach initiation occurs have been identified. A choice of model which allows the hydraulics to be readily coupled to other models of geotechnical or structural processes would be extremely beneficial.

## Choice of Model

A variety of hydraulic models were considered, including well-known commercial codes such as CFX as well as more readily-available codes such as the Gerris model and the OpenFOAM library. Each model is described below[1].

CFX is a commercial CFD package made by ANSYS Ltd. It is widely used across a broad range of fields, including the fields of civil and marine engineering. However, previous work on CFX by Westphalen *et al.* (2007) indicated that accurate simulation of water waves, except on very fine grids, could be problematic, with the code requiring meshes beyond the limits of modern computer systems for even a relatively simple model.

Gerris is a free, three-dimensional, open-source hydraulic model using an octtree grid concept and the non-viscous, Euler equations (Popinet 2003). While it does not have a large number of users, it has been used in coastal and offshore simulations (Popinet & Rickard 2007). Initial testing with this solver indicated that the solver's free-surface capabilities were still at an early stage, however, and might not be suitable for the simulation of breaking waves.

The OpenFOAM library is a free, open-source library for continuum mechanics developed by OpenCFD Ltd. which comes with a wide variety of solvers specialised for a wide variety of problems, including a

[1]This assessment and comparison of the various available models was undertaken in late 2008 and the comments on each model are representative of this time period. It is expected that some or all of the issues raised here may have been resolved during the course of this work.

series of solvers specialised for free-surface modelling (Weller *et al.* 1998, Rusche 2002). Additionally, examples were available of the close coupling of the hydraulic model with a linear-elastic structural model, although this was at a very early stage of development (Olivier & Dumas 2009).

## OpenFOAM

Based on this preliminary study, it was decided to use OpenFOAM. At different stages of this work, different versions of the library were used. The initial simulations were performed with version 1.5-dev, while the later simulations were performed with version 1.6 or 1.7.1..

This library was selected, in part, because the associated "interFoam" family of multi-phase hydraulic models met all of the hydraulic modelling criteria given above, and because their design will, after suitable validation, allow them to be closely coupled to a geotechnical model without significant alteration. Additionally, their free, open-source nature allows the program to be run indefinitely, on any machine or any number of machines, without additional cost—a feature that is not only useful to this study, but may also significantly enhances the model's practicality for use in real engineering problems.

The OpenFOAM library is an extensive collection of code, written in the C++ programming language. It is designed to run on UNIX or UNIX-like systems such as Linux. A large number of CFD solvers are provided with this library solving for a broad range of parameters using a wide selection of methods. As they are all based on the same fundamental code, they have many features in common. All use a three-dimensional, unstructured finite-volume mesh and have the same selection of matrix solvers and discretisation schemes. The different solvers and discretisation schemes can be selected on a per-operation basis at run-time. Additionally, all of the models can take advantage of MPI (message passing interface) parallelism, allowing single models to be run over multiple cores, processors and machines without modification.

The "interFoam" solvers have several additional features in common (OpenCFD Ltd. 2008):

- The solvers use the Volume-of-Fluid (VoF) method for calculating interfacial flows, taking into account surface tension.

- They are dynamic, solving for unsteady, time-varying flow.

- They use the PISO algorithm for solving the Navier-Stokes equations.
- Either Reynolds-Averaged Stress (RAS) or Large Eddy Simulation (LES) turbulence formulations may be used, or turbulent flow may be neglected altogether.

These concepts are discussed in greater depth in section 2.1.

The various interFoam models that were used as part of this study, their version numbers and brief descriptions are listed in table 1.1.

## 1.4 Test Systems

It is important, in the assessment of the model's feasibility for use in engineering design, to consider the time taken to complete simulations. The simulation time, along with the cost of hardware and software licenses, is one of the key factors that determines whether a model can be practically applied in a design problem. This time period, however, is continually reducing every year as newer, faster and more computationally efficient computer systems become available. It is therefore important to describe the computer systems used to perform the model runs described in the following chapters, so that the quoted run-times can be related to more modern computer systems in the future.

Two different computer systems were used in the tests. In order to ensure that the model was feasible for use by small companies and individuals, the test systems were constructed using commodity components and were generally inexpensive.

Test system A was constructed in 2008. It was a single computer using an Intel "Core2"-based quad-core processor and 8 GiB of RAM. This was used for the computations shown in chapter 3.

Test system B was constructed in 2009. It was a "micro-cluster" of three computers with one AMD "Phenom II X4" quad-core processor and 4 GiB of RAM each. The systems were linked using a 1000baseT Ethernet network, but most computations on these systems were not parallelised across more than one machine. This was used for the computations shown in chapters 4–5.

| Model name | 1.5-dev | 1.6 | 1.7.1 | Description |
|---|---|---|---|---|
| interFoam | X | X | X | Basic model solving the unsteady, incompressible Navier-Stokes equations for two phases using the VoF method. |
| rasInterFoam | X | | | As interFoam, but with RAS turbulence modelling. This functionality was incorporated into the standard interFoam from v. 1.6. |
| porousInterFoam | * | * | X | As interFoam, but incorporating flow through porous media. * - This was initially implemented by hand, following the procedure described in Hafsteinsson (2009), but a standard solver of this name was included from v. 1.7 and this was then used in preference. |
| multiphaseInterFoam | | | X | An implementation with an arbitrary number of fluid phases. Used for simulations in which soil was modelled as a Herschel-Bulkley fluid. |

Table 1.1: Table showing the various interFoam-based models used in this work and their versions.

# CODE SPECIFICATION 2

## 2.1 Governing Equations

### Navier-Stokes Equations

In general, the motion of a fluid can be described by the Navier-Stokes equations. These equations are well-known and can be found in many textbooks. Only a summary is given here. A more complete discussion can be found in, for example, Temam (2001) or Tu *et al.* (2008).

Formulated for an incompressible fluid, the Navier-Stokes equations can be written as a mass conservation equation

$$\frac{\partial \rho}{\partial t} + \nabla \cdot \left( \rho \underset{\rightarrow}{U} \right) = 0, \tag{2.1}$$

and a momentum conservation equation

$$\frac{\partial \rho \underset{\rightarrow}{U}}{\partial t} + \nabla \cdot \left( \rho \underset{\rightarrow}{U} \underset{\rightarrow}{U} \right) = -\nabla p + \nabla \cdot \boldsymbol{\tau} - \underset{\rightarrow}{g} \cdot \underset{\rightarrow}{x} \nabla \rho + S \tag{2.2}$$

in which $S$ represents additional momentum source/sink terms to model additional processes such as flow through porous media (see section 2.4).

Conventionally, the Newtonian fluid assumption is made, assuming a purely linear relationship between the stress tensor, $\boldsymbol{\tau}$, and the strain rate, $\dot{\boldsymbol{\epsilon}}$:

$$\boldsymbol{\tau} = \mu \dot{\boldsymbol{\epsilon}} \tag{2.3}$$

in which $\mu$ is the dynamic viscosity of the fluid (some texts give this as $\eta$, e.g. Jeong *et al.* (2009)).

This strain rate can be expanded into a function of the fluid velocity and the viscosities which, for a Newtonian fluid, are material constants, giving:

$$\boldsymbol{\tau} = \mu \left[ \nabla \underset{\rightarrow}{U} + (\nabla \underset{\rightarrow}{U})^T + \left( \frac{\nu}{\mu} - \frac{2}{3} \right) (\nabla \cdot \underset{\rightarrow}{U}) \boldsymbol{I} \right] \tag{2.4}$$

in which $\nu$ is the kinematic (bulk) viscosity of the fluid. (de Medina 2008)

When considered in three dimensions the Navier-Stokes equations is a set of four equations with four unknowns: fluid pressure and each component of fluid velocity. The solution of these equations using numerical methods on computers is known as computational fluid dynamics (CFD).

## Discretisation Approach

The Navier-Stokes equations describe fluid motion at a point. In order to use them to simulate real cases, it is usually necessary to model some large domain. Two basic approaches for solving the equations over a domain are popular: Eulerian methods, where the fluid moves through a fixed "mesh" of solution locations and Lagrangian methods where the solution locations move with the fluid. Both approaches have advantages and disadvantages.

Eulerian solutions are often easier to formulate and do not require complex treatments on boundaries. They are a well understood problem and there is a wealth of experience already available within the field of coastal and fluvial engineering, giving them a slight advantage for practical applications. The well-known "finite difference", "finite element" and "finite volume" methods are predominantly Eulerian in character. (Kothe 1999)

Lagrangian solutions, while normally easier for the modeller (due to the absence of the complex, and often error-prone meshing step) can be harder to formulate (Schlatter 1999) and can occasionally present problems on boundaries (Morgan 2008). Many Lagrangian solutions require frequent "re-meshing" as the solution points deform to a degree that some areas of the domain do not have sufficient points to accurately resolve the flow behaviour (Sbalzarini *et al.* 2006). Also, while many modern Smoothed Particle Hydrodynamics (SPH) codes are currently better designed for modern hardware than available Eulerian codes, it is theoretically more straightforward to optimise Eulerian solutions than Lagrangian solutions on modern computer hardware due to the fixed connectivity of Eulerian solutions. Examples of Lagrangian approaches include the Particle-In-Cell (PIC) method (Harlow & Evans 1955, Harlow *et al.* 1956, Harlow 1957) and the SPH method (Dalrymple & Rogers 2006, Gomez-Gesteira *et al.* 2010).

For these reasons the Eulerian, finite volume (FV) method was selected as the tool of choice for this problem, and consequently, this is the approach that will be discussed here.

In the FV method the computational domain is divided into a number of volumes (or cells) which are assumed to be small relative to the scale of the fluid motions being studied. The equations to be solved are integrated over a control volume and the Gauss divergence theorem is then used to transform the divergence terms in the equations into surface integrals over the volume's boundary. These surface integrals are then computed as the sum of the values on the cell faces. (Kothe 1999)

## Solution Approach

It is difficult to solve the incompressible form of the Navier-Stokes equations directly, despite the determinate system of equations and unknowns. There are two well-known approaches to solving the system, known as "SIMPLE" and "PISO" as well as several other, less common variants and schemes.

The Semi-Implicit Method for Pressure-Linked Equations (SIMPLE) approach is widely used and is described in detail in many publications, e.g. Juretic (2004). There are four basic steps which are iterated for each time-step until a suitable convergence has been achieved:

1. Solve the momentum equation to calculate the velocity field using best-guess initial values. Under-relaxation is normally used. This step is sometimes referred to as the "Momentum Predictor" step.

2. Use the predicted velocities to solve the pressure equation.

3. Calculate a new set of mass-conservative fluxes for the cell faces.

4. Calculate the new best-guess velocity field from the new set of face fluxes. Once the process has converged, this velocity field will satisfy both mass and momentum conservation.

After each iteration has completed, additional equations, such as turbulence models or multi-phase models may be solved using the updated velocities and cell-face fluxes.

The PISO (Pressure Implicit with Splitting of Operators) approach was proposed by Issa (1985). Here, each time-step is solved in three steps, with iteration only required for the second and third steps:

1. The momentum equations are optionally solved using a best-guess pressure field to produce a best-guess velocity field. [1]

[1] Issa (1985) notes that while this "momentum predictor" step is formally required for the method, many applications do not require it, and can proceed straight to the second step using the previous time-step's velocity field.

2. The best-guess velocities are used to solve the pressure equation.

3. The velocity field is corrected using the new pressures.

Within each time step, additional equations for multi-phase flow are solved before the PISO algorithm, while other equations, such as turbulence models, are solved afterwards.

There appears to be little guidance in the literature regarding which of these two approaches is more suitable for the type of problems under consideration here, but work on this is currently under investigation by other researchers (Paterson 2009). For the present, the models presented in this research will use the PISO scheme as that is the current scheme in use within the interFoam models.

## Multi-phase Modelling

Using the Navier-Stokes equations to model free-surface flow, such as that in rivers and oceans, requires some additional treatment. There are a wide variety of approaches for this, which are often tied to the discretisation approach used for the domain: for example, many particle methods such as PIC and SPH have their domain move along with the fluid and therefore model the free-surface implicitly as part of their discretisation approach.

For purely Eulerian methods, a common approach is to make the "one-fluid" assumption in which a number of different fluids are modelled as a single fluid with rapidly varying material properties. (Kothe 1999) In order to do this, some form of marker is required to denote the distribution of the phases through the domain or the position of the free surface. The material properties ($\rho$, $\mu$, $\nu$, etc.) then become functions of this marker variable.

The marker variable can take a variety of forms, but a common and widely-used approach is the Volume-of-Fluid (VoF) method.

In the VoF method the marker variables are known as "volume fractions". The volume fraction, $\alpha_i$, indicates the proportion of a cell which is filled with fluid $i$. $\alpha_i$ is strictly bounded: $0 \leq \alpha_i \leq 1$. In a simulation with $N$ fluids, $N-1$ volume fractions are required to complete the model, as $\alpha_N = 1 - \sum_{i=1}^{N-1} \alpha_i$, $\sum_{i=1}^{N} \alpha_i = 1$.

In a conventional VoF solution of the Navier-Stokes equations the fluid properties $\rho$, $\mu$ and $\nu$ are substituted with weighted averages:

$$\rho = \sum_{i=1}^{N} \alpha_i \rho_i, \tag{2.5}$$

$$\mu = \sum_{i=1}^{N} \alpha_i \mu_i, \tag{2.6}$$

$$\nu = \sum_{i=1}^{N} \alpha_i \nu_i, \tag{2.7}$$

and the distribution of the volume fractions is solved using additional equations of the form

$$\frac{\partial \alpha_i}{\partial t} = \underset{\rightarrow}{U} \cdot \nabla \alpha_i \tag{2.8}$$

(Ubbink 1997).

## Turbulence Modelling

The flows that occur in natural and complex mechanical processes are often turbulent flows: exhibiting fluctuations in velocity and fluid behaviour over a small area in an apparently random manner. Directly solving for these turbulent fluctuations requires meshes which are so small as to be impractical for most problems. Because of this, the turbulent nature of the flow is often either neglected or, in situations where the turbulence effects are significant, modelled with a simplified model.

While there are a wide variety of models for the turbulent fluctuations, only the Reynolds-Averaged Stress (RAS) models[2] will be discussed here. While Large Eddy Simulation (LES) models are also commonly used, they have much more stringent meshing requirements than the RAS models, leading to even greater computational expense. The investigation of the use of LES turbulence modelling for breaching problems has been left for future work.

In RAS models, the main variables in the Navier-Stokes equations are decomposed into a time-averaged component and a turbulent fluctuation component:

$$\underset{\rightarrow}{U} = \left\langle \underset{\rightarrow}{U} \right\rangle + \underset{\rightarrow}{U_t} \tag{2.9}$$

$$p = \langle p \rangle + p_t \tag{2.10}$$

$$\boldsymbol{\tau} = \langle \boldsymbol{\tau} \rangle + \boldsymbol{\tau_t} \tag{2.11}$$

in which the angle-brackets represent the time-averaging and the $t$-subscripted terms, the instantaneous fluctuations. If these equations are

[2]The combination of the Navier-Stokes equations with RAS turbulence modelling is sometimes referred to as a Reynolds-Averaged Navier-Stokes (RANS) simulation.

combined with the Navier-Stokes equations, however, the number of unknown variables is greatly increased, for no gain in the number of equations. Further, an additional "stress" term is produced, known as the Reynolds stress. This stress is extremely difficult to quantify as the small turbulent flows that induce it cannot be directly modelled without unacceptable computational expense and are themselves highly dependant on its value. A full treatment of these equations is not necessary here. George (2009) expands further upon the Reynolds stress term and gives an outline of the practical problems of turbulence modelling.

One approach to the concept of Reynolds stress is to treat it similarly to the conventional stress term and model it using a viscosity, as in equation 2.4. This leads to the concept of the eddy viscosity, $\mu_t$:

$$\boldsymbol{\tau} = \mu_t \left[ \nabla \underset{\rightarrow}{U} + (\nabla \underset{\rightarrow}{U})^T + \left( \frac{\nu_t}{\mu_t} - \frac{2}{3} \right) (\rho k) \boldsymbol{I} \right] \tag{2.12}$$

The various turbulence models in common use essentially serve to calculate this $\mu_t$ value. Two common RAS models are described below. It can be seen that these equations, which must be solved additionally, alongside the Navier-Stokes equations, are very complex and impose additional requirements on the shape of the computational mesh. In cases where turbulence does not play a significant effect or its effect cannot be reliably estimated, even this form of turbulence modelling can probably be neglected altogether in order to minimise needless computational expense within the model.

### $k$-$\epsilon$ model

The $k$-$\epsilon$ model parametrises the turbulence problem into two variables, the turbulent kinetic energy, $k$, and the turbulent dissipation rate, $\epsilon$. From these, the eddy viscosity is calculated using

$$\mu_t = \frac{c_\mu f_\mu \rho k^2}{\epsilon}. \tag{2.13}$$

The $k$ and $\epsilon$ variables each have a convection-diffusion equation[3]:

$$\frac{\partial \rho k}{\partial t} + \nabla \cdot \left( \rho \underset{\rightarrow}{U} k - \left[ \mu + \frac{\mu_t}{\sigma_k} \right] \nabla k \right) = \boldsymbol{\tau_t \epsilon} - \rho \epsilon + \phi_k \tag{2.14}$$

[3]Note the difference between $\boldsymbol{\epsilon}$, the strain rate, and $\epsilon$, the turbulent dissipation rate, in equations 2.14–2.15.

$$\frac{\partial \rho \epsilon}{\partial t} + \nabla \cdot \left( \rho \underset{\rightarrow}{U} \epsilon - \left[ \mu + \frac{\mu_t}{\sigma_\epsilon} \right] \nabla \epsilon \right) = c_{\epsilon 1} \frac{\epsilon}{k} \boldsymbol{\tau_t \epsilon} - c_{\epsilon 2} f_2 \rho \frac{\epsilon^2}{k} + \phi_\epsilon \tag{2.15}$$

It can be seen that there are a large number of constant parameters ($c_\mu = 0.09$, $c_{\epsilon 1} = 1.45$, $c_{\epsilon 2} = 1.92$, $\sigma_k = 1.0$, $\sigma_\epsilon = 1.3$) as well as damping functions ($f_\mu$, $f_2$) and terms ($\phi_k$, $\phi_\epsilon$) that are related to the behaviour of the values at walls. Equations for these functions are provided in e.g. Bardina *et al.* (1997), among others.

### $k$-$\omega$ model

The $k$-$\omega$ model, is very similar in many respects to the $k$-$\epsilon$ model and was developed at around the same time. It uses a different form of the turbulent dissipation rate, $\omega$:

$$\mu_t = \frac{\rho k}{\omega} \tag{2.16}$$

$$\frac{\partial \rho k}{\partial t} + \nabla \cdot \left( \rho \underset{\rightarrow}{U} k - \left[ \mu + \sigma^* \mu_t \right) \nabla k \right) = \boldsymbol{\tau_t \epsilon} - \beta^* \rho \omega k \tag{2.17}$$

$$\frac{\partial \rho \omega}{\partial t} + \nabla \cdot \left( \rho \underset{\rightarrow}{U} \omega - \left[ \mu + \sigma \mu_t \right] \nabla \omega \right) = \alpha \frac{\omega}{k} \boldsymbol{\tau_t \epsilon} - \beta \rho \omega^2 \tag{2.18}$$

### Estimation of $k$, $\epsilon$ and $\omega$

While the above approaches have simplified the turbulence problem to only two parameters, there remains the problem of estimating these parameters for practical cases. Various rules-of-thumb and approximate formulae exist for this purpose, most of which focus on first approximating simpler parameters, such as the turbulent length scale, $l$, and the turbulent intensity, $I$, for specific problems.

The turbulent length scale is defined as

$$l = C_\mu \frac{k^{\frac{3}{2}}}{\epsilon} \tag{2.19}$$

and is commonly approximated as being half of the thickness of the inlet boundary layer. Another rule-of-thumb suggests that it can be approximated as

$$l \approx 0.07 d_h \tag{2.20}$$

for closed pipes where $d_h$ is the hydraulic diameter. This use of the hydraulic diameter in the estimation of $l$, suggests that it may be possible to make a similar relationship between the hydraulic radius, $R$, used in

fluvial flow (see section **??**) and the turbulent length scale. The definition of $d_h$ as $4A/P$ suggests the following:

$$l \approx 0.07\left(\frac{4A}{P}\right) = 0.28R. \tag{2.21}$$

The turbulent intensity,

$$I = \frac{\sqrt{\frac{2}{3}k}}{U} \tag{2.22}$$

is generally estimated qualitatively at the inlet and outlet of the domain. For a stationary fluid or laminar flow, $I = 0$. For flow at low Reynolds Numbers, it is generally assumed that $0.01 \leq I \leq 0.05$ while flow leaving a complex structure might have a turbulence intensity as high as $0.20$.

For flow in pipes, an approximation formula exists:

$$I \approx 0.16 Re_{d_h}^{-\frac{1}{8}} \tag{2.23}$$

in which $Re_{d_h}$ is the Reynolds Number of the flow based on the hydraulic diameter, but no widely used and validated approximation exists for other classes of problem.

On the assumption that most of the flows we consider in this work will be in motion, but not highly turbulent, the key parameters for the RAS turbulence models could be estimated as follows, in the absence of real-world data.

$$k \approx 1.5(0.03 \pm 0.02)^2 U^2 \tag{2.24}$$

$$\epsilon \approx C_\mu \frac{k^{1.5}}{0.28R} \tag{2.25}$$

$$\omega \approx C_\mu^{-\frac{1}{4}} \frac{k^{0.5}}{0.28R} \tag{2.26}$$

These equations, however, are very much estimates of the turbulence and are highly inaccurate. Simply carrying through the range of possible values of $I$ in equation 2.24 leads to a range of $k$ from $1.5 \times 10^{-4} U^2$–$3.8 \times 10^{-3} U^2$, a range of $\epsilon$ from $5.9 \times 10^{-7} U^3 R^{-1}$–$7.4 \times 10^{-5} U^3 R^{-1}$ and a range of $\omega$ from $2.4 \times 10^{-2} U R^{-1}$–$1.2 \times 10^{-1} U R^{-1}$.

Further, for many of the problems posed here, very little turbulence will be indicated by these equations. It is therefore reasonable in many cases to neglect the turbulent effects in the flow as a model approximation. This reduces the computational cost of the model, removes a number of parameters which cannot be accurately estimated and will often

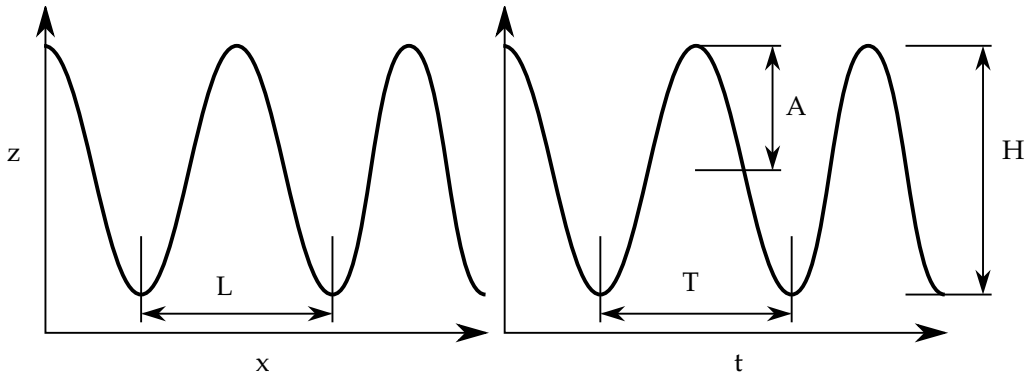


Figure 2.1: Plots of water surface elevation, $\eta$, against distance and time with some key wave properties illustrated.

have relatively little effect on the results. Of course, for problems for which a reliable estimation of the turbulence is available, the inclusion of turbulence modelling will generally improve the accuracy of the model.

## 2.2 Waves

### Basic Properties

Waves in the interface between two fluids (for example, waves on water) can be defined using a number of basic properties as illustrated in figure 2.1 (Boccotti 2000).

- The wave height, $H$, or the amplitude, $A = \frac{H}{2}$.
- The wave length, $L$, or the wave number, $k = \frac{2\pi}{L}$.
- The wave period, $T$, frequency, $f = T^{-1}$, or angular frequency, $\omega = 2\pi f$.

The particles under a surface water wave move in elliptical orbits, with the height of the ellipse growing with water depth until the orbits become circular in deep water.

In general, a water wave can be defined by the following equations for horizontal and vertical velocity, pressure and free surface elevation:

$$U_x(x,z,t) = \frac{gHk}{2\omega}\frac{\cosh[k(d+z-h)]}{\cosh(kd)}\cos(kx-\omega t) \tag{2.27}$$

$$U_z(x,z,t) = \frac{gHk}{2\omega}\frac{\sinh[k(d+z-h)]}{\cosh(kd)}\sin(kx-\omega t) \tag{2.28}$$

$$p(x,z,t) = -\rho g z + \frac{\rho g H}{2}\frac{\cosh[k(d+z-h)]}{\cosh(kd)}\cos(kx-\omega t) \tag{2.29}$$

$$\eta(x,z,t) = \frac{H}{2}\frac{\cosh[k(d+z-h)]}{\cosh(kd)}\cos(kx-\omega t) \tag{2.30}$$

in which $h$ represents the mean water level and terms of order $H^2$ or greater have been neglected. Equations 2.29 and 2.30 are both only valid below the free surface. (Boccotti 2000)

## Wave Spectra

Waves in nature generally occur with a wide range of frequencies and amplitudes simultaneously. These are referred to as irregular waves. The wave spectrum at a particular location defines the strength of each wave frequency at that location in terms of the power available at that frequency. The water surface elevation from an irregular sea state can be reconstructed from a wave spectrum using

$$\eta = \int S(\omega) sin(\phi(\omega) - \omega t) d\omega \tag{2.31}$$

in which $S(\omega)$ represents the amplitude of the waves with rotational velocity $\omega$ and $\phi(\omega)$ gives the phase. Clearly $S(\omega)$ can be equally well represented by a function $S(f)$, and this is the form in which most parametric wave spectra are given. The phase is often not specified by formulae for wave spectra and is, instead, assumed to be a random function.

Two parametric wave spectra are in common use whose formulae can be found in most text-books, e.g. Chadwick *et al.* (2004). The Pierson-Moskowitz (PM) spectrum,

$$S(f) = \frac{K_p g^2}{(2\pi)^4 f^5}\exp\left(-\frac{5}{4}\left[\frac{f_p}{f}\right]^4\right) \tag{2.32}$$

$$f_p = \frac{0.8772g}{2\pi U_{19.5}}; K_p = 0.0081 \tag{2.33}$$

approximates the wave spectrum of a "fully arisen" sea, controlled only by the parameter $U_{19.5}$, the wind speed 19.5 m above the sea surface.

The JONSWAP spectrum was based on observations from the North Sea and adds a dependency on the fetch length, $F$:

$$S(f) = 0.076 X_{10}^{-0.22} \frac{g^2}{(2\pi)^4 f^5} \exp\left(-\frac{5}{4}\left[\frac{f_p}{f}\right]^4\right)\gamma^a \tag{2.34}$$

$$X_{10} = \frac{gF}{U_{10}^2}; f_p = \frac{3.5g}{U_{10}X_{10}^{0.33}}; a = \exp\left(-\frac{(f-f_p)^2}{2W^2 f_p^2}\right) \tag{2.35}$$

where $W = 0.07$ where $f \leq f_p$ and $W = 0.09$ otherwise. It can be seen that this spectrum takes two parameters: $U_{10}$, the wind speed at a height of 10 m above the sea surface and the fetch length, $F$, making this formulae more appropriate for seas with short fetches, which cannot be modelled appropriately with the PM spectrum.

The above description of a wave spectrum assumes that the waves are travelling in a single direction. While this is often appropriate for laboratory experiments, it is rarely the case in the real world. In these cases, a directional wave spectrum can be used and the power of each wave is given as a function of both frequency and direction. Equation 2.31 becomes

$$\eta = \iint S(\omega,\theta) sin(\phi(\omega,\theta) - \omega t) d\omega d\theta \tag{2.36}$$

## Focussed Waves

Focussed waves are irregular wave series generated in such a way that a particularly large, "worst case" crest or trough is formed at a particular point in space and time (the focal point). An irregular wave series can be considered as a series of superposed sine waves as shown in figure 2.2. A focussed wave group is generated by tuning the phases of each of the component waves so that they align at the focal point. This is shown in figure 2.3.

Focussed waves can be generated from a unidirectional spectrum by tuning the phase angle of each individual wave using:

$$\eta(x,t) = \sum_i \frac{H_i}{2} \sin\left(k_i(x - x_f) - \omega_i(t - t_f)\right) \tag{2.37}$$

in which $x_f$ is the distance from the generation point at which the worst-case wave should be generated and $t_f$ is the time at which the focussed wave should occur. In practice, not all values of $x_f$ and $t_f$ are valid as sufficient time needs to be allowed for all of the wave components to propagate to the focus point.

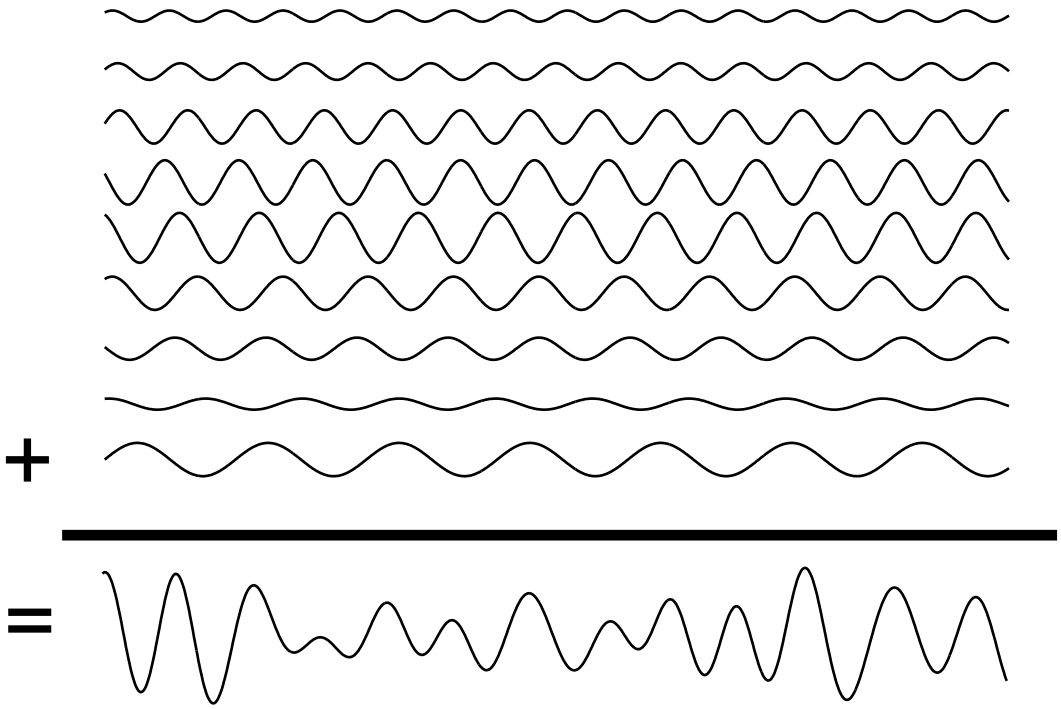

Figure 2.2: Diagram showing the summation of a large number of sine waves to produce an irregular wave.

Other techniques for wave focussing exist. For example, in a multi-directional wave spectrum, the wave directions can be tuned to provide a focussed wave at a point, but it is the temporally focussed waves described above that will be used in this study as they have several properties that make them useful for CFD simulations:

- They can be generated using only a unidirectional spectrum and can therefore be used in vertical two-dimensional models or narrow three-dimensional models. This means that temporally focussed waves can be generated with smaller meshes than spatially focussed waves.

- They can be generated in only a very short time and create a compact group of waves that travel through the model. This allows models of them to have short run-times of a few seconds rather than the several hours that would be required to simulate a conventional test using an irregular wave spectrum. (Morgan & Zang 2010, Zang *et al.* 2010)

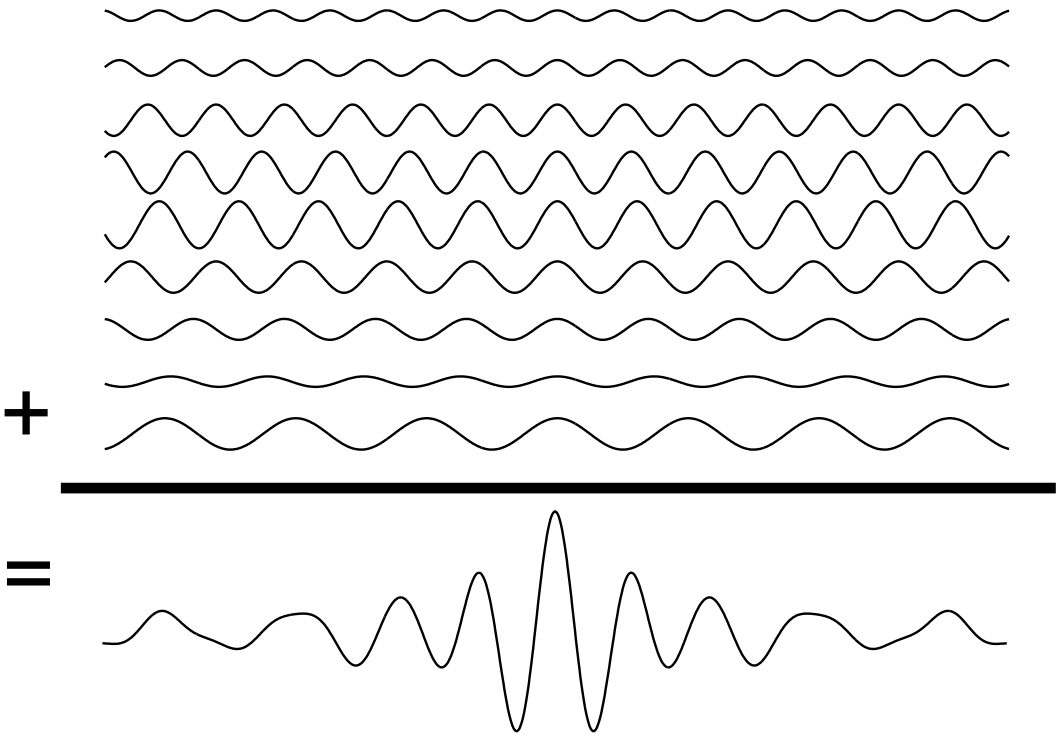

Figure 2.3: Diagram showing the summation of a large number of sine waves to produce a focussed wave group.

- These focussed wave groups have several useful mathematical properties that allow the first, second, third and higher order effects of the wave-structure interaction to be considered separately. (Zang *et al.* 2006, Zang *et al.* 2009)

## 2.3 Hydraulic Forces

If the failure of a defence structure due to hydraulic loading is to be accurately modelled, the correct determination of the forces on the structure due to the hydraulic action is critical. It is useful to break hydraulic loading on structures into two components: direct (pressure) stresses and shear stresses.

### Direct Stresses

Direct stresses arise from the water pressure on the structure. Generally a structure can be considered as a series of discrete elements and the fluid

pressure acting on these elements may vary across each element. The total pressure force on each element is given by the surface integral of the pressures on the surface of the element. In terms of a finite volume model, the surface of each structural element will be composed of a number of faces, each with a known normal and area. In this case the total force on the element will be given by

$$\underrightarrow{F_{tot}} = \sum_{i=1}^{i=N} p_i A_i \underrightarrow{\hat{n}_i} \tag{2.38}$$

Direct stresses may be long-term, the force on a hydraulic structure during a flood, for example; or short-term, such as the instantaneous "slamming" action of a wave breaking on the face of a structure. Both types of action may be critical in a breaching scenario: the long-term stresses will affect the overall stability of embankments and the solid structures upon them, while the short-term loadings may cause localised damage to the embankment face or structures.

## Shear Stresses

In contrast to the direct stresses, above, the determination of the shear stresses between a flowing fluid and a solid is a very difficult problem. In structural design this hydraulic shear stress is often neglected as it is generally much smaller than the direct stress (unless the surfaces are very rough) but its determination is critical to the assessment of incipient motion and erosion of granular bed material. (Mirtskhoulava 1988)

The traditional approach to determining the bed shear stress, used by many of the standard formulae for incipient motion and sediment transport use very simple, depth-averaged hydraulic models, leading to a bed shear stress determined from the steady state flow over a sloping bed:

$$\tau_b = \frac{\gamma A S}{P} = \gamma R S \tag{2.39}$$

in which $\gamma$ is the specific weight of water, $R$ is the hydraulic radius and $S$ is the bed slope. (Graf 1971)

The limitations of this formula are evident: it is valid only for one-dimensional flow, it assumes that the flow is steady and that the shear stress is evenly distributed over the bed. None of these assumptions are likely to hold in a breaching scenario and a more detailed approach is therefore required.

Considering the problem at its most general, the shear stress on the surface of the bed must, for equilibrium, be equal for both the water and the soil, and can therefore be represented using the fluid velocity and equation 2.4[4]:

$$\boldsymbol{\tau} = \frac{1}{2}\rho\nu\left[\nabla \underset{\rightarrow}{U} + \left(\nabla \underset{\rightarrow}{U}\right)^T\right] \tag{2.40}$$

In other words, the bed shear stress is related to the change in velocity of the water near the bed,

$$\tau_b = \frac{\partial U}{\partial z}. \tag{2.41}$$

While this definition of bed shear stress is of little use with a depth-averaged model, it can theoretically be used with a three-dimensional hydraulic model.

Equation 2.40 suffers from a practical problem, however: it is difficult to accurately describe the velocity/depth profile near a rough bed, and accurate direct simulation of the profile is prohibitively computationally expensive.

Several equations for the near-wall velocity profile have been proposed in the literature, of which probably the best-known is von Karman's equation:

$$U(z) = \bar{U} + \frac{u_*}{k}\left(1 + 2.3\log\frac{z}{z_0}\right) \tag{2.42}$$

which describes a logarithmic distribution of velocity near the wall (See, e.g. Vanoni *et al.* (1960)). It should be noted that there is an ongoing debate about the nature of this layer and whether it is logarithmic (according to Karman and Prandtl), or whether it is a power law (according to Barenblatt, George, Afzal and others). Buschmann & Gad-el Hak (2007) investigate this in more detail. For the purposes of this report the distribution will be assumed to be logarithmic as it can be seen from the data presented by Buschmann that both approaches yield reasonable results and the problem is therefore largely academic.

Even the logarithmic velocity distribution of Karman, however, breaks down in the near vicinity of the wall. The behaviour of the fluid very close to the wall forms the so-called "laminar sub-layer".

Several equations exist for near-wall velocity profiles that attempt to span all the near-wall layers, including this laminar sub-layer. These in-

[4]The normal stress terms are neglected here.

clude the Reichardt profile, developed by H. Reichardt in 1959,

$$U(z) = \frac{1}{\kappa}\log\left(1+\frac{\kappa u_* z}{\nu}\right) + 7.8\left[1-\exp\left(-\frac{u_* z}{11\nu}\right) - \frac{u_* z}{11\nu}\exp\left(-\frac{u_* z}{3\nu}\right)\right] \tag{2.43}$$

and the simpler power law,

$$U(z) = U_\infty\left(\frac{z}{\delta}\right)^{\frac{1}{\alpha}}, 0 \leq z \leq \delta \tag{2.44}$$

in which $\delta$ is the width of the near-wall region, $U_\infty$ is the fluid speed away from the wall and $\alpha$ is a constant usually taken as 7, leading to the "1/7th power law". (Berselli & John 2006)

It is possible to calculate the shear stress on the bed using these profiles in combination with equation 2.40 assuming we have sufficient information about the velocity away from the wall to determine the scaling of the profile.

This technique requires a certain amount of care, to fit the velocity distribution curves to the known far-field velocities, but can be used in some cases to reduce the need for complex turbulence models.

There exists one further problem, however: in natural channels and on flood plains and coastal defences, the bed is not normally perfectly smooth and can generally be considered to be hydraulically "rough". The geometry of hydraulic model representations of natural beds is generally simplified into a series of planes, smoothing out the bed-forms and the features in between known points. To account for this, a "roughness", $\chi$ (see figure 2.4), is introduced, describing the extent by which the actual form of the bed differs from the assumed shape.

This roughness is important in the determination of the bed shear stress as it will greatly affect the formation of the near-wall layers. Figure 2.4 illustrates the problem. On a perfectly smooth bed (a), the wall layers form as normal. On a slightly rough bed (b), the roughness is entirely contained within the laminar sub-layer and has relatively little effect on the overall flow, but will have some effect on the bed stresses due to the change in bed shape and surface area. On a rough bed (c), the roughness of the bed extends into the log layer, deforming the laminar sub-layer, causing additional turbulence and further increasing the area over which the bed stresses act. On a very rough bed (d), as might be found in a natural channel, the roughness of the bed extends well into the main flow and the shape of the wall-layers are severely distorted.

As might be expected, the simplistic approach for determining the bed shear stress outlined above will be reasonably accurate for the smoother

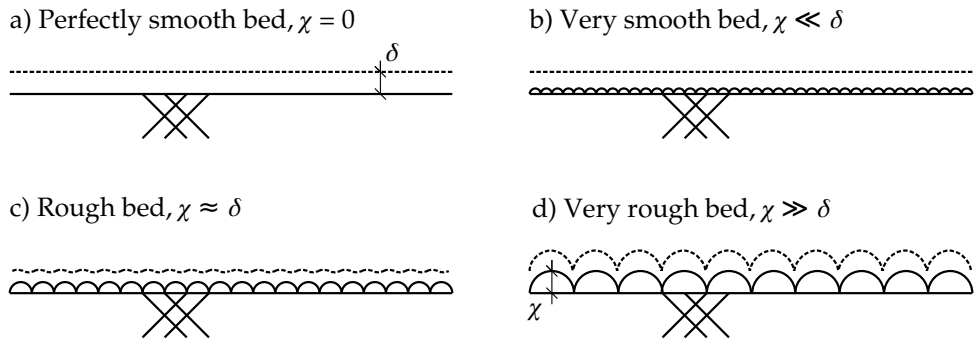


Figure 2.4: Schematic diagram of changes in the shape of the near-wall layers due to bed roughness.

beds, (a), (b) and even (c), but it cannot be expected to produce satisfactory results for case (d) unless the roughness (i.e. the shape) of the bed is explicitly modelled. Such detailed modelling is rarely practical.

## 2.4 Flow Through Soil

### Darcy Law

One of the factors which is critical to the behaviour of soil when it is loaded by hydraulic action is the flow of water through the soil and the pore pressures that this induces. This has traditionally been calculated by geotechnical engineers using the one-dimensional Darcy law for creeping flow.

$$U = -K\frac{dh}{dx} \tag{2.45}$$

in which $U$ is the velocity of the water within the soil, $h$ is the piezometric head and $K$ is the hydraulic conductivity, or permeability, of the soil.

This can be extended to three dimensions as

$$\underset{\rightarrow}{U} = -K\nabla h. \tag{2.46}$$

It is important to note that the permeability coefficient, $K$ in the Darcy equation is not fundamental to the soil and is highly dependent on the environmental conditions. Head (1982) lists these as:

1. Particle size distribution
2. Particle shape

3. Particle texture
4. Mineralogy
5. Voids ratio
6. Saturation
7. Soil homogeneity and stratification
8. Nature of the fluid
9. Nature of the flow
10. Temperature of the fluid

To these, it seems sensible to add, from TAW (1996),

11. Macroscopic soil structure and fissuring.

It can be seen from this list that permeability is not specific to a medium of a given type, but is highly dependent on the placing and compaction of the soil or gravel and the nature of the fluid flow.

In particular, the conventional methods for determining the $K$ parameter use a steady and laminar flow through the material. This is true both of most geotechnical laboratory tests (Head 1982) and estimation formulae. This means that values of $K$ estimated by conventional means will not be suitable for fast flows, very coarse materials or unsteady flows, such as wave motion.

## Darcy-Forchheimer Equation

In many situations the Darcy equation does not adequately model the behaviour of the fluid in the soil. One attempt to generalise the Darcy equation is the Darcy-Forchheimer equation, in which an additional term and coefficient have been introduced to account for the viscous effects of the fluid.

$$\nabla h = -\left(a\underset{\rightarrow}{U} + b|\underset{\rightarrow}{U}|\underset{\rightarrow}{U}\right) \tag{2.47}$$

in which $a$ and $b$ are material constants.

When $a = \frac{1}{K}$ and $b = 0$, equation 2.47 reduces to the three-dimensional Darcy equation (equation 2.46).

While more representative than the Darcy equation alone, according to Sidiropoulou *et al.* (2007), "in practice, [the Darcy-Forchheimer equation's] use is limited to coarse granular porous media ..., fractured or

karstified aquifers," although this appears to be predominantly a question of usage and not a shortcoming of the method itself. This lack of usage may simply be because the equation is more difficult to use than the Darcy law as it replaces the single, relatively well known hydraulic conductivity, $K$, with two material parameters, $a$ and $b$ which are extremely problem-specific and for which laboratory tests are not well-established.

It should be noted that, despite the inclusion of terms to deal with the viscous effects of the fluid, the dependence of the $a$ parameter (analogous to the the $K$ parameter of the conventional Darcy equation) on the nature of the fluid flow has not changed. $K$ values are generally quoted with the assumption of steady, gradual flow and these are not generally applicable to unsteady, transient flow fields regardless of whether the Darcy or the Darcy-Forchheimer equation is used.

## Darcy and Forchheimer Parameters

Various authors use various forms of the Darcy and Forchheimer parameters, and it is important to disambiguate them here: Sidiropoulou *et al.* (2007) uses $a$ and $b$ notation, as above. Also widely used are the parameters $\alpha$ and $\beta$, given by

$$a = \alpha \frac{(1-n)^2}{n^3} \frac{\nu}{g D_{50}^2} \tag{2.48}$$

$$b = \beta \frac{1-n}{n^3 g D_{50}} \tag{2.49}$$

(Reis *et al.* 2009).

In the OpenFOAM implementation that is used here the permeability is represented by an additional sink term in the momentum equation:

$$S_p = -\left( \boldsymbol{D} + \frac{1}{2}\rho |\underrightarrow{U}| \boldsymbol{F} \right) \underrightarrow{U} \tag{2.50}$$

(Hafsteinsson 2009). The tensor quantities $\boldsymbol{D}$ and $\boldsymbol{F}$ can be represented (for homogeneous media) as two scalars $D$ and $F$ which, in turn, can be related to the parameters above as

$$D = \nu a \tag{2.51}$$

$$F = \frac{2b}{\rho} \tag{2.52}$$

In addition to the momentum sink term, the OpenFOAM implementation also introduces the material porosity as a factor to the time-dependant terms of the Navier-Stokes equations. (Hafsteinsson 2009)

Sidiropoulou *et al.* (2007) explores a variety of empirical and semi-empirical formulae for the $a$ and $b$ coefficients and evaluates them using a dataset derived from a literature review. In general these methods use the porosity, $n$, and grain size of the soil as well as basic fluid properties such as kinematic viscosity, $\nu$. Among the equations suggested by Sidiropoulou, three sets are considered here:

Ward was one of the first to propose a set of equations, in 1964, based predominantly on a study of glass beads and homogeneous sands:

$$a = \frac{360\nu}{gD_{50}^2} \tag{2.53}$$

$$b = \frac{10.44}{gD_{50}}. \tag{2.54}$$

Sidiropoulou *et al.* (2007) propose their own formulae in which they introduce an additional dependence on a Reynolds Number of the flow ($Re = \frac{UD}{\nu}$):

$$a = \frac{6570\nu(1-n)}{gD^2}, \qquad 10 < Re \leq 80 \tag{2.55}$$

$$b = \frac{98.1(1-n)}{gD}, \qquad 10 < Re \leq 80 \tag{2.56}$$

$$a = \frac{8316\nu(1-n)}{gD^2}, \qquad Re > 80 \tag{2.57}$$

$$b = \frac{88.65(1-n)}{gD}, \qquad Re > 80 \tag{2.58}$$

Sidiropoulou *et al.* (2007) also propose a set of empirical formulae based on a regression analysis of a dataset of results taken from the literature:

$$a = 0.003333 D^{-1.500403} n^{0.060350} \tag{2.59}$$

$$b = 0.194325 D^{-1.265175} n^{-1.141417} \tag{2.60}$$

It should be noted that these formulae illustrate one of the issues with the accurate simulation of porous media: the estimation of the Darcy-Forchheimer parameters. The porous media test case used in chapter 5 can be used to illustrate this: here a breakwater was used with the parameters $D_{50}$ = 0.0181 m, $n$ = 0.426, $\alpha$ = 3009 and $\beta$ = 2.455. Table 2.1 shows the values of $a$ and $b$ that can be calculated from the $D_{50}$ and $n$ values using the above formulae.

It can be seen that the results vary widely, with the values of $a$ and $b$ varying by an order of magnitude, depending on the formulae used to

| Variable | Reported Value | Eq'ns 2.53 –2.54 | Eq'ns 2.55 –2.58 | Eq'ns 2.59 –2.60 |
|---|---|---|---|---|
| $a$ | 3.99 | 0.112 | 1.17 | 1.30 |
| $b$ | 103. | 58.8 | 317. | 82.4 |
| $D$ | $4 \times 10^{-6}$ | $1 \times 10^{-7}$ | $1 \times 10^{-6}$ | $1 \times 10^{-6}$ |
| $F$ | 0.2 | 0.1 | 0.6 | 0.2 |

Table 2.1: Values of $a$, $b$, $D$ and $F$ calculated from reported parameters of a single porous breakwater.

calculate them. This is a significant problem for the simulation of porous media for, as is shown in chapter 5, model results are very sensitive to the value of $a$.

## 2.5 Coastal models

A coastal CFD model is essentially a numerical approximation to an experimental wave tank or wave flume and the model schematisation reflects this. Generally, a rectangular box is used, with one wall set to generate waves and either two or three "solid" walls some of which may have wave absorbing properties. The structure or body under investigation is simply placed in the middle of this box so that the waves interact with it in the desired fashion.

The principal requirement of a coastal model is that the waves interacting with the structure should not reflect in such a way that the reflected waves contaminate the results. Wave reflections in the model must therefore either be absorbed or damped or must simply never propagate to any location where they are not wanted.

While the introduction of a notional porous medium of the sort described in section 2.4 would serve to absorb waves, in most of the cases described below a simpler approach was used: The domain was simply extended, using relatively coarse cells, to a sufficient length that propagating reflected waves did not contaminate the results. The clearest example of this is in the three-dimensional wave interaction case study described in chapter 5, where the domain has been extended so that waves reflecting from the porous breakwater structure under test do not return from the domain boundary before at least three incoming waves have interacted with the structure.

In the cases described here a solid wall boundary condition was used

at the downstream end of the model. It is possible to use "open" boundaries as an alternative, but most of the formulations for open boundary conditions will result in wave reflection from the downstream end. Additionally, using a solid wall boundary in this location allows mass conservation in the model to be more easily assessed.

It should be noted that using a notional porous medium to damp waves at the edges of the numerical wave tank suffers from a particular problem: it is very difficult to accurately damp waves on the wave-generating boundary. The interaction of waves with wave paddles is a relatively well-studied field, however, and several methodologies exist to apply active wave damping through adjusting the input wave to cancel the reflected waves (Troch & De Rouck 1999). Such an approach has not been implemented in OpenFOAM as part of this study as it was not necessary to simulate the validation tests presented here. Many validation tests in the literature, however, use long sequences of irregular waves, the simulation of which requires wave absorbing boundaries. The implementation of an active absorbing wave boundary condition such as the AWAVOF condition described in Troch & De Rouck (1999) should be considered to be a useful topic of further work and validation.

## 2.6 Meshing

### Mesh types

While OpenFOAM-based models use polyhedral, unstructured meshes, some effort was made to keep the meshes used in this research as regular as possible. Preliminary testing indicated that, while the overall solution of the hydraulic problems was broadly unaffected by the type of mesh used, regular, hexahedral meshes had two distinct advantages: the formulation of the volume-fraction boundary condition on the walls is much simpler and the problem is much easier to post-process.

In general, it is desirable in VoF-based CFD to have the free surface pass through cell faces as this gives the "tightest" representation of the free surface and a wide transition zone from $\alpha_i = 0$ to $\alpha_i = 1$ is avoided. This is not always possible, however, as the free surface will move over the course of a simulation (due to waves, etc.). While it is possible to have the mesh move with the free surface to a limited extent, this becomes much harder during violent interactions where the free surface may break up.

When the free surface does not pass exactly through a cell face, it can become difficult to reconstruct the exact position of the free surface within the cell. This problem is rendered even more difficult in the case where non-hexahedral cells are used. The problem of surface reconstruction is discussed at greater length by, for example, Kothe *et al.* (1991).

The main advantage of hexahedral cells for this surface reconstruction problem is that relatively simple methods can be used in the post-processing stage to produce a surface from the volume fraction field which is visibly believable, and while these simple methods may have inaccuracies, these do not exceed the inaccuracies inherent in the model itself. Non-hexahedral meshes, when used with these same simple, computationally cheap, methods for surface reconstruction, produce water surfaces that look visibly "choppy" and require either much finer meshes or higher-order surface reconstruction methods to reproduce a believable surface.

It should be noted that this "choppiness" is normally purely an artifact of the post-processing and occurs at a sub-cell level—a model on a tetrahedral mesh and on a hexahedral mesh produce substantially similar results (assuming appropriate solution methods and numbers of iterations are used in each case).

## Meshing approach

The meshing approach used in the models presented here is in relatively common use with OpenFOAM and interFoam modelling and was designed with automation in mind. This gives it several key advantages over other, more conventional, CFD meshing techniques from the point of view of the practising civil engineer.

- It produces adequately-refined, predominantly hexahedral meshes relatively quickly.
- It is relatively easy, requiring little specialised skill or knowledge and could therefore be used by practising engineers with little additional training.
- The input requirements are very simple, and can be taken directly from existing three-dimensional CAD drawings.

The procedure is as follows:

1. An encompassing "model domain" is defined.

2. A coarse mesh is applied to this domain, possibly with some graded refinement.

3. Areas requiring additional refinement within the domain are defined using triangulated surfaces and this refinement is applied using an octtree-based approach.

4. Objects and areas which are to be removed from the domain are defined as triangulated surfaces and cells with centres within these objects are removed.

5. The vertices of the remaining cells are adjusted so that they lie directly on the object surfaces, removing the stair-step representation.

## 2.7 Boundary Conditions

One of the most important parts of the CFD modelling process is the accurate definition of the boundary conditions. A variety of different physical boundary conditions exist in the vicinity of an overtopping or breaching embankment and these must be represented in the CFD model by constraints on the available variables of pressure, velocity and volume fraction. The following sections describe how each physical boundary condition was modelled in the general case.

### Solid Wall Conditions

Solid wall conditions are used to model solid, impermeable structures as well as soil or bed conditions which are assumed to be immobile and impermeable. The approach used to model solid walls should vary according to the mesh size and turbulence formulation used. Additionally, if the stresses or forces on the wall are required outputs of the model, this further constrains the modelling approach.

On very coarse meshes, where the shear stresses and forces on the wall are not of interest, the "slip" condition for velocity can be used. Here velocity normal to the wall is constrained to a value of zero, while velocity tangential to the wall is unaffected:

$$\underrightarrow{U}_{bdy} = \underrightarrow{U} - \underrightarrow{U} \cdot \underrightarrow{\hat{n}} \tag{2.61}$$

where $\underrightarrow{\hat{n}}$ is the unit normal vector to the boundary and $\underrightarrow{U}_{bdy}$ is the velocity vector that is applied by the boundary condition.

On finer meshes, and where the wall or bed shear stress is of importance, however, the "no-slip" condition for velocity must be used:

$$\underset{\rightarrow}{U}_{bdy} = (0.0, 0.0, 0.0)^T \tag{2.62}$$

This is the approach used in all of the models described in this report. This condition accurately prevents fluid motion immediately adjacent to the boundary condition, however, unless extremely fine meshes are used, the model will not be able to correctly resolve the velocity profile near to the wall. This will lead to a slight underestimate of the flow velocity near the wall. While this is generally not a problem, it does significantly affect the shear stress calculations (see section 2.3). It is possible to overcome the problem by using a turbulence model in the simulation combined with an appropriate wall-function on the boundary. (George 2009)

The boundary conditions used for pressure and volume fraction are the same for both coarse and fine meshes. The zero-gradient condition can be used for the pressure in all cases, but the volume fraction condition is a little more complex.

The best boundary condition for the volume fraction depends on the angle between the water surface and the wall. In the most common case, the water surface will be perpendicular to the wall, and the zero-gradient condition can be used. When the water surface and the wall do not form a right-angle, however, the gradients of volume fraction applied at the wall must be adjusted to simulate this. The effect of these adjustments is shown in figure 2.5. Figure 2.5a shows the normal condition, while figure 2.5b shows the effect of applying the zero-gradient condition when the water surface is not perpendicular: the boundary is effectively a symmetry plane for the volume fraction parameter and this models a sharp change in the gradient of the water surface. If uncorrected, this causes the model to generate spurious velocities near the boundary to force the water to assume this unnatural shape. Figure 2.5c shows the effect of applying corrections to the boundary to force the water surface to meet the wall at a prescribed angle.

This effect was demonstrated in the "interFoam" model by creating a model of a box at a 45° angle and simulating a quantity of still water in the bottom of it. The results of this are shown in figure 2.6. The figure shows portions two boxes one on the right and one on the left. In the figure each computational cell is shown and is coloured according to the volume fraction (with dark cells representing water and pale cells representing air). For each box the position of the interpolated water surface is shown. The box on the right uses the zero-gradient condition (as figure

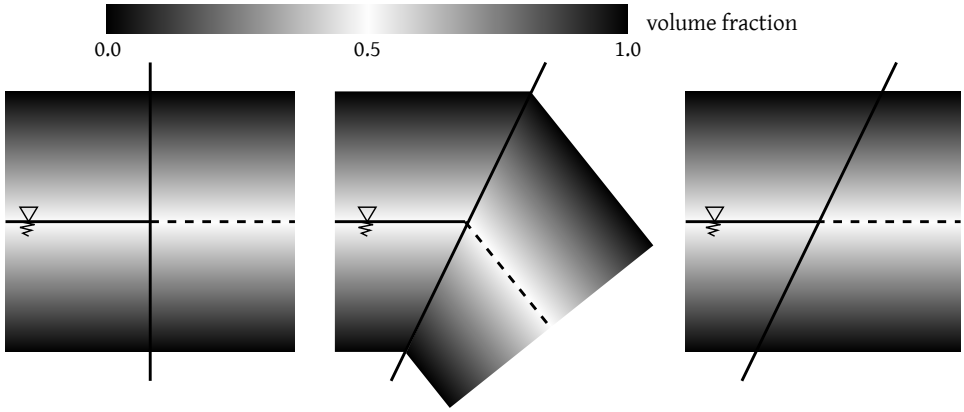


Figure 2.5: Diagram showing how the volume fraction parameter varies at the boundary with and without adjustments for the water surface contact angle.

2.5b) and it can be seen that the water surface is distorted upwards at the boundary. By contrast the box on the left has the boundary gradients adjusted (as figure 2.5c) and while it can be seen that the adjustment is not perfect, the distortion of the water surface is much reduced.

While this could be considered a problem with the model, the practical effects of errors of this kind in the boundary schematisation are very limited. The spurious flows generated at the free surface are very small and will only seriously affect results if very slow moving or still water is being modelled.

### Atmospheric Conditions

For the atmospheric boundary conditions it was assumed that during the construction of the model, sufficient space would be left between the free surface and the atmospheric boundary that no water would come into contact with this boundary. Accordingly, the boundary has the water volume fraction set to a fixed value of zero.

The velocity boundary condition was set using OpenFOAM's "pressureInletOutletVelocity" condition. This sets the normal velocity on the boundary to be calculated from the pressure differences at every point on the boundary. This has the effect that any water which does impinge on the atmospheric boundary will be removed from the domain and air can be exchanged through the boundary to prevent unwanted area of high

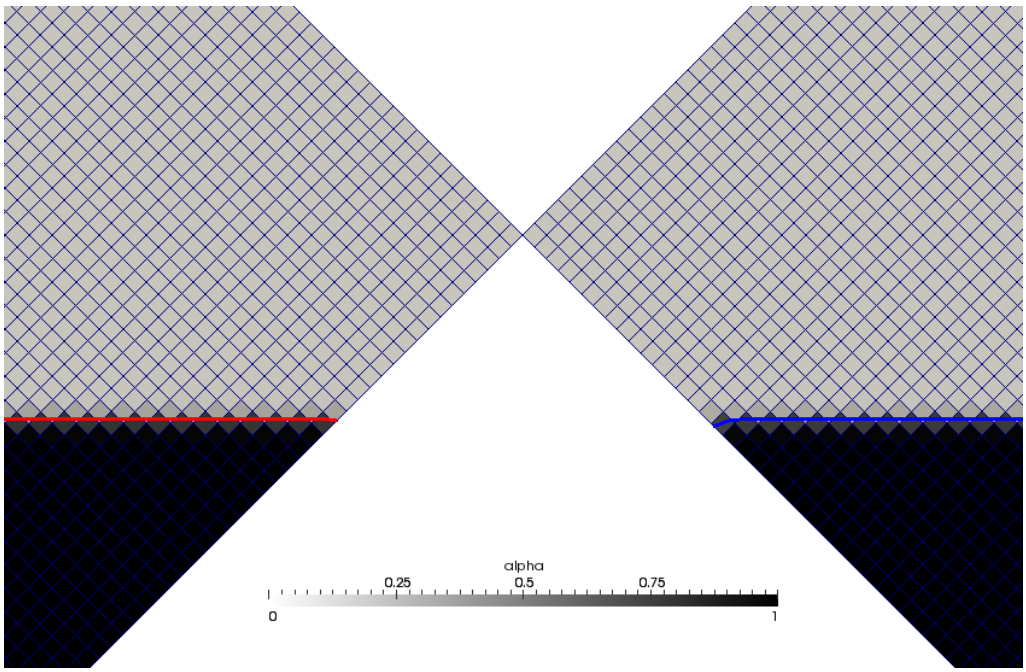


Figure 2.6: Results from a simple test model comparing the effects of the zero-gradient boundary condition for a solid wall (on the right) with a condition where the gradients are adjusted to match the angle of the water surface (on the left).

air pressure in the model. The tangential velocity on the boundary can optionally be specified in order to simulate wind conditions.

The boundary condition for pressure was calculated at each stage using the velocities and the model's intermediate flux results to keep the total pressure on the boundary equal to zero.

### "Dry Air" Conditions

The boundary conditions applied for air over dry land have generally been set to a "zero-gradient" condition for all of the variables. This has the effect of permitting flow of water and air out through the boundary. Some reflection is possible from this type of boundary. It is assumed, however, that the boundary is sufficiently far away from the area of interest that any distortion due to vortical flow near the boundary will not affect the model results in the area of interest.

**Wave Conditions**

Conditions for water waves are not incorporated into the OpenFOAM model by default. As part of this study a series of water wave boundary conditions were added to the model, and it is these conditions that are described below.

Waves are generated by calculating and applying velocity values on the boundaries. The water surface elevation and sub-surface velocities for the wave are calculated for each cell on the boundary using Stokes' wave theory (equations 2.27–2.30). The water surface elevation is converted into a volume fraction field by means of a simple limiting function:

$$\alpha = min\left[max\left(\left[\eta(t,x) + h - z\right], \frac{-\Delta z}{2}\right), \frac{\Delta z}{2}\right] + \Delta z \tag{2.63}$$

in which $\Delta z$ is a small number representing the thickness of the transition zone between water and air. The velocities on the boundary are then generated from

$$U = \alpha \frac{gHk}{2\omega} \frac{\cosh[k(d + x_z - h)]}{\cosh(kd)} \cos(k\vec{x} - \omega t). \tag{2.64}$$

In the case of extremely violent waves, where linear theory is insufficient, it may be necessary to relax this condition and specify only the velocity in order to achieve a more stable model. A better option would be to improve the boundary conditions to use a higher-order representation and some success was achieved by using Stokes' second order theory for the water surface elevation:

$$\eta(t,x) = \frac{H}{2}\cos(kx - \omega t) + \frac{H^2}{4}k\cos\left(2(kx - \omega t)\right). \tag{2.65}$$

Four boundary conditions were developed based on the theory above:

- A regular wave boundary condition in which equations 2.63–2.65 are applied without modification.
- A focussed wave group boundary which generates a focussed wave group based on the JONSWAP spectrum by summing the results of equation 2.64 for a large number of wave components generated from equation 2.34.
- A focussed wave group boundary which generates a focussed wave group based on a user-supplied amplitude spectrum.

- An irregular wave boundary which generates an irregular wave series based on user-supplied amplitude and phase spectra.

# 3 WAVE PROPAGATION OVER BARS

## 3.1 Validation Tests

Before any attempt is made to validate complex wave propagation and breaking behaviour in the "interFoam" code it is important to verify that the wave decay effect reported by Westphalen *et al.* (2007) is not an issue in OpenFOAM and that the code is capable of accurately propagating waves along an unobstructed, flat flume.

Accordingly a model was constructed with a 90 m numerical flume and a water depth of 0.86 m. As will be seen, this is the same model geometry as used for the "Dingemans" test case, below, but without the submerged breakwater. A wave with period 3.571 s, height 0.058 m and length 9.901 m was introduced (this is identical to the "Dingemans" (b) case) and the wave propagation was investigated. The results were very promising and are shown in figure 3.1. The red line shows the water surface elevation time series at a point 5 m in front of the wave-generating boundary. It can be seen that a clean, regular wave is being generated. The blue line shows the equivalent time series 60 m along the flume. It can be seen that the wave is slightly distorted initially (this is to be expected as the wave will naturally lose some energy as it propagates through the still water of the flume) but then settles into a similar pattern. The end of the series is similarly distorted by wave reflections from the end of the flume. In all, it can be seen that the "interFoam" code is capable of transmitting waves through a distance of at least 60 m without any appreciable loss of wave height.

In order to demonstrate that the "interFoam" model is capable of modelling complex wave transformation processes in shallow water with violent and, indeed, breaking waves, two test cases are now presented in this chapter. The first is the well-known test case of Beji & Battjes (1993), later repeated by Luth in 1994 and sometimes referred to in the literature as the "Dingemans" test case. This test case follows the propagation and

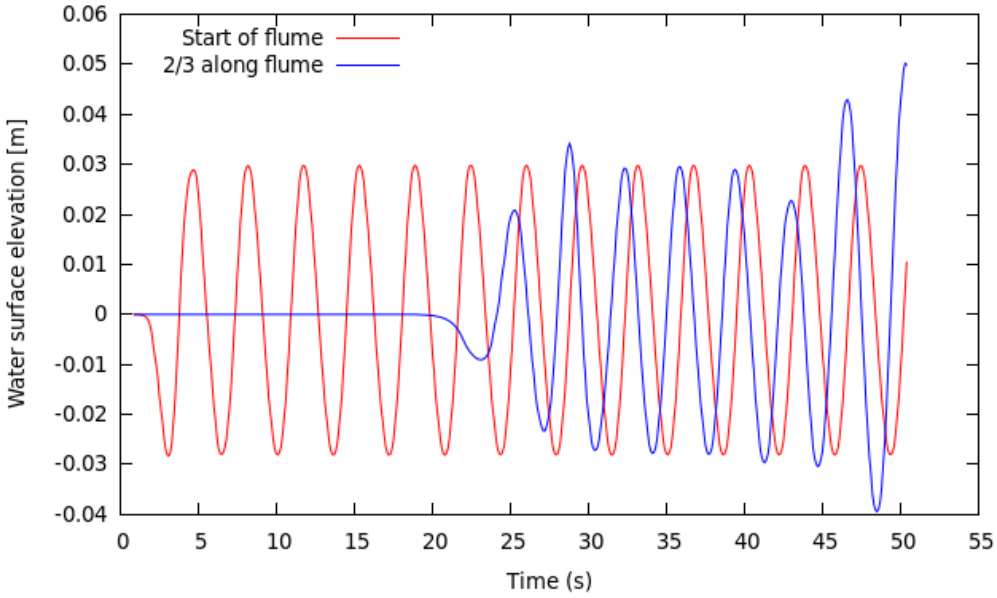


Figure 3.1: Graph showing water surface elevation time series at two points along an empty flume with a propagating wave.

transformation of regular waves over a submerged breakwater structure and has been widely used for the validation of Boussinesq-type models (see e.g. Gobbi & Kirby (1999)). The second test case models the transformation of a focussed wave group over a submerged bar and is based on a series of experiments conducted at the Danish Hydraulic Institute (DHI) in 2010 and described by Zang *et al.* (2010).

## 3.2 "Dingemans" Test Case

### Description of case

The experiment was conducted in a wave flume of length 45.0 m with a submerged breakwater of the shape shown in figure 3.2. The precise shape of the breakwater is given by the profile in table 3.1. The water level was recorded at the eleven locations shown in the figure.

Three different regular waves were used, referred to as cases (a), (b) and (c). The wave parameters are shown in table 3.2. It can be seen that two of the waves break as they pass over the breakwater. Case (b) is a long, high amplitude wave that breaks about half-way along the breakwater crest. Case (c) is much steeper with a much shorter wavelength

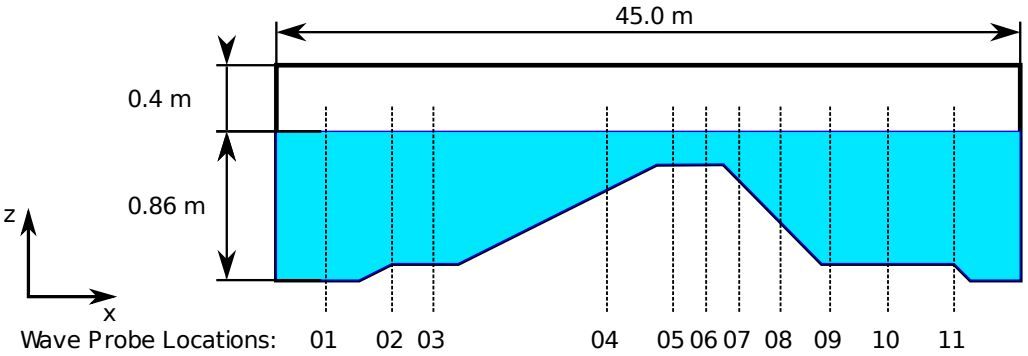


Figure 3.2: Schematic of the geometry of the "Dingemans" test case showing breakwater shape and positions of wave gauges. Horizontal scale reduced ten times.

| $x$ | $z$ |
|---|---|
| 0.00 | -0.86 |
| 5.22 | -0.86 |
| 6.42 | -0.80 |
| 11.01 | -0.80 |
| 23.04 | -0.20 |
| 27.04 | -0.20 |
| 33.07 | -0.80 |
| 40.61 | -0.80 |
| 41.82 | -0.86 |

Table 3.1: Bed elevations in metres below mean water level recorded at changes in bed gradient in the "Dingemans" test case.

and lower amplitude than case (b). As it passes over the breakwater it is right on the limit of breaking.

## Validation results

The results from the model were compared with the experimental data in a number of ways. Graphs showing the modelled water surface elevations (in red) compared to the experimental water surface elevations (in blue) at several wave probe locations shown in figure 3.2 are presented below. Similar graphs for all of the locations are presented in appendix A.

| Case ID | Period, T (s) | Wave Height, H (m) | Wave Length, L (m) | Steepness, H/L (m/m) | Breaking? |
|---|---|---|---|---|---|
| (a) | 2.857 | 0.04 | 7.727 | 0.0052 | No |
| (b) | 3.571 | 0.058 | 9.901 | 0.0059 | Yes |
| (c) | 1.428 | 0.082 | 3.012 | 0.0272 | Yes |

Table 3.2: Wave parameters used in the "Dingemans" test case.

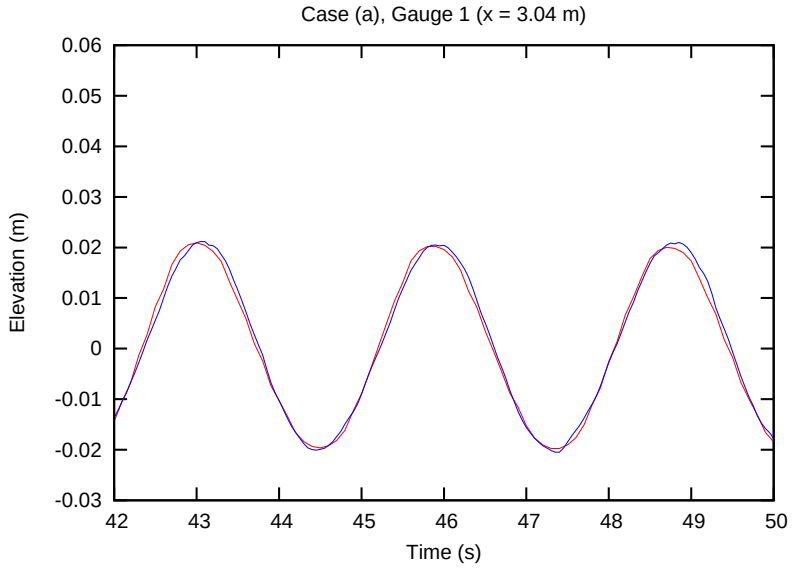


Figure 3.3: Graph showing the observed (blue line) and modelled (red line) elevation time series at wave gauge 1 for case A.

### Case A

Case A is the smallest of the three wave cases and it should therefore be expected to yield a reasonable agreement with the experiment.

It can be seen from figures 3.3–3.7 that the modelled results agree well with the experimental results . The model is, as expected, more accurate at the earlier gauges than at the later ones, but the total model error is very small.

Figures 3.8–3.12 show the amplitude frequency spectra for each wave probe. These frequency spectra were obtained by trimming the modelled and experimental time series between 33 s and 58 s and applying the Fast Fourier Transform (FFT) algorithm. This time period was chosen as it is the period for which all of the gauges in the experiment experience an

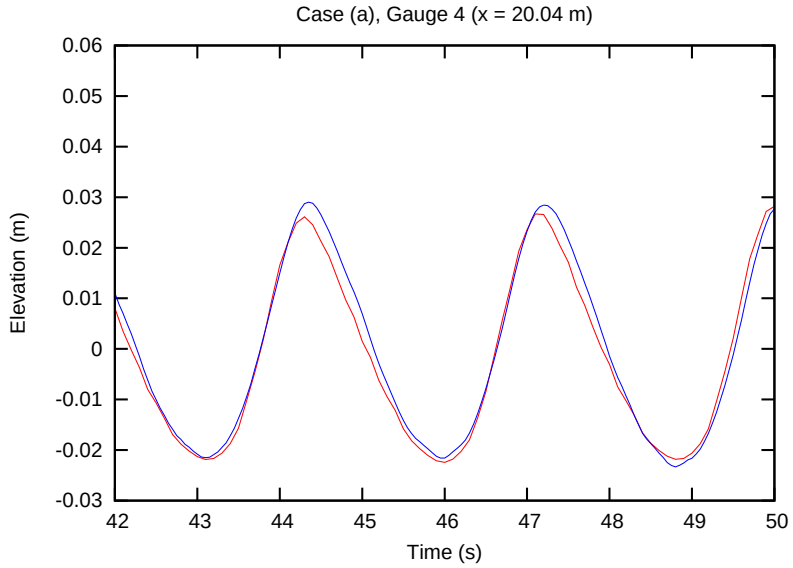


Figure 3.4: Graph showing the observed (blue line) and modelled (red line) elevation time series at wave gauge 4 for case A.

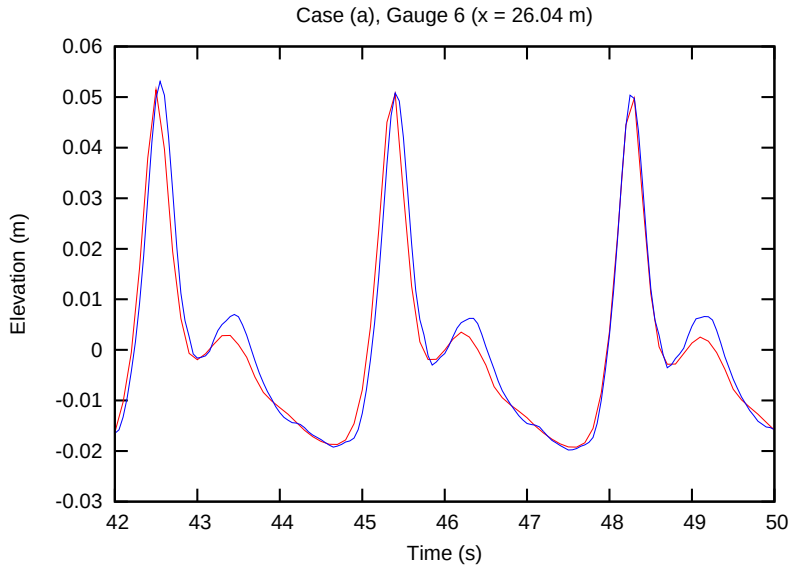


Figure 3.5: Graph showing the observed (blue line) and modelled (red line) elevation time series at wave gauge 6 for case A.

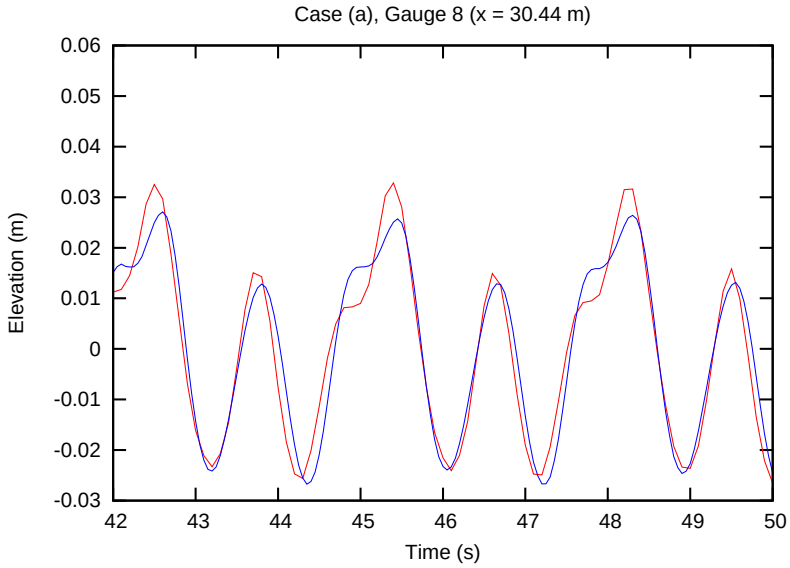


Figure 3.6: Graph showing the observed (blue line) and modelled (red line) elevation time series at wave gauge 8 for case A.

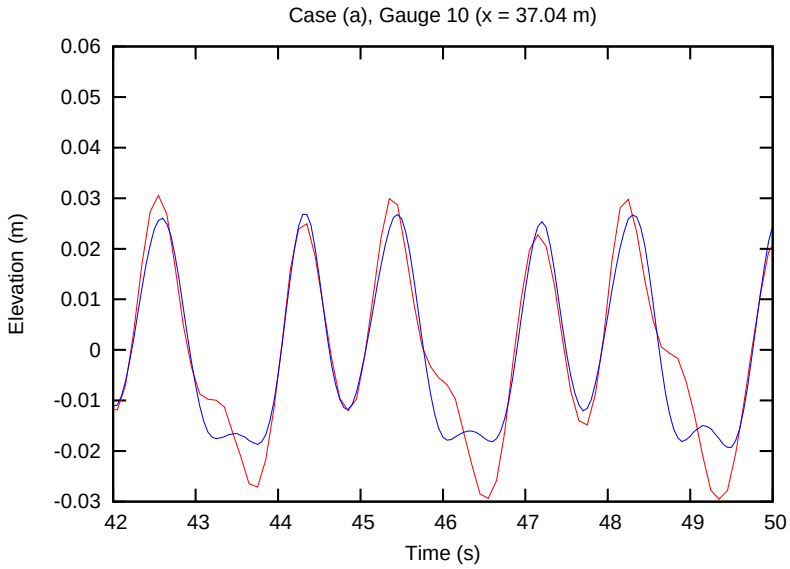


Figure 3.7: Graph showing the observed (blue line) and modelled (red line) elevation time series at wave gauge 10 for case A.

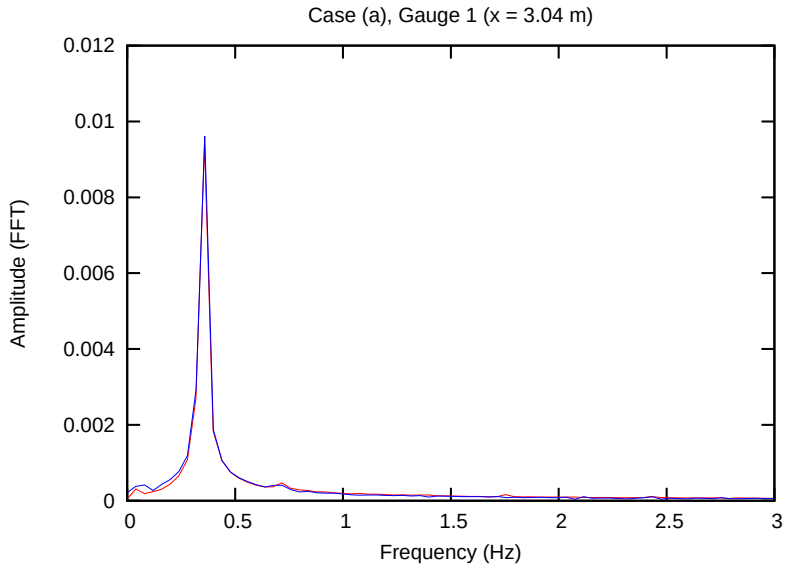


Figure 3.8: Graph showing the experimental (blue line) and modelled (red line) frequency spectra at wave gauge 1 for case A.

undisturbed wave field (i.e. the time from which waves are fully developed at gauge 11 to the point just before the field at gauge 11 becomes contaminated by reflection from the downstream limit of the model).

It can be seen that the model correctly represents the frequency and amplitude of all the major harmonics which are present (up to the seventh harmonic in the case of gauge 6).

These results are to be expected: case A is a very small-amplitude wave. It is not violent or breaking and can generally be reasonably well represented using simpler Boussinesq-type models. (Gobbi & Kirby 1999)

### Case B

Case B is the longest wave of the three cases and is also both larger and steeper than case A. This leads to a more violent wave-structure interaction and a more non-linear wave.

It can be seen from figures 3.13–3.17 that the agreement in water surface elevation is very good up to the top of the embankment, but begins to deteriorate slightly on the back face of the embankment.

By plotting the frequency spectra (figures 3.18–3.22) for this case, we can see why the modelled wave transformation for this more violent wave is not as accurate. While the modelled surface water elevation is

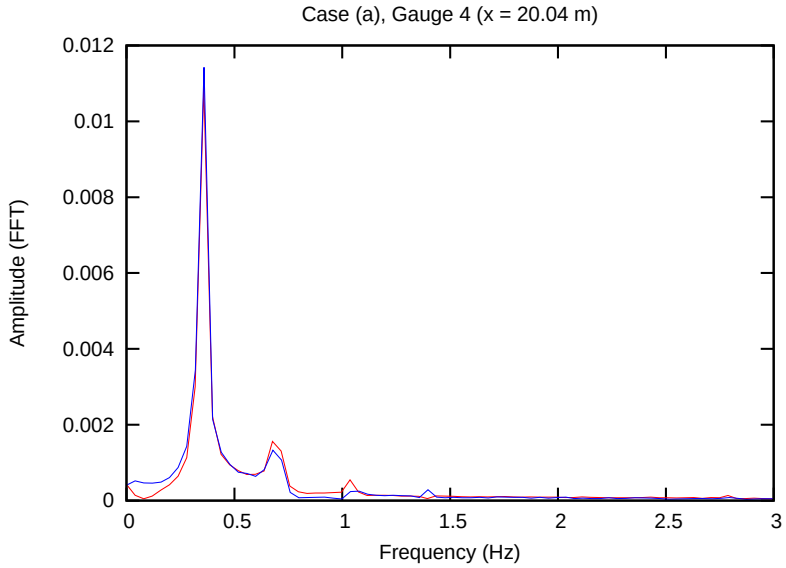


Figure 3.9: Graph showing the experimental (blue line) and modelled (red line) frequency spectra at wave gauge 4 for case A.

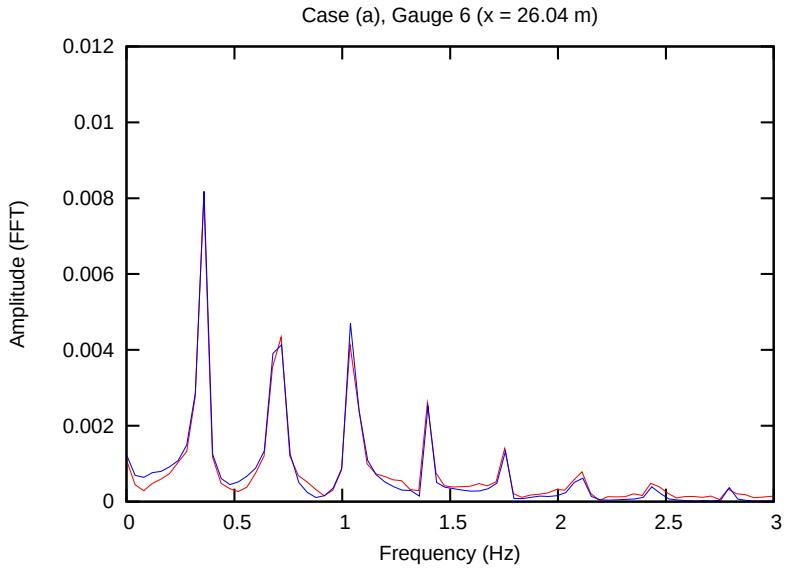


Figure 3.10: Graph showing the experimental (blue line) and modelled (red line) frequency spectra at wave gauge 6 for case A.

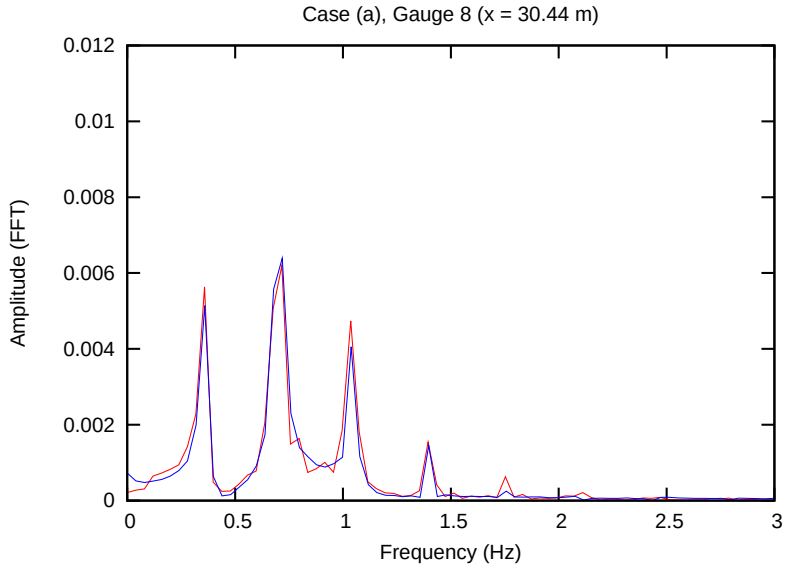


Figure 3.11: Graph showing the experimental (blue line) and modelled (red line) frequency spectra at wave gauge 8 for case A.

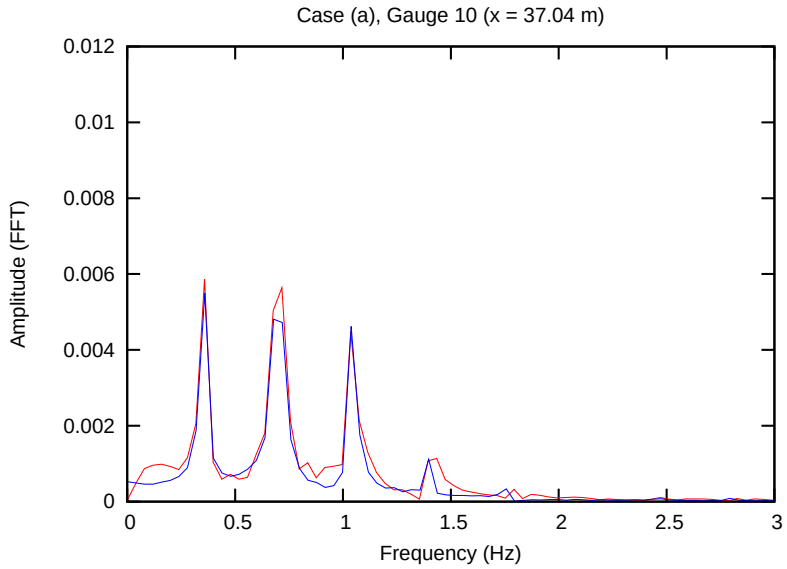


Figure 3.12: Graph showing the experimental (blue line) and modelled (red line) frequency spectra at wave gauge 10 for case A.

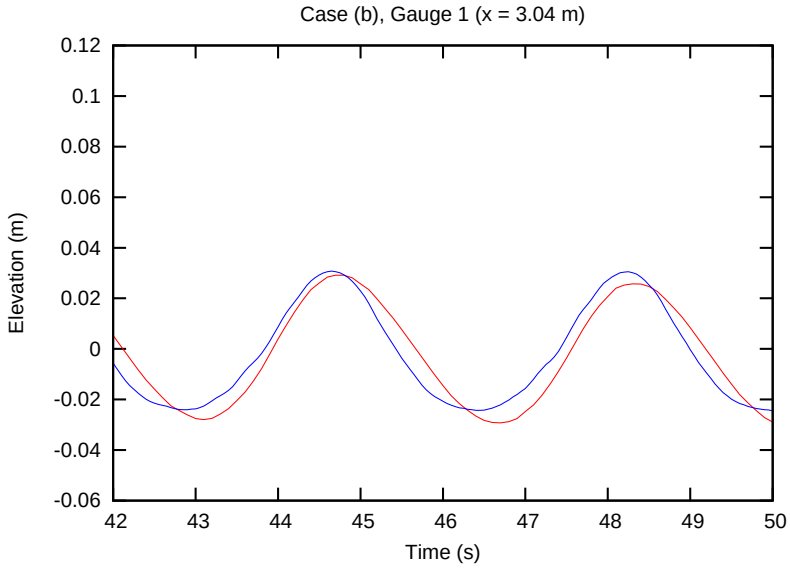


Figure 3.13: Graph showing the observed (blue line) and modelled (red line) elevation time series at wave gauge 1 for case B.

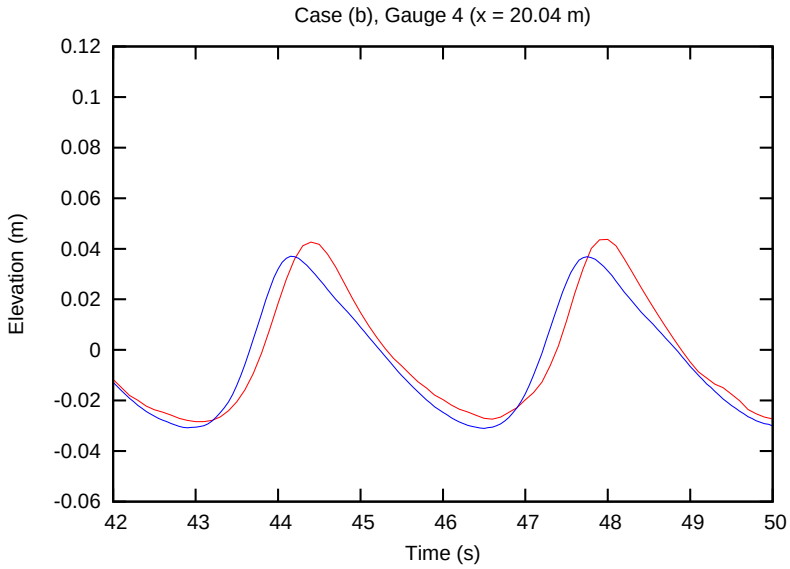


Figure 3.14: Graph showing the observed (blue line) and modelled (red line) elevation time series at wave gauge 4 for case B.

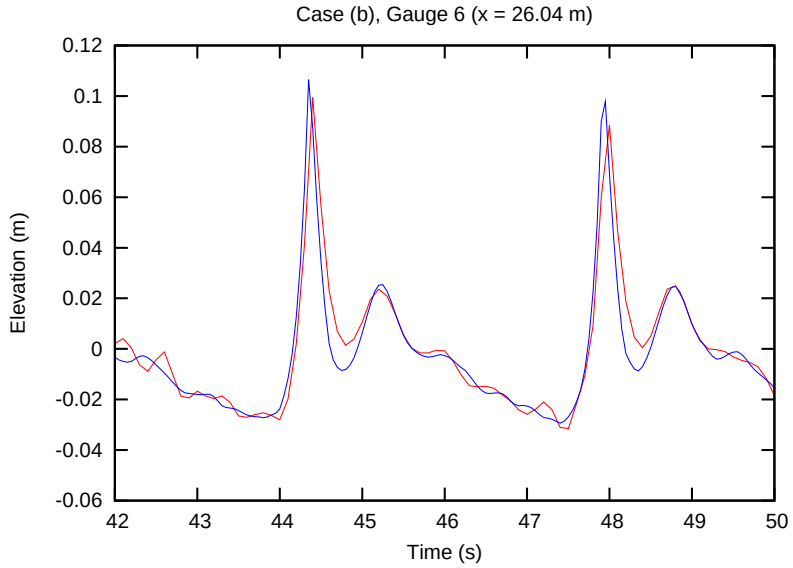


Figure 3.15: Graph showing the observed (blue line) and modelled (red line) elevation time series at wave gauge 6 for case B.

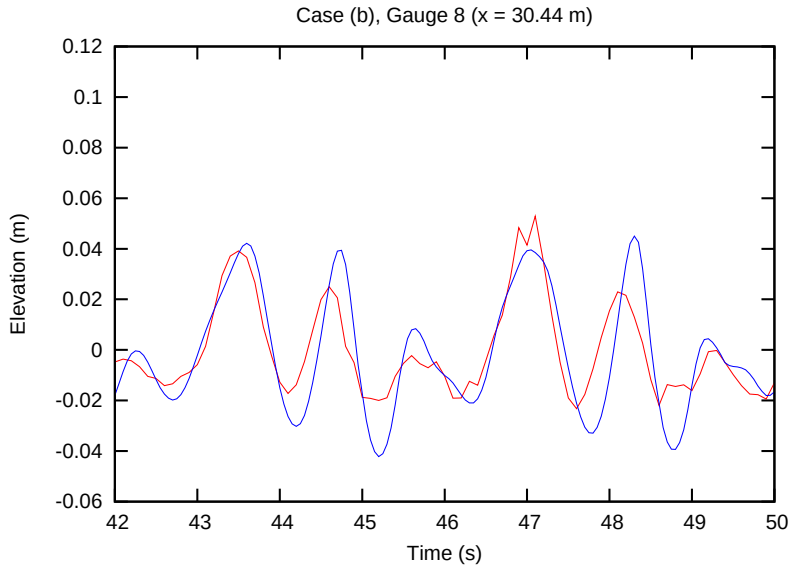


Figure 3.16: Graph showing the observed (blue line) and modelled (red line) elevation time series at wave gauge 8 for case B.

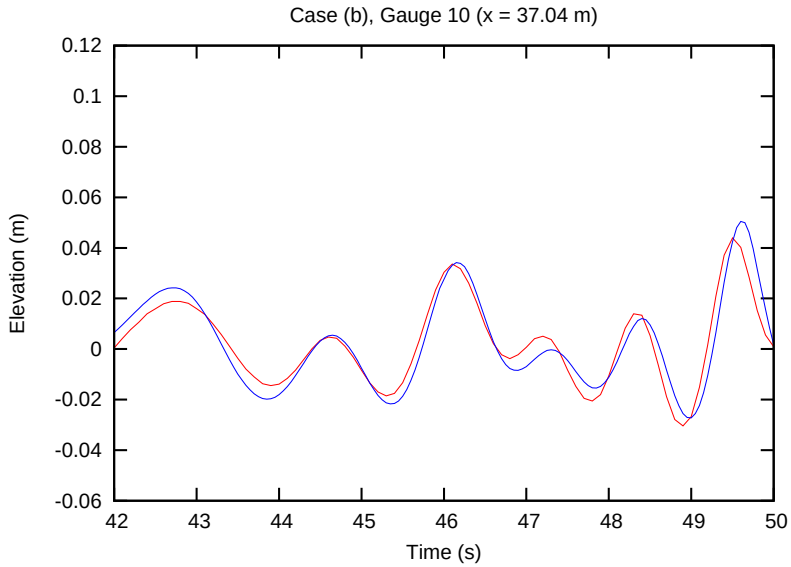


Figure 3.17: Graph showing the observed (blue line) and modelled (red line) elevation time series at wave gauge 10 for case B.

not quite accurate for gauges 1–4, it can be seen that the wave spectra are represented to a reasonable level of accuracy. It is likely that this slight inaccuracy is due to the difference in wave generation methodology between the experimental and the modelled results.

For gauges 5–6, good agreement is achieved both in the water surface and spectrum plots with a slight underestimation of the fourth and higher order terms at gauge 6. It is at gauge 7, both in the surface elevation and spectral plots where the agreement between the model and the experimental data begins to break down. We can see from the spectrum plots that this inaccuracy is concentrated in the third and fourth order terms which have begun to dominate the wave climate. It has been found that the representation of these higher-order waves improves with mesh density suggesting a conclusion that there is a minimum mesh density or maximum timestep required to model waves of a particular frequency. This is discussed further below.

### Case C

Case C is the steepest and most non-linear wave under consideration. It can be seen from figures 3.23–3.27 and 3.28–3.32 that, like case B, the agreement between the experimental and modelled results is generally

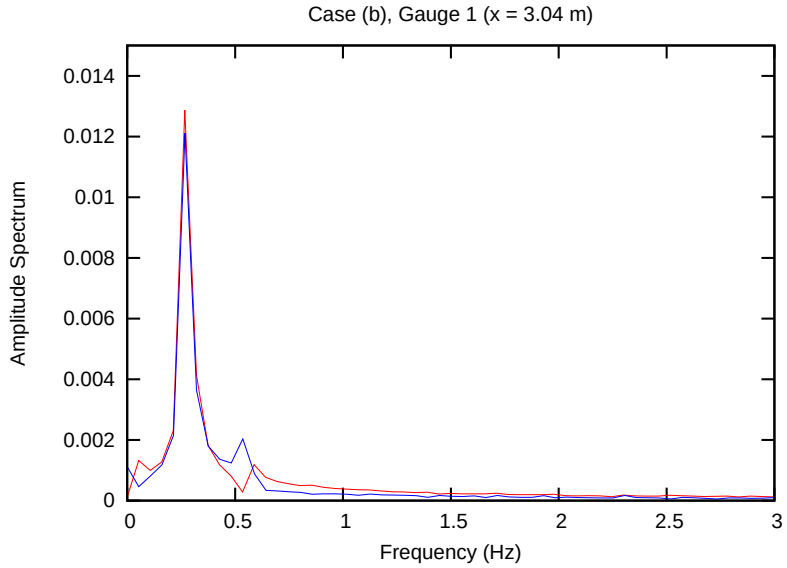


Figure 3.18: Graph showing the experimental (blue line) and modelled (red line) frequency spectra at wave gauge 1 for case B.

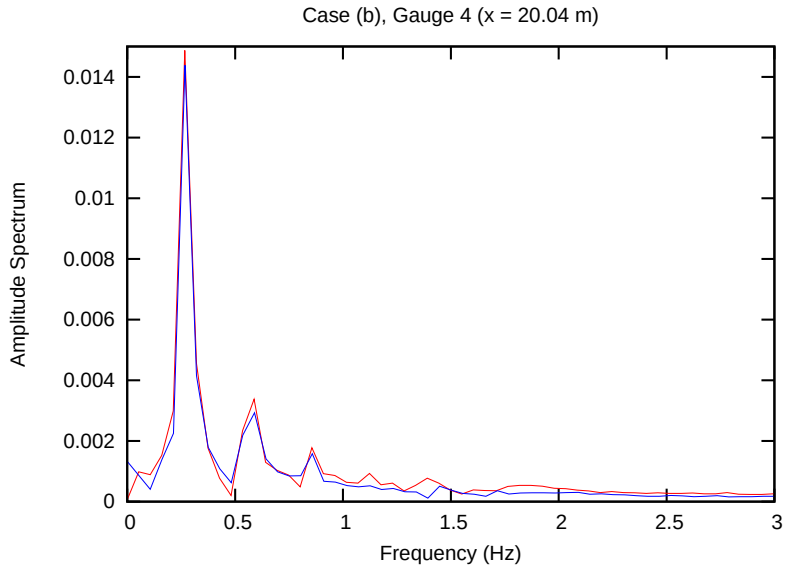


Figure 3.19: Graph showing the experimental (blue line) and modelled (red line) frequency spectra at wave gauge 4 for case B.

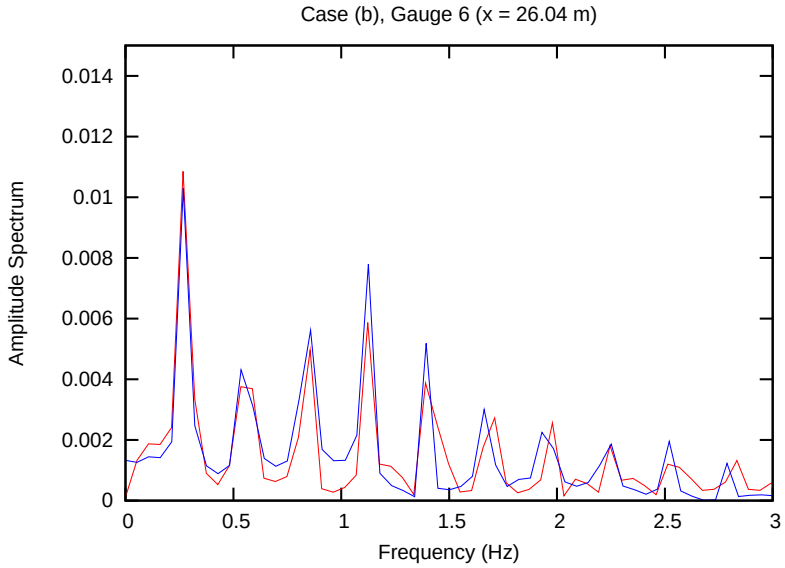


Figure 3.20: Graph showing the experimental (blue line) and modelled (red line) frequency spectra at wave gauge 6 for case B.

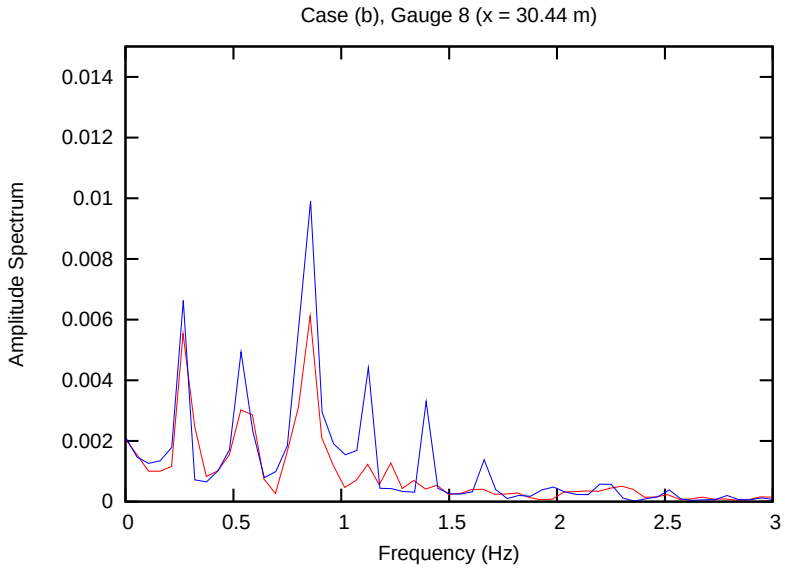


Figure 3.21: Graph showing the experimental (blue line) and modelled (red line) frequency spectra at wave gauge 8 for case B.

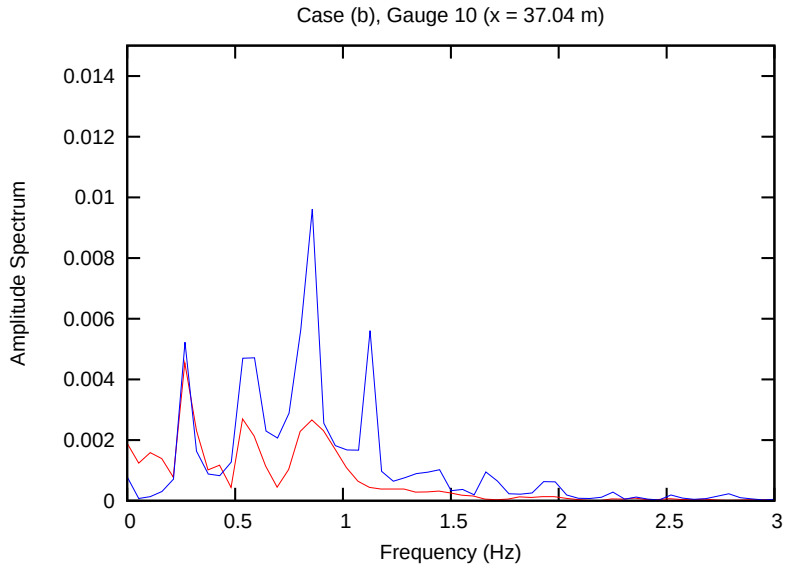


Figure 3.22: Graph showing the experimental (blue line) and modelled (red line) frequency spectra at wave gauge 10 for case B.

good, but the model struggles to transmit the high frequency wave components generated as the wave passes the top of the embankment.

Figure 3.33 shows snapshots of the modelled water surface elevation along the flume at various times for cases (b) and (c). The scale has been compressed by a factor of 5 in the horizontal direction for reasons of space and clarity. It can be seen that case (b) breaks about half way along the crest of the breakwater and air-entrainment is visible. In case (c) the wave is just breaking as can be seen by the roughness of the modelled water surface on top of the breakwater. It can be seen that these very small waves propagate backwards and interact with the subsequent incoming waves.

## 3.3 Sensitivity and Convergence

### Mesh density

The sensitivity of the model to the refinement and density of the mesh was assessed by constructing four different meshes. These meshes were labelled A, B, C and D and their basic parameters are given in figures 3.34–3.37.

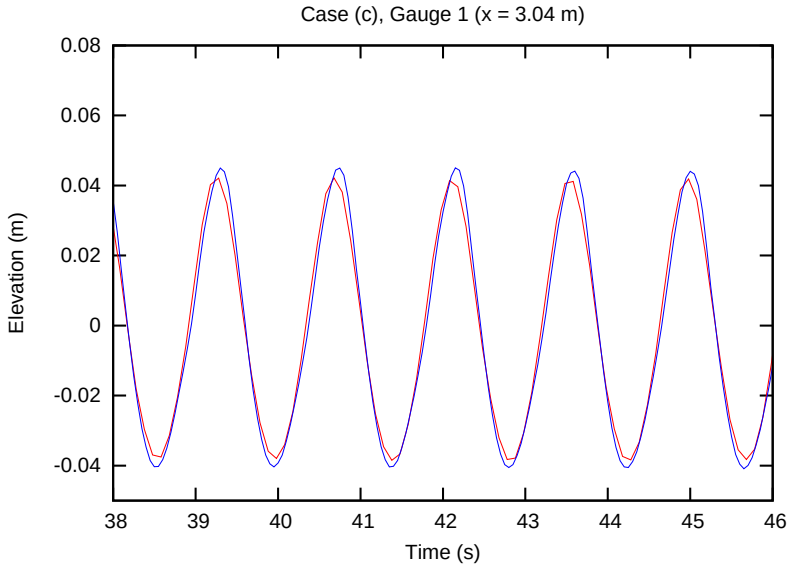


Figure 3.23: Graph showing the observed (blue line) and modelled (red line) elevation time series at wave gauge 1 for case C.

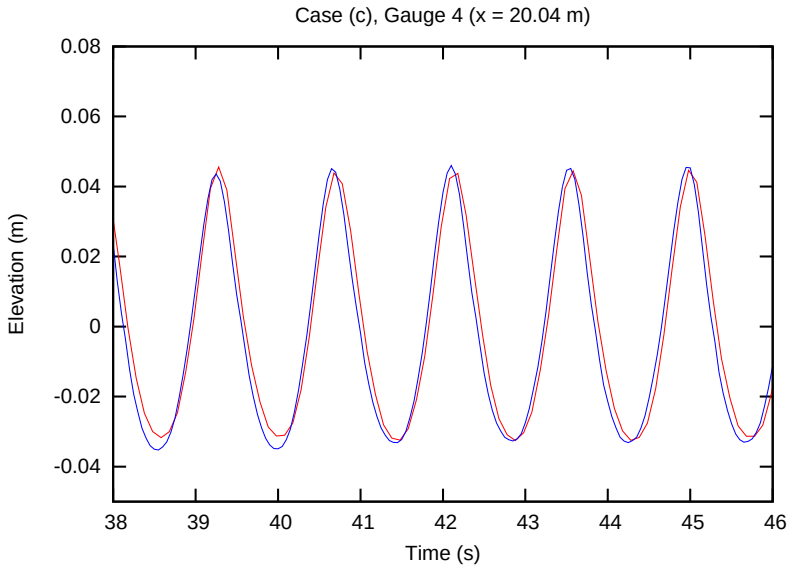


Figure 3.24: Graph showing the observed (blue line) and modelled (red line) elevation time series at wave gauge 4 for case C.

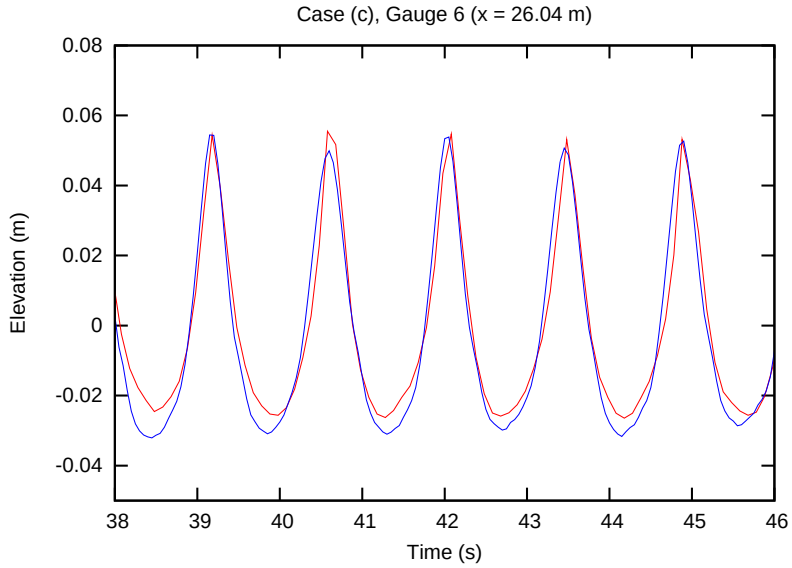


Figure 3.25: Graph showing the observed (blue line) and modelled (red line) elevation time series at wave gauge 6 for case C.

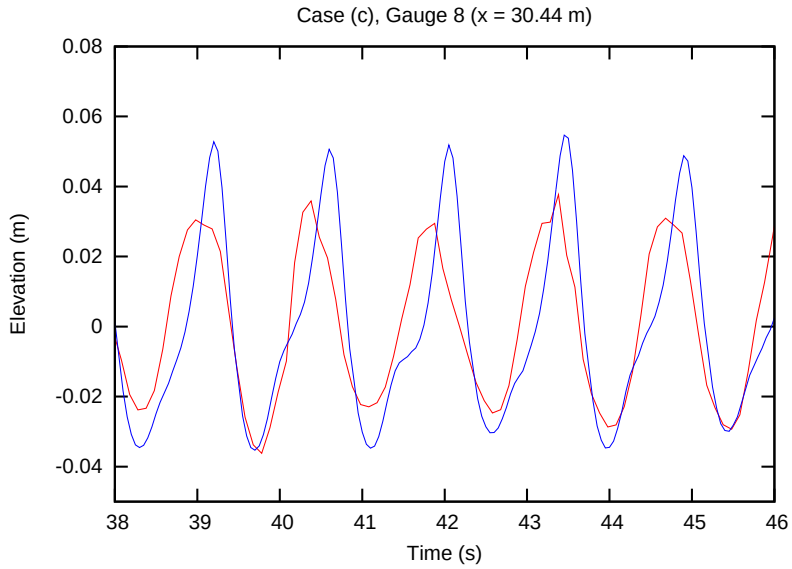


Figure 3.26: Graph showing the observed (blue line) and modelled (red line) elevation time series at wave gauge 8 for case C.

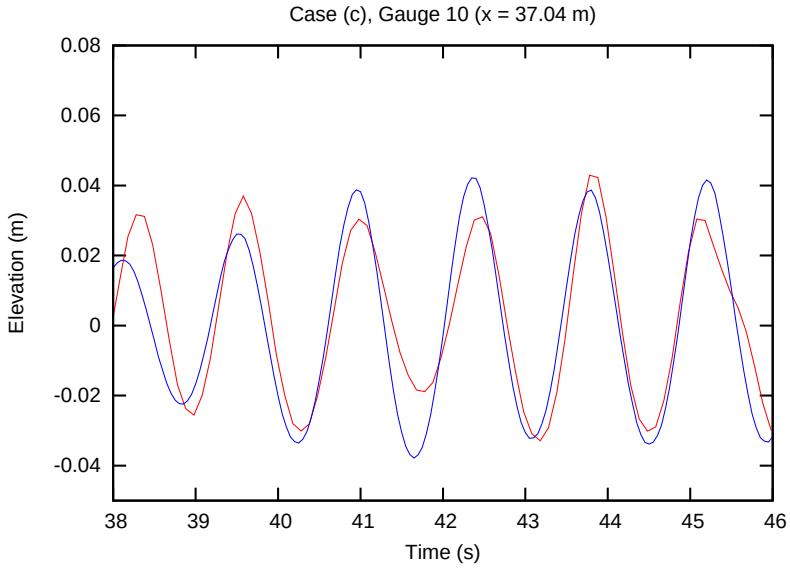


Figure 3.27: Graph showing the observed (blue line) and modelled (red line) elevation time series at wave gauge 10 for case C.

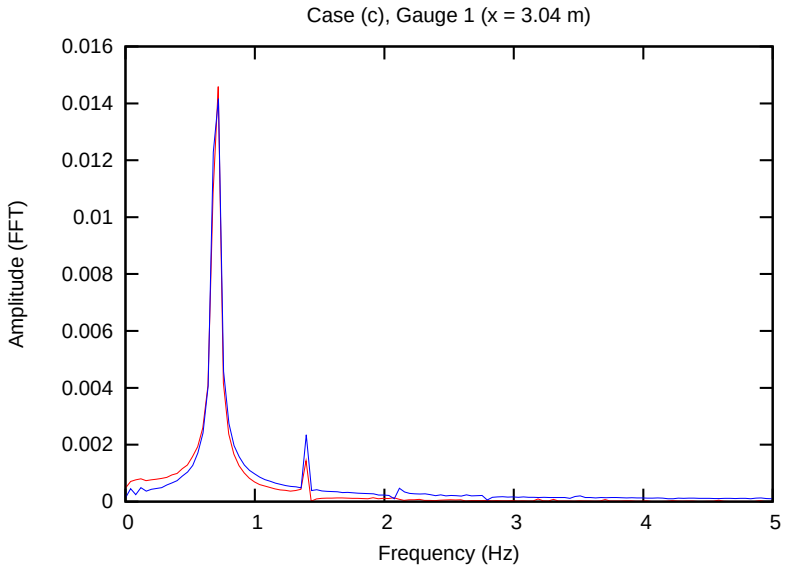


Figure 3.28: Graph showing the experimental (blue line) and modelled (red line) frequency spectra at wave gauge 1 for case C.

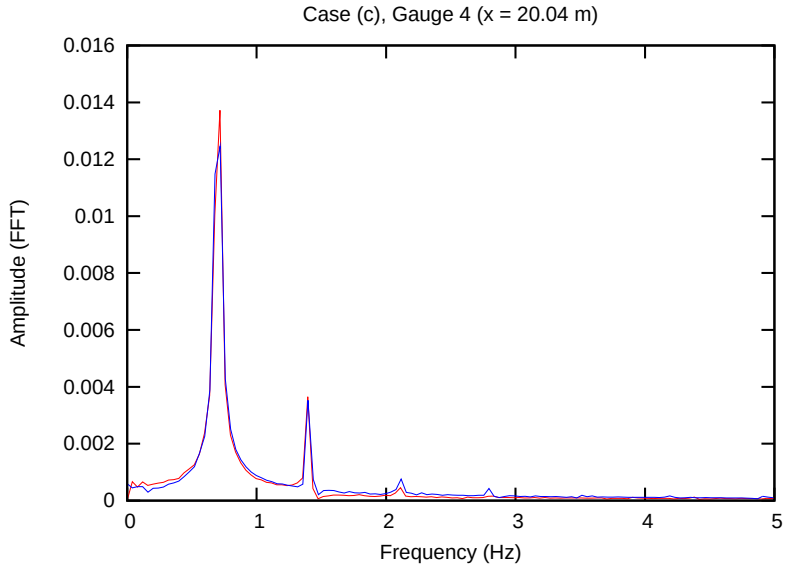


Figure 3.29: Graph showing the experimental (blue line) and modelled (red line) frequency spectra at wave gauge 4 for case C.

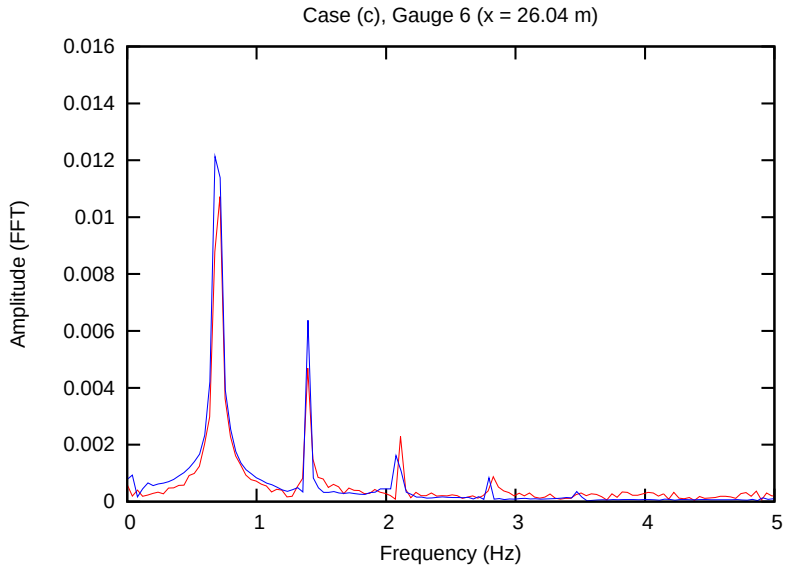


Figure 3.30: Graph showing the experimental (blue line) and modelled (red line) frequency spectra at wave gauge 6 for case C.

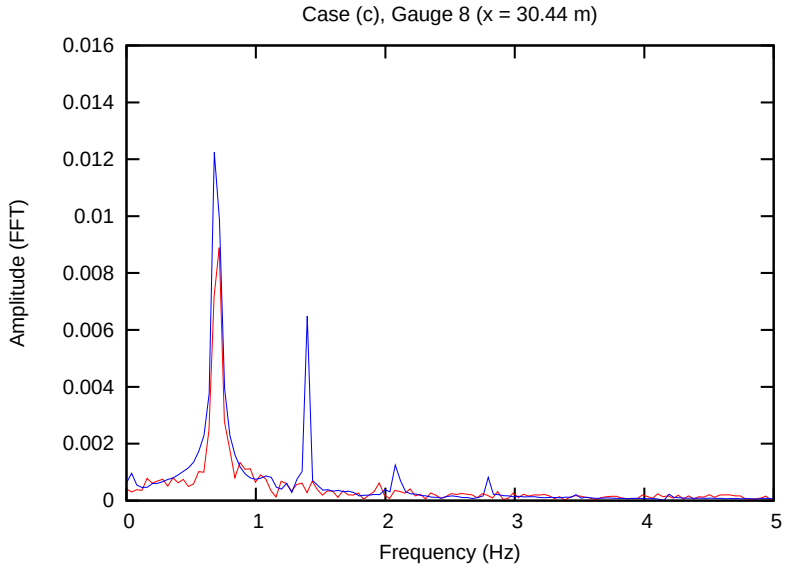


Figure 3.31: Graph showing the experimental (blue line) and modelled (red line) frequency spectra at wave gauge 8 for case C.

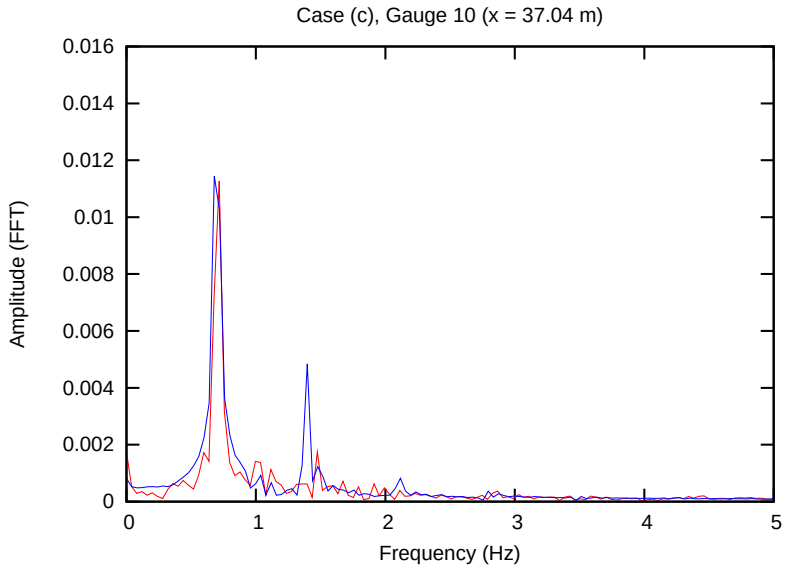


Figure 3.32: Graph showing the experimental (blue line) and modelled (red line) frequency spectra at wave gauge 10 for case C.

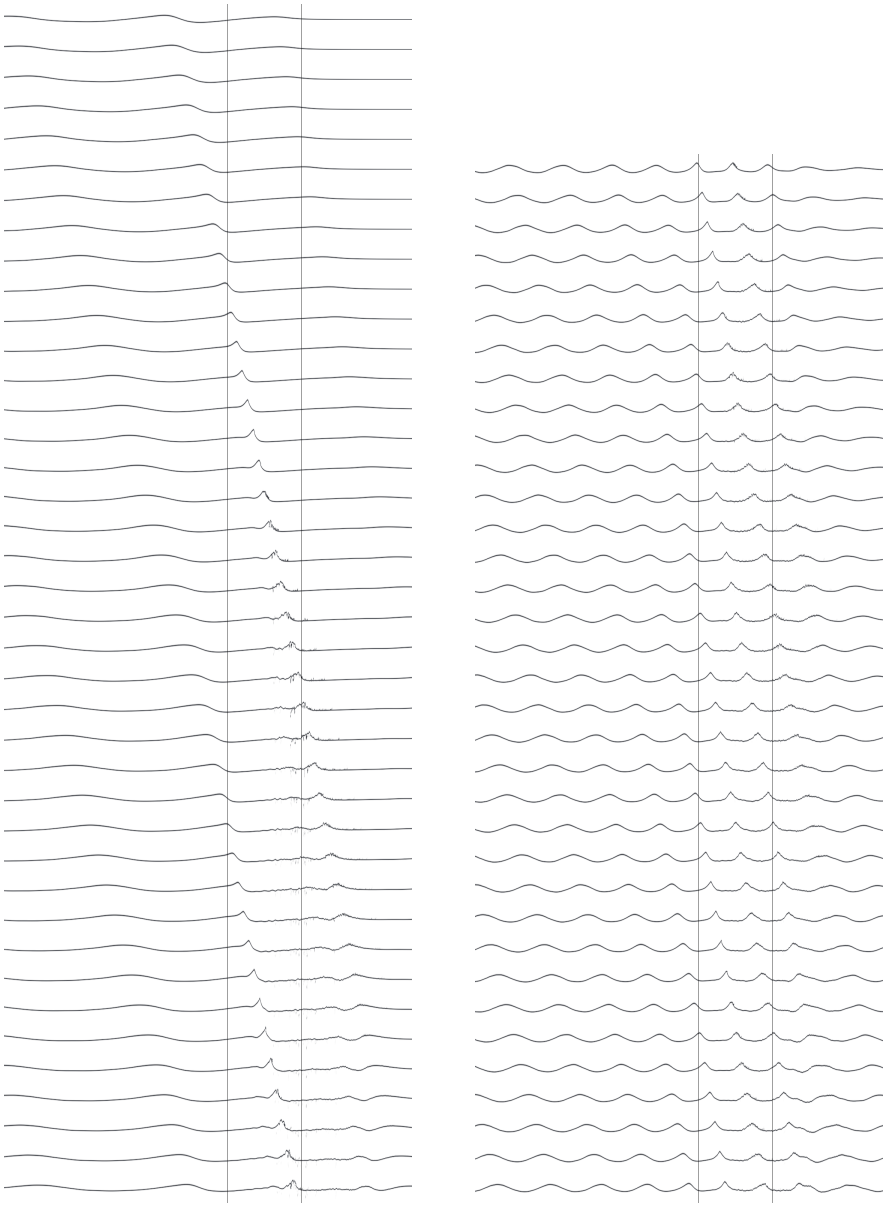

Figure 3.33: Snapshots of the water surface in the "Dingemans" tests for case (b) (left) and (c) (right) at 0.2 s intervals with the two shoulders of the crest of the breakwater shown as vertical lines.

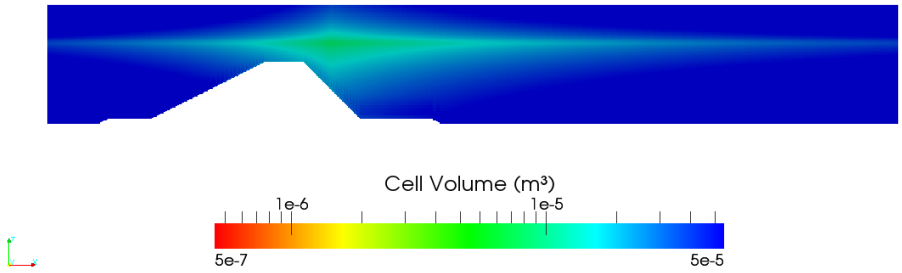


Figure 3.34: Mesh A: Base cell size of 0.02 m $\times$ 0.02 m with varying sizes in both dimensions.

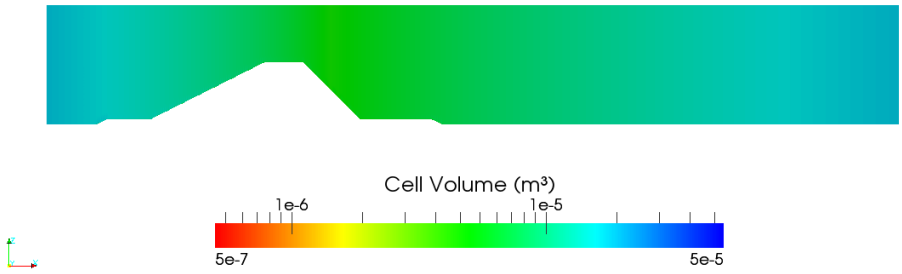


Figure 3.35: Mesh B: Base cell size of 0.01 m $\times$ 0.01 m with varying sizes in the x direction only.

It is possible to compare the water surface elevation results for each of these meshes, but it is difficult to observe qualitative changes in the results from this. Instead, to measure the convergence of the results with increasing mesh density, the total error in each of the first eight harmonic peaks in the amplitude wave spectra for each gauge were summed, producing a single "total model error" value. These error values are plotted against the total number of cells in the mesh in figure 3.38. It can be seen that as the total number of cells increases, the model error decreases. From the comparison between meshes B and C, which have very similar numbers of cells, it can be concluded that the surface refinement in meshes A and C increases the accuracy of the model even if the total number of cells (the overall mesh density) is not changed.

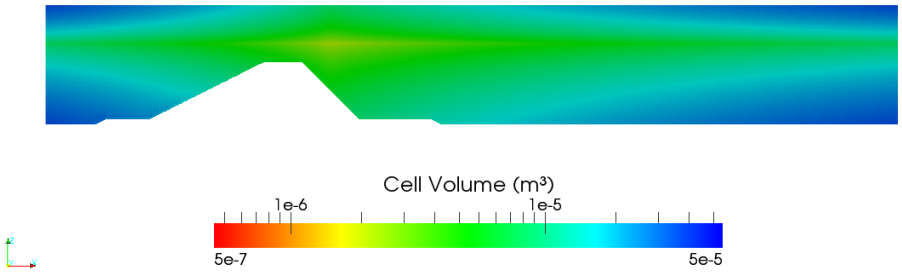


Figure 3.36: Mesh C: Base cell size of 0.01 m $\times$ 0.01 m with varying sizes in both dimensions.

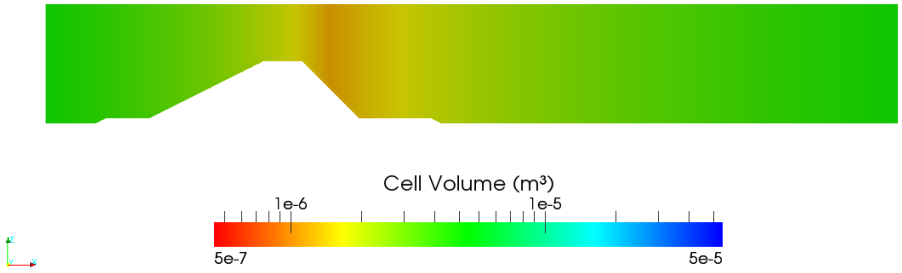


Figure 3.37: Mesh D: Base cell size of 0.005 m $\times$ 0.005 m with varying sizes in the x direction only.

## Discretisation scheme

Some researchers have concluded that it is desirable to use high-order discretisation schemes for the calculation of wave transformation and wave-structure interaction. In order to assess the need for this in the interFoam model a sensitivity analysis was performed, comparing the results from case (b) of the Dingemans test on mesh A using different discretisation schemes for the grad and laplacian terms of the Navier-Stokes equations. Two discretisation schemes were tested. The linear scheme used in the results above and throughout this report, and a semi-explicit cubic scheme. The comparison of the results from the two schemes is shown in figures 3.39–3.43. It can be seen from the figures that changing

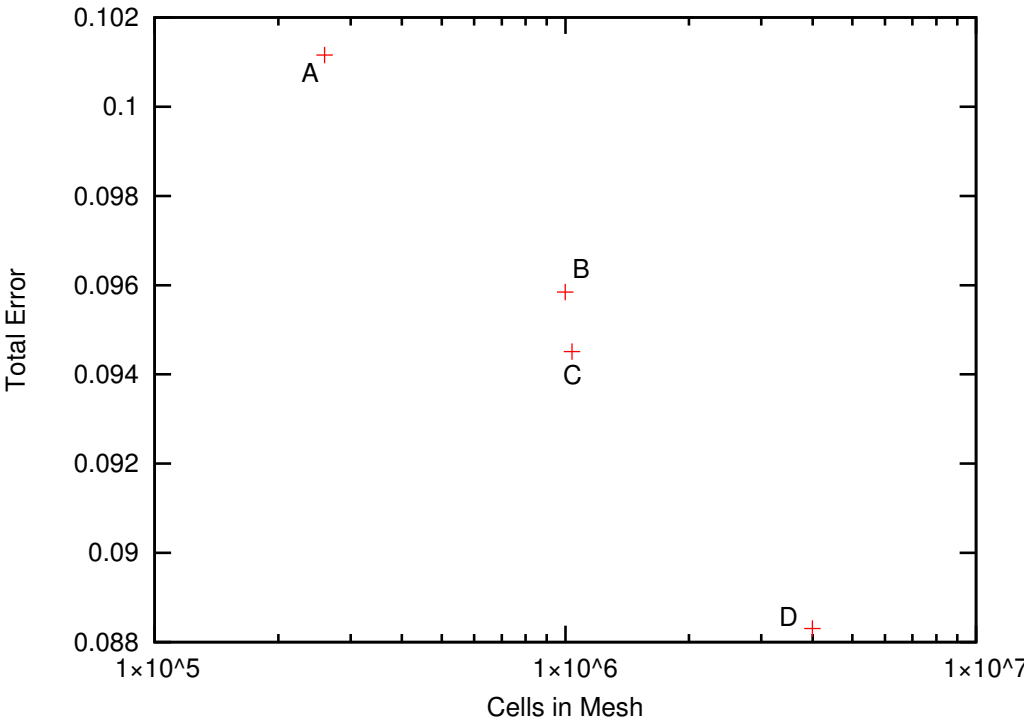


Figure 3.38: Diagram showing the total model error against the total number of cells for each mesh.

the discretisation scheme has very little effect on the shape of the wave.

## Momentum predictor step

The PISO scheme used by the interFoam models and discussed in section 2.1 has an initial momentum prediction step which, as noted by Issa (1985), while formally required, can often be neglected and the momentum results from the previous timestep used instead. To assess whether the additional computational expense of the momentum predictor step is required in this case, models were run using case (b) on mesh A with and without this momentum predictor step. The results are shown in figures 3.44–3.48. It can be seen that the momentum predictor step has very little effect on the shape of the wave form and it is therefore not unreasonable to neglect this solution step for this type of problem.

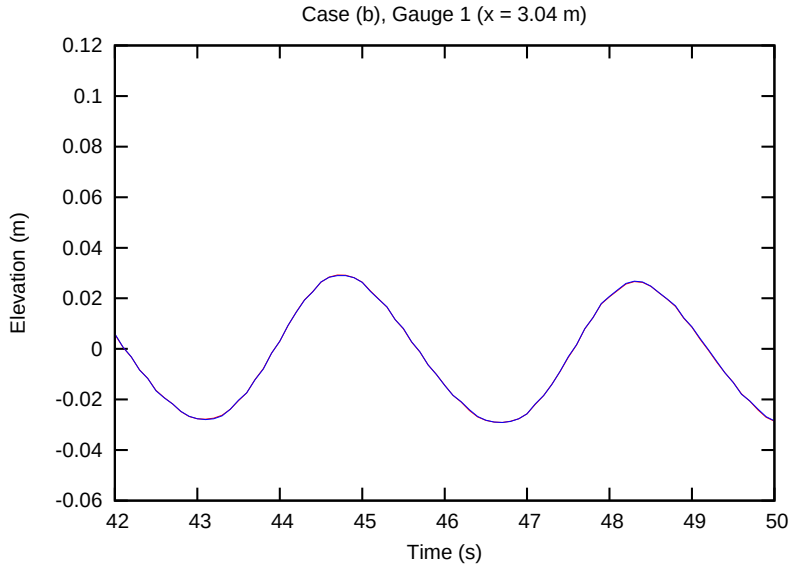


Figure 3.39: Graph showing modelled elevation time series using the linear scheme (red line) and cubic (blue line) at wave gauge 1 for case B.

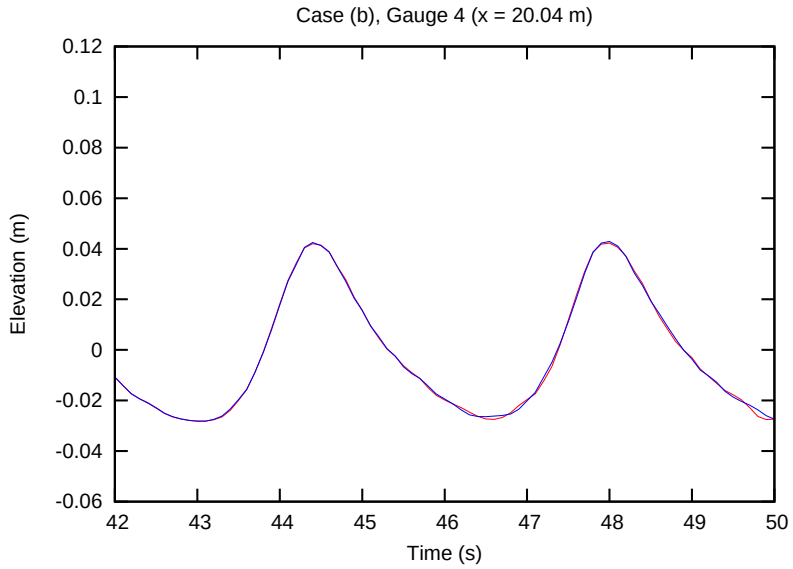


Figure 3.40: Graph showing modelled elevation time series using the linear scheme (red line) and cubic (blue line) at wave gauge 4 for case B.

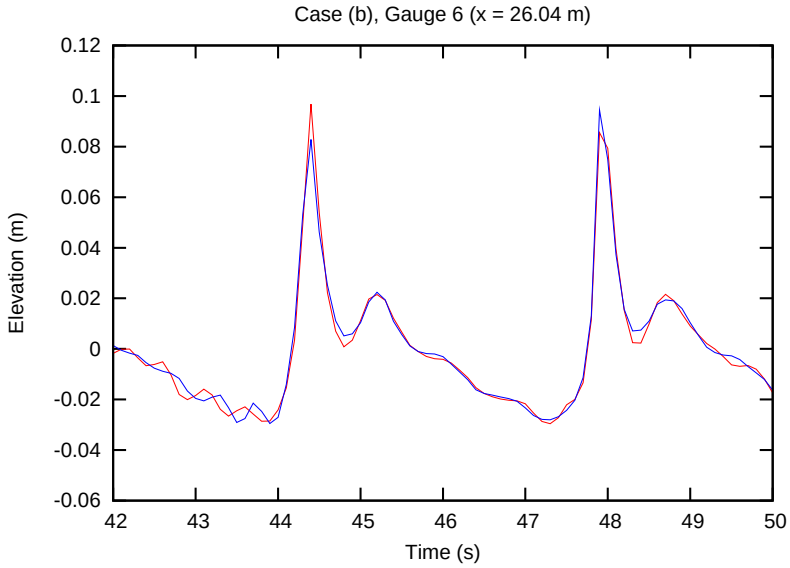


Figure 3.41: Graph showing modelled elevation time series using the linear scheme (red line) and cubic (blue line) at wave gauge 6 for case B.

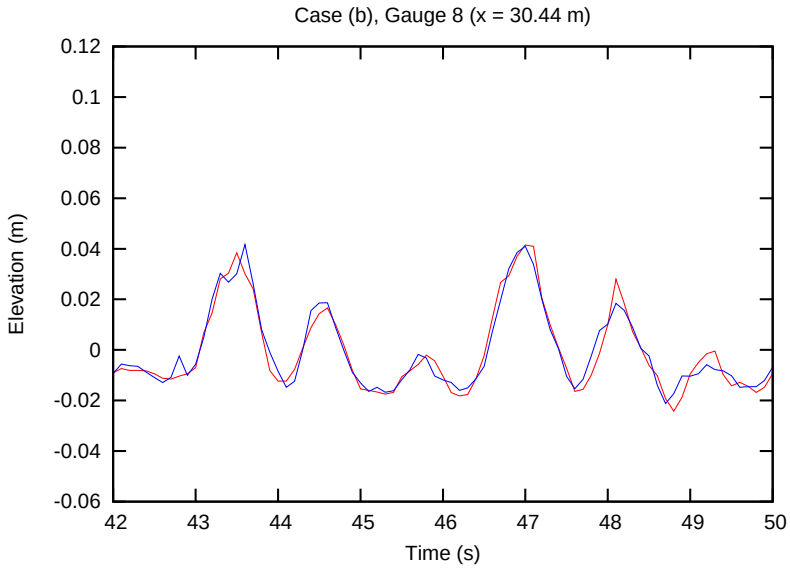


Figure 3.42: Graph showing modelled elevation time series using the linear scheme (red line) and cubic (blue line) at wave gauge 8 for case B.

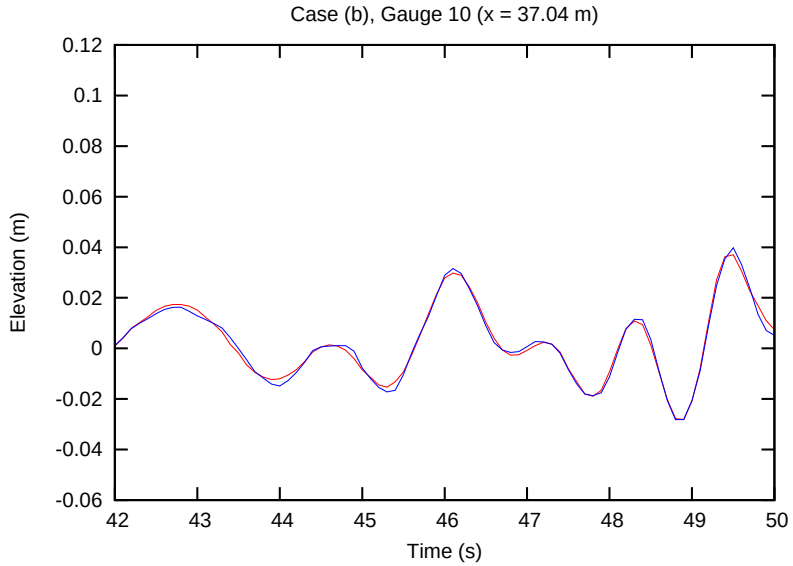


Figure 3.43: Graph showing modelled elevation time series using the linear scheme (red line) and cubic (blue line) at wave gauge 10 for case B.

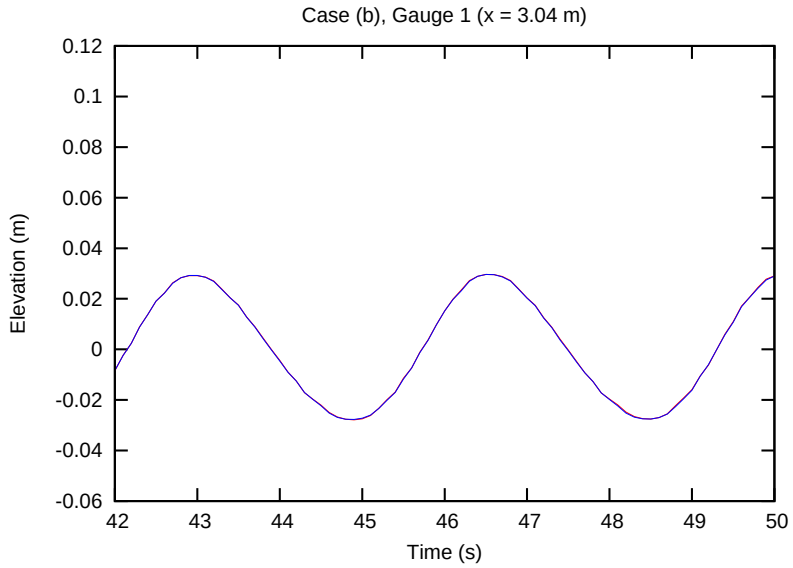


Figure 3.44: Graph showing modelled results with and without the momentum predictor step (blue and red lines respectively) at wave gauge 1 for case B.

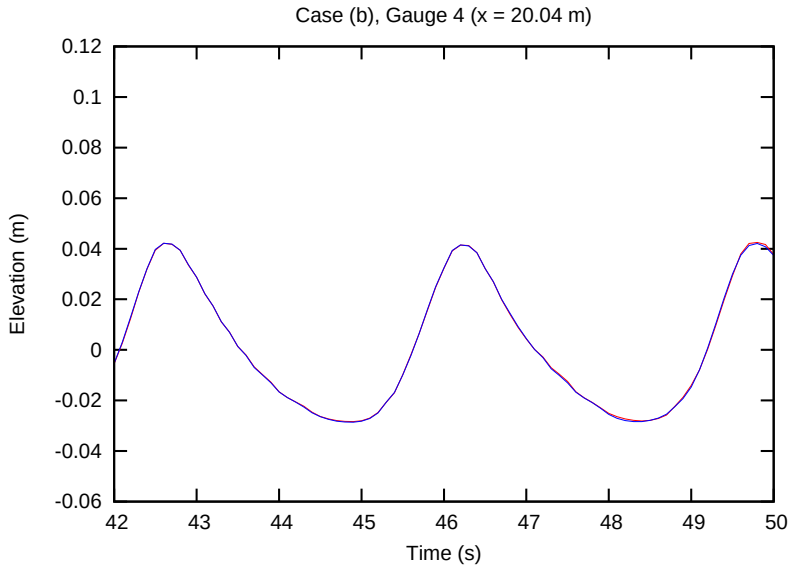


Figure 3.45: Graph showing modelled results with and without the momentum predictor step (blue and red lines respectively) at wave gauge 4 for case B.

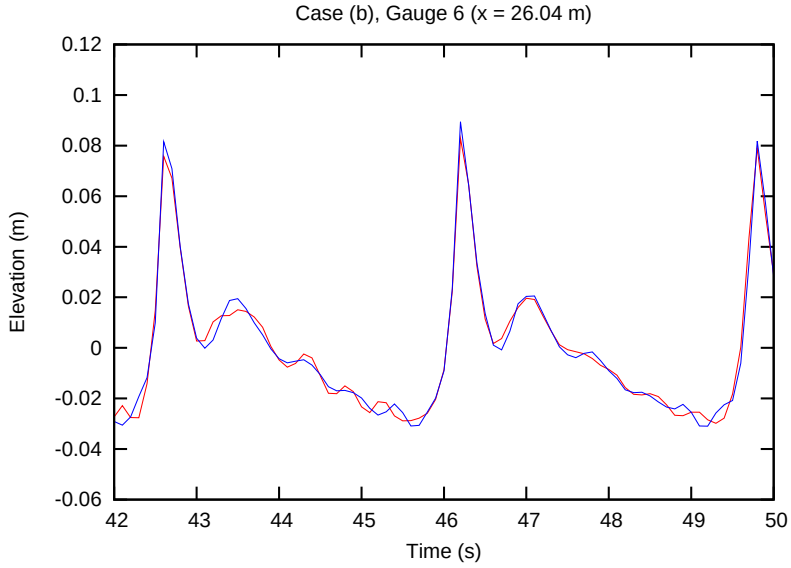


Figure 3.46: Graph showing modelled results with and without the momentum predictor step (blue and red lines respectively) at wave gauge 6 for case B.

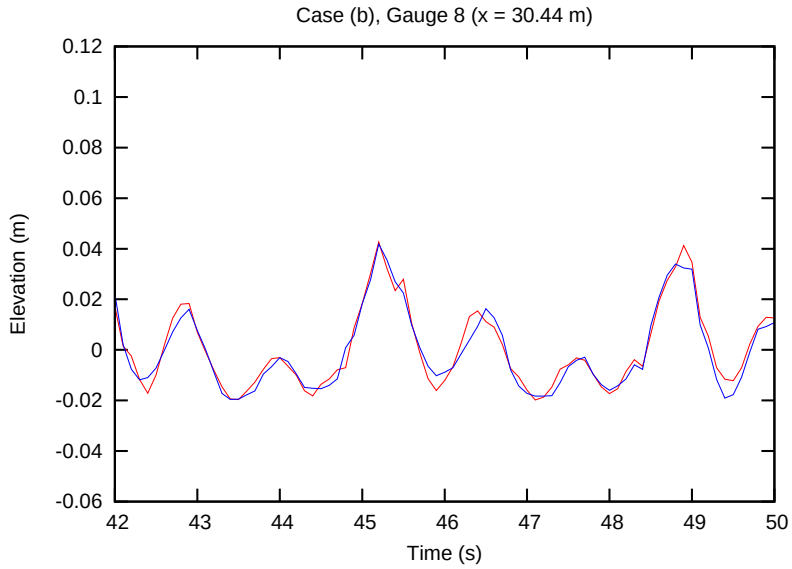


Figure 3.47: Graph showing modelled results with and without the momentum predictor step (blue and red lines respectively) at wave gauge 8 for case B.

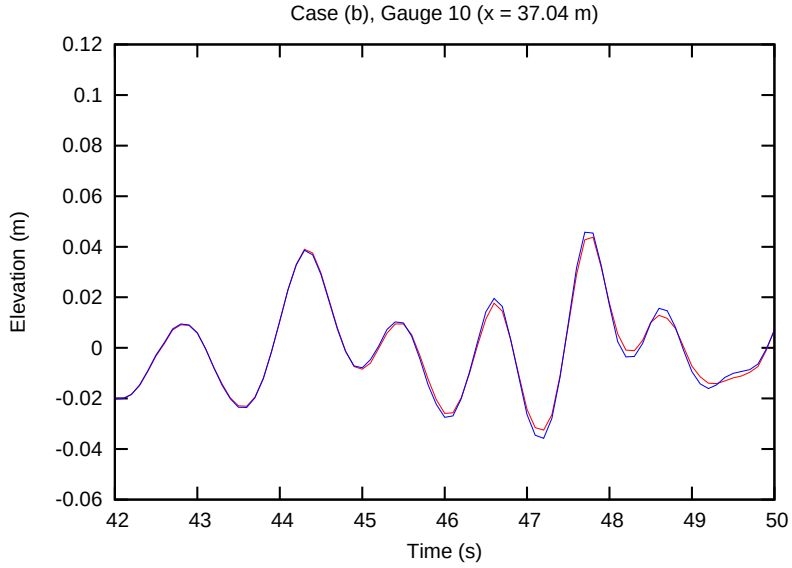


Figure 3.48: Graph showing modelled results with and without the momentum predictor step (blue and red lines respectively) at wave gauge 10 for case B.

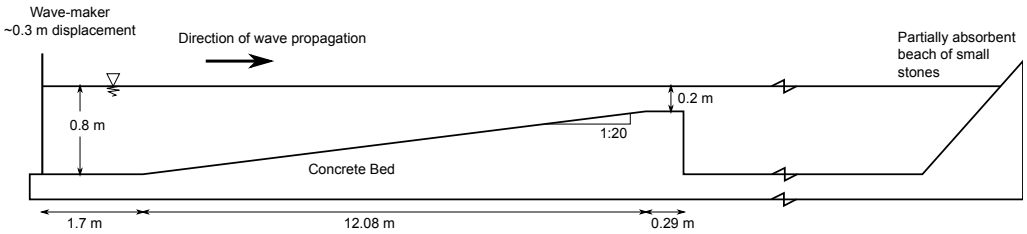


Figure 3.49: Cross-section schematic showing the geometry of the flat bed and sloping beach cases in the experiment.

## 3.4 DHI Test Case

### Description of case

This experiment was conducted in an 18 m wide test area constructed in the DHI shallow water wave basin with the addition of two, wooden guide walls. At one end of this area was a 36-segment, piston-type wave maker, while at the other end was a partially absorbing beach of coarse gravel.

The bed geometry was a sloping beach with a gradient of 1/20 in a water depth of 0.8 m. The beach terminated before emerging from the water, with the crest of the beach at a depth of 0.2 m before a vertical step in the bed. The bed geometry is shown in schematic form in figure 3.49. The wave tank was instrumented with 17 wave gauges along the centre line of the test area whose locations are shown in table 3.3. The full experiments are described in greater detail in Zang *et al.* (2010).

A large number of regular waves and focussed wave groups were tested as part of the experiments, of which 11 regular waves and one focussed group were used in these validation tests. The details of the regular waves are shown in table 3.4. The focussed wave group, designated "F14" in the experiments, used a JONSWAP wave spectrum scaled to fit a wave period of 1.22 s at the peak and have a total focussed amplitude (on a flat bed) of 0.14 m. It is therefore roughly comparable to the "R7" regular wave.

### Validation results

It is neither practical nor informative to show all the results from the twelve regular wave tests here, as the effects that can be seen substantially mirror those of the three "Dingemans" cases. Instead, only a se-

| No. | $x$ |
|---|---|
| 1 | 0.77 |
| 2 | 1.64 |
| 3 | 3.65 |
| 4 | 5.70 |
| 5 | 6.70 |
| 6 | 7.19 |
| 7 | 7.39 |
| 8 | 7.49 |
| 9 | 7.59 |
| 10 | 7.69 |
| 11 | 7.79 |
| 12 | 7.99 |
| 13 | 8.49 |
| 14 | 9.49 |
| 15 | 11.73 |
| 16 | 13.73 |
| 17 | 18.34 |

Table 3.3: Locations of wave gauges used in the DHI wave transformation test cases.

| Wave ID | Wave Period, $T$ (s) | Wave Length, $\lambda$ (m) | Wave Height, $H$ (m) | $kA$ |
|---|---|---|---|---|
| R1 | 0.82 | 1.05 | 0.02 | 0.05 |
| R2 | 0.82 | 1.05 | 0.03 | 0.10 |
| R3 | 0.82 | 1.05 | 0.07 | 0.20 |
| R4 | 0.82 | 1.05 | 0.10 | 0.30 |
| R5 | 1.22 | 2.27 | 0.04 | 0.05 |
| R6 | 1.22 | 2.27 | 0.07 | 0.10 |
| R7 | 1.22 | 2.27 | 0.14 | 0.20 |
| R8 | 1.22 | 2.27 | 0.22 | 0.30 |
| R9 | 1.63 | 3.65 | 0.06 | 0.05 |
| R10 | 1.63 | 3.65 | 0.12 | 0.10 |
| R12 | 1.63 | 3.65 | 0.35 | 0.30 |

Table 3.4: Wave properties used in the validation test cases.

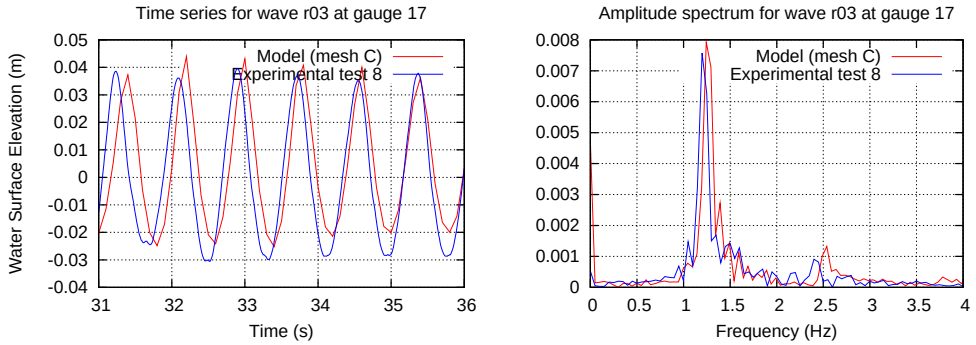


Figure 3.50: Modelled and experimental wave series and spectra from gauge 17 from wave R03.

lection of wave gauges exhibiting interesting wave behaviour are reproduced below.

These results are shown in figures 3.50–3.58. It can be seen that the model is capable of representing the transformation of the waves as they travel up the submerged beach and over the backward-facing step, but that the results for the longer waves are better than those for the shorter waves. This difference is related primarily to the quality of the mesh: models with more cells in a given wavelength perform better than those with fewer cells.

The incoming wave boundary also has a large effect on the accuracy of the model. It can be seen from the gauge 1 results that in some cases the amplitude of the incoming wave is not correctly reproduced near the boundary. In these cases, wave r07 for example, while the wave transformation processes proceed as expected, the amplitude is underestimated throughout. This suggests that, for the steeper waves, a more accurate, higher-order boundary condition should be used.

The results from the focussed wave group, exhibit some new behaviour. The figures show the wave surface elevations and spectra at four gauges: 1 (incident wave from the paddle), 9 (half way up the beach), 16 (the crest of the beach) and 17 (behind the beach). The surface elevation time series are shown in figures 3.59–3.62 and the corresponding wave spectra are shown in figure 3.63–3.66. It can be seen that the agreement between the modelled and experimental free-surface data is very good with two minor exceptions: the modelled time series does not quite reach the same low point in the troughs of the waves as the experimental data and the modelled data exhibits an overestimate at the start of the wave group.

Both of these discrepancies between the modelled and experimental

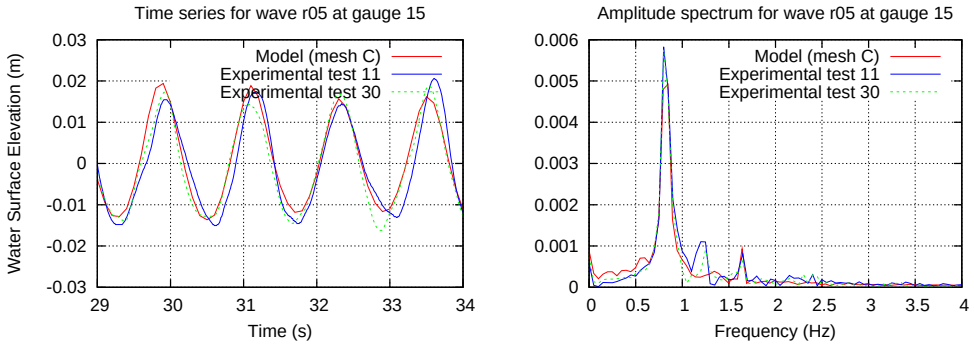


Figure 3.51: Modelled and experimental wave series and spectra from gauge 15 from wave R05.

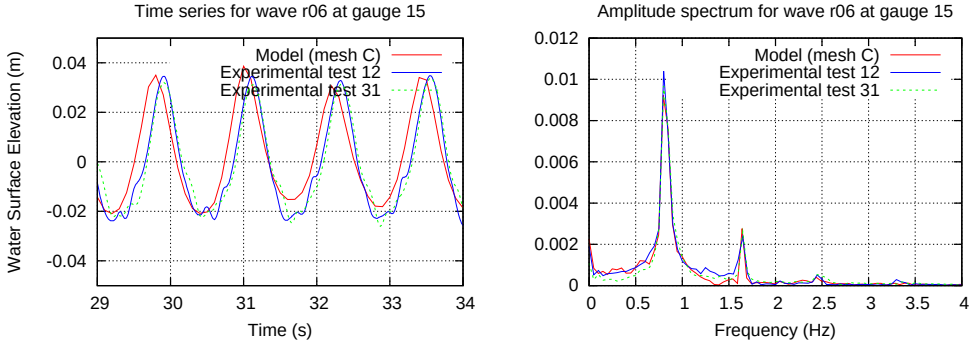


Figure 3.52: Modelled and experimental wave series and spectra from gauge 15 from wave R06.

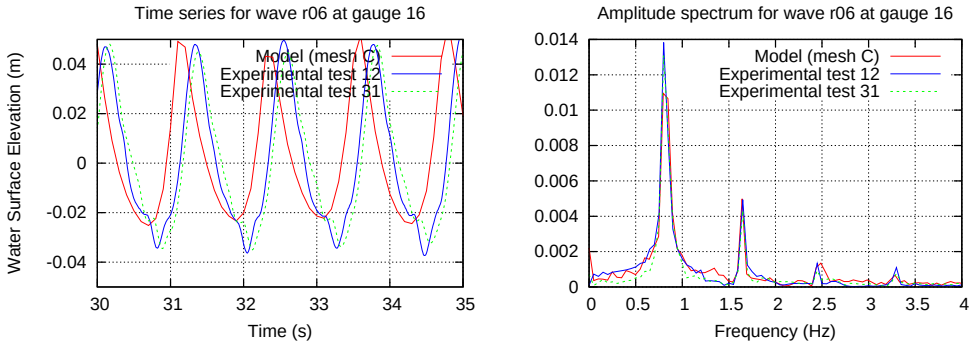


Figure 3.53: Modelled and experimental wave series and spectra from gauge 16 from wave R06.

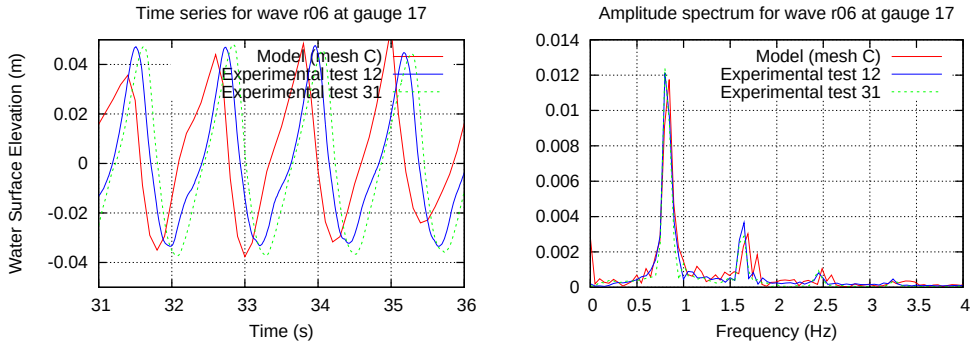


Figure 3.54: Modelled and experimental wave series and spectra from gauge 17 from wave R06.

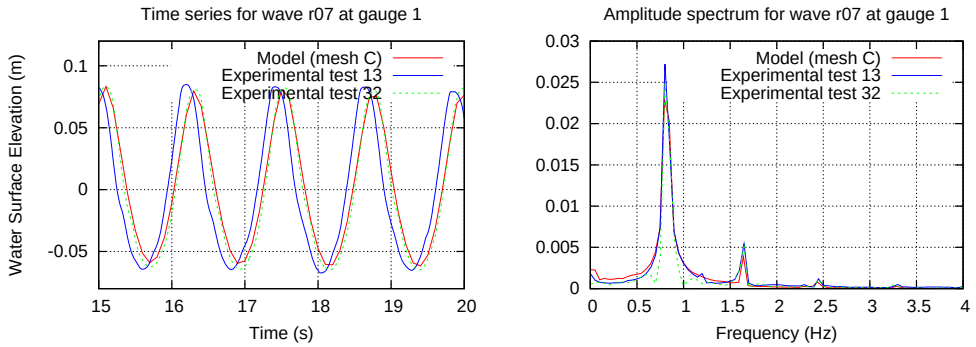


Figure 3.55: Modelled and experimental wave series and spectra from gauge 12 from wave R07.

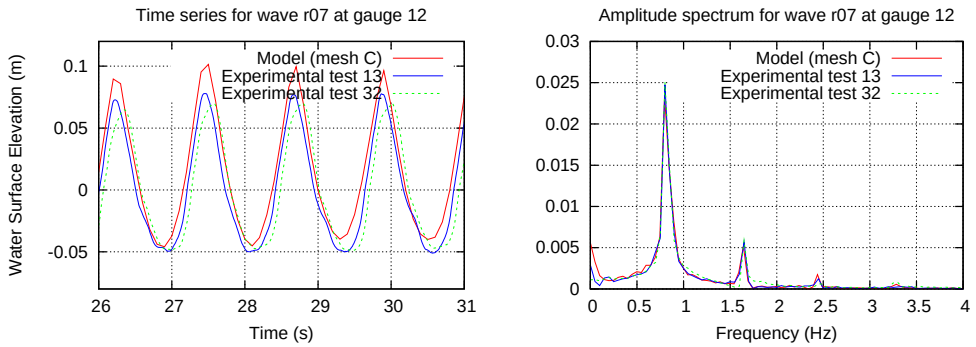


Figure 3.56: Modelled and experimental wave series and spectra from gauge 12 from wave R07.

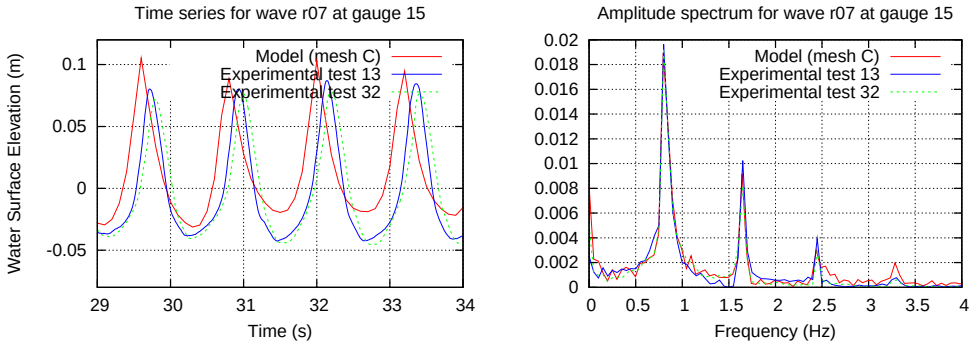


Figure 3.57: Modelled and experimental wave series and spectra from gauge 15 from wave R07.

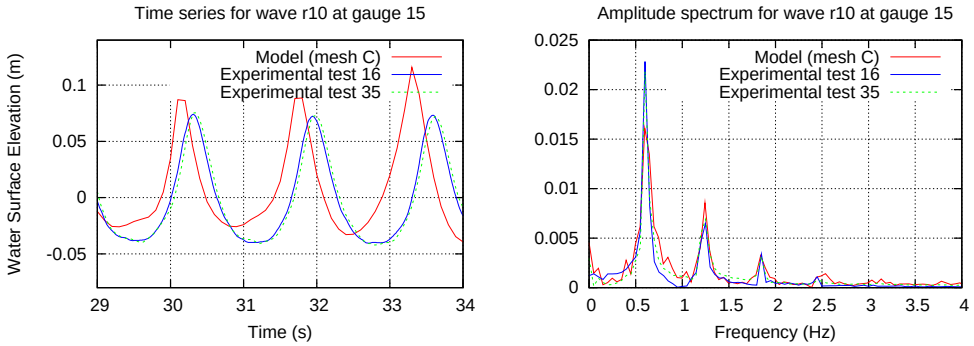


Figure 3.58: Modelled and experimental wave series and spectra from gauge 15 from wave R10.

data can be, to some extent, ascribed to the differences in the way the waves are generated between the model and the wave tank. In the wave tank the volume of water was constant and the waves were generated using a segmented, piston-type wave maker. This generates waves by applying a velocity to the water that is constant throughout the depth. In the model, however, the waves are generated by applying the Stokes equations for velocity under a wave, adding and removing water from the domain as necessary. This means that the model is subject to the phenomenon of Stokes' drift: more water is injected into the model domain at the crest of each wave than is removed at each trough, causing a gradual build-up of water within the domain. This can be seen most clearly in the results from gauge 17, where the modelled mean water level has clearly increased before the bulk of the wave group arrives at the gauge.

This Stokes' drift effect can be modelled as an additional long wave

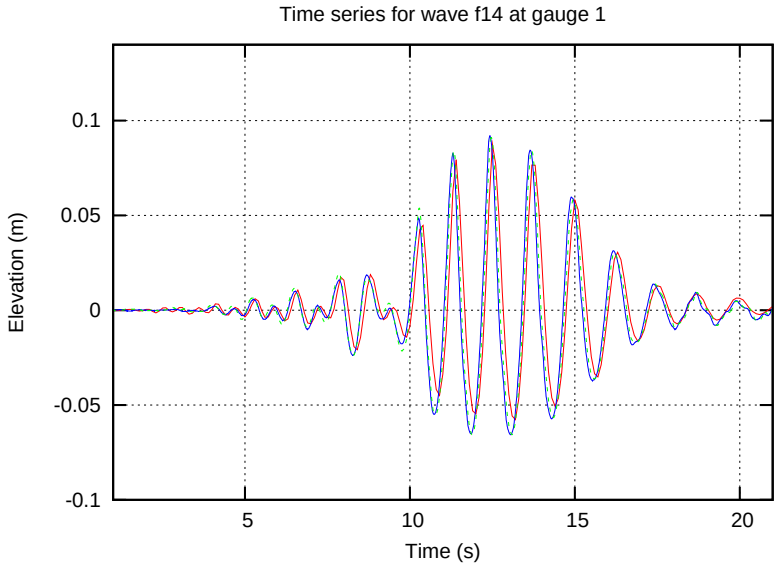


Figure 3.59: Graph showing the observed (blue and green lines) and modelled (red line) elevation time series at wave gauge 1 for case F14.

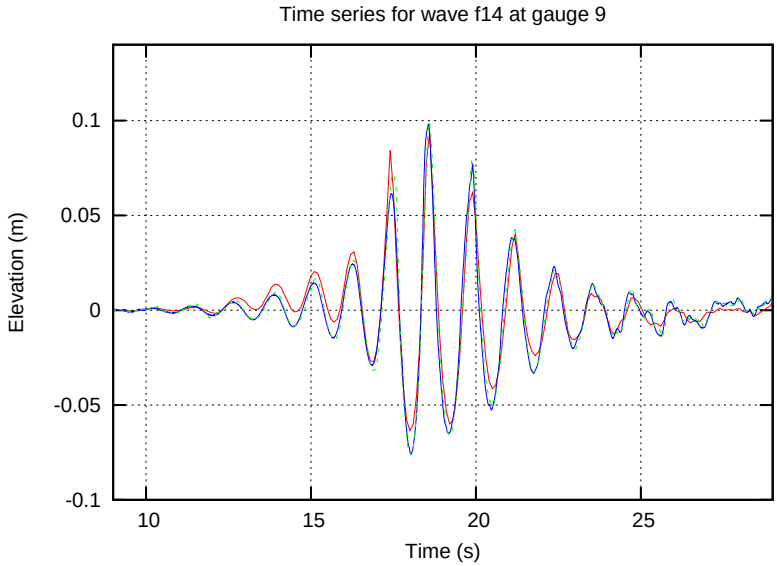


Figure 3.60: Graph showing the observed (blue and green lines) and modelled (red line) elevation time series at wave gauge 9 for case F14.

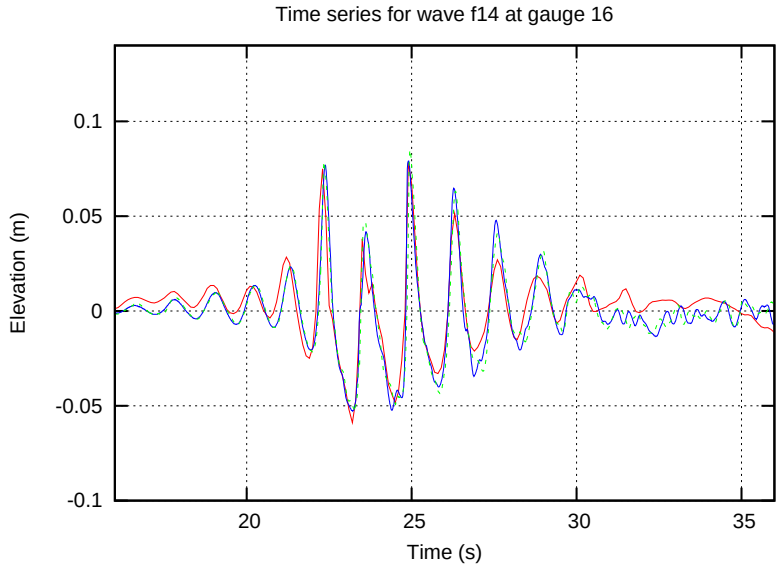


Figure 3.61: Graph showing the observed (blue and green lines) and modelled (red line) elevation time series at wave gauge 16 for case F14.

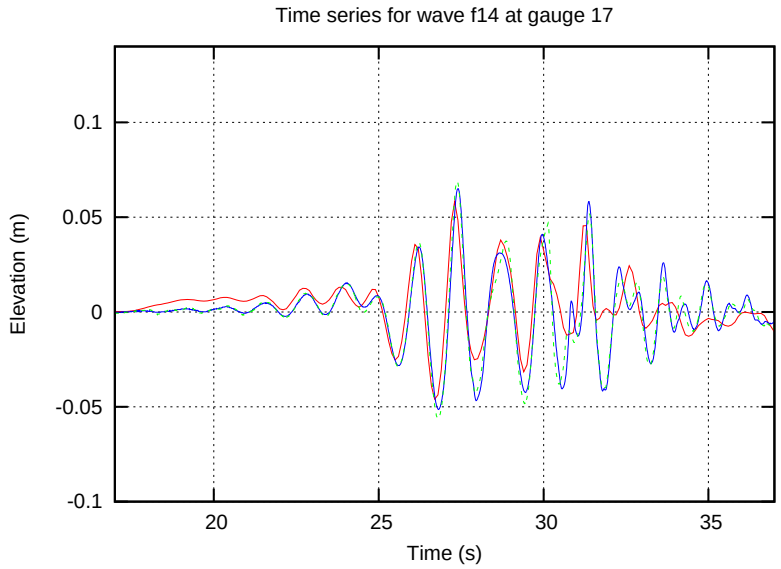


Figure 3.62: Graph showing the observed (blue and green lines) and modelled (red line) elevation time series at wave gauge 17 for case F14.

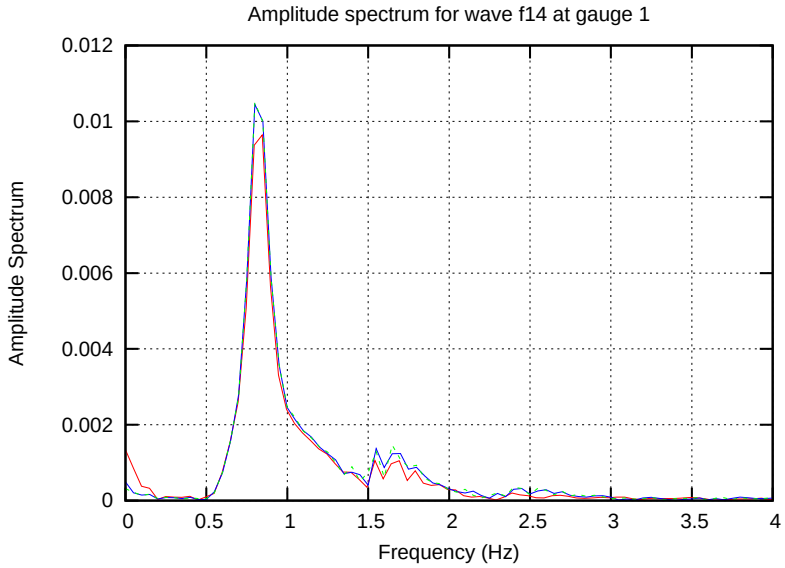


Figure 3.63: Graph showing the observed (blue and green lines) and modelled (red line) amplitude spectra at wave gauge 1 for case F14.

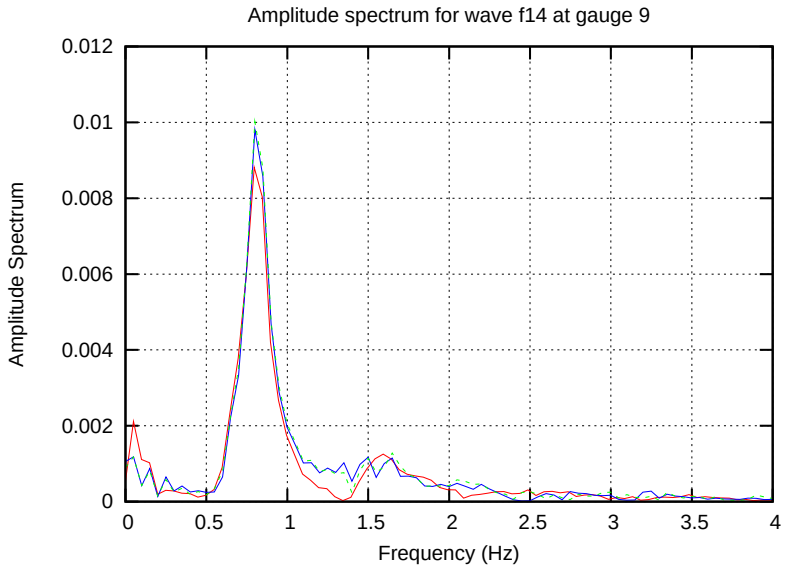


Figure 3.64: Graph showing the observed (blue and green lines) and modelled (red line) amplitude spectra at wave gauge 9 for case F14.

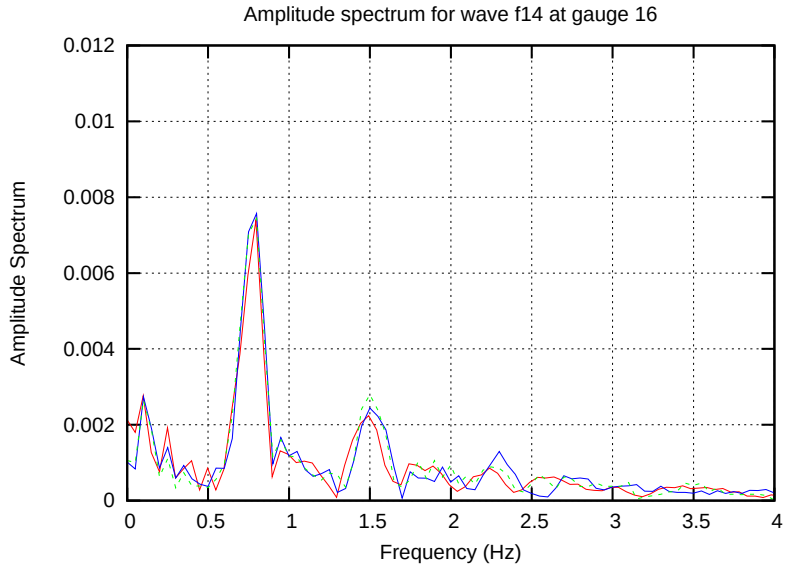


Figure 3.65: Graph showing the observed (blue and green lines) and modelled (red line) amplitude spectra at wave gauge 16 for case F14.

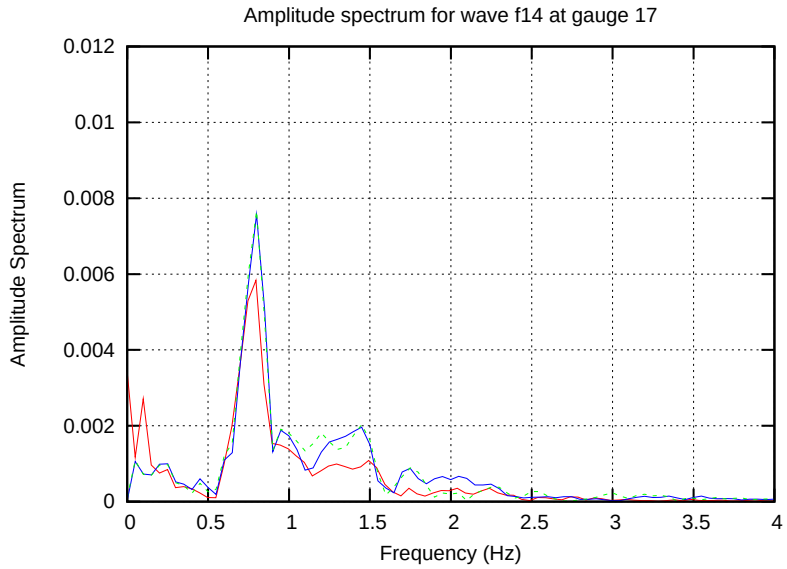


Figure 3.66: Graph showing the observed (blue and green lines) and modelled (red line) amplitude spectra at wave gauge 17 for case F14.

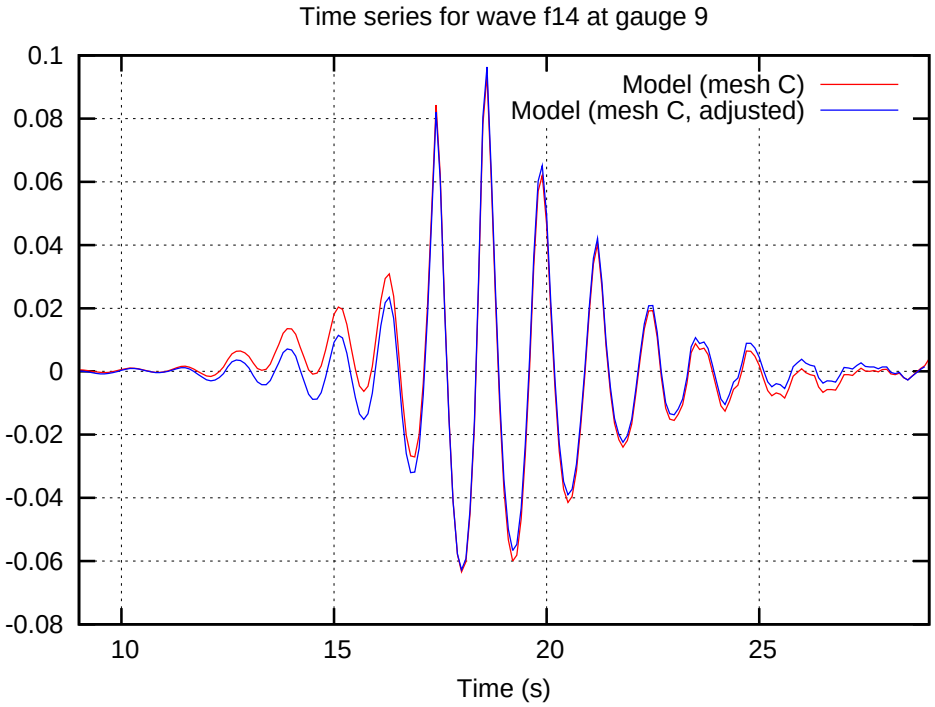


Figure 3.67: Graph showing the effect of the high-pass filter on the elevation time series at gauge 9.

component in the data. This long wave component can be seen in the wave spectra plots, where the model is shown to overestimate the very low frequencies. The model outputs can be corrected for this effect, however, by simply passing them through a high-pass filter to remove the wave components with frequencies of less than 0.25 Hz. The effect of this adjustment is shown in figure 3.67 and the comparison between the adjusted free surface and the experimental data is shown in figure 3.68–3.71. It is clear that this post-processing has improved the results, especially in the initial portion of the wave group and that the processing step has had a negligible effect on the peak levels.

As discussed in section 2.2, focussed wave groups can be used to decompose a wave spectrum into its first-, second-, and higher-order effects. This is done by comparing a wave group focussed to a crest and a wave group focussed to a trough. Full details of the method are given in Zang *et al.* (2006). This technique has been used in this case to further inspect the model's results and assess the model's performance.

Figures 3.72–3.75 show comparisons between the spectra of the mod-

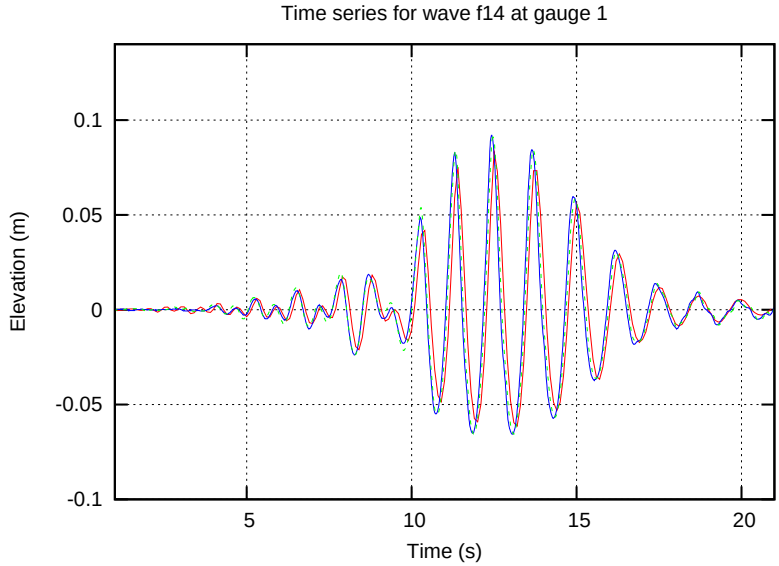


Figure 3.68: Graph showing the observed (blue and green lines) and modelled (red line) elevation time series adjusted for Stokes' drift at wave gauge 1 for case F14.

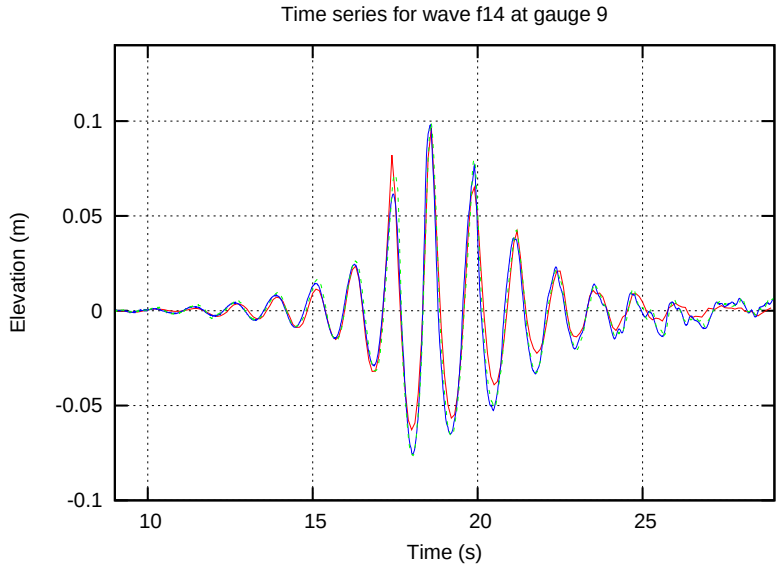


Figure 3.69: Graph showing the observed (blue and green lines) and modelled (red line) elevation time series adjusted for Stokes' drift at wave gauge 9 for case F14.

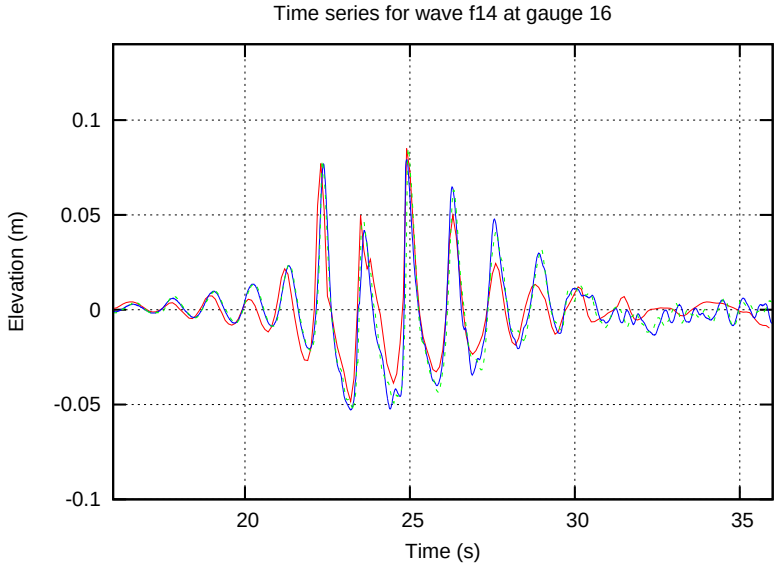


Figure 3.70: Graph showing the observed (blue and green lines) and modelled (red line) elevation time series adjusted for Stokes' drift at wave gauge 16 for case F14.

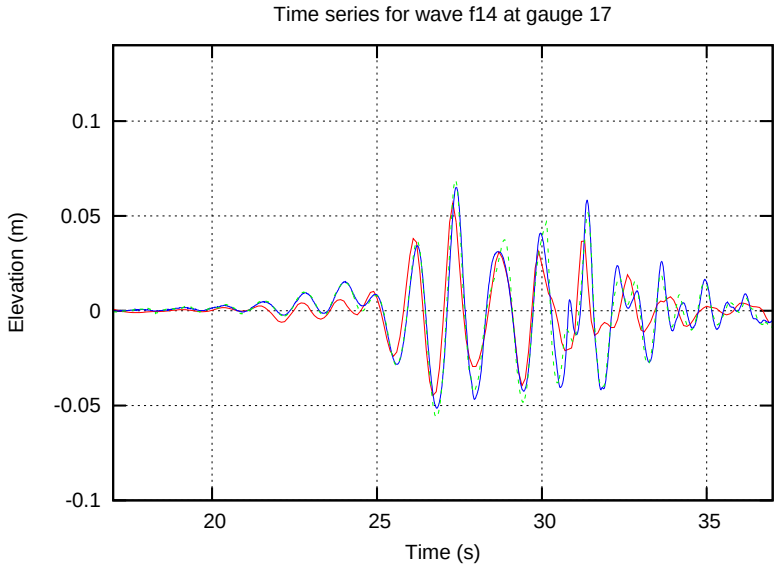


Figure 3.71: Graph showing the observed (blue and green lines) and modelled (red line) elevation time series adjusted for Stokes' drift at wave gauge 17 for case F14.

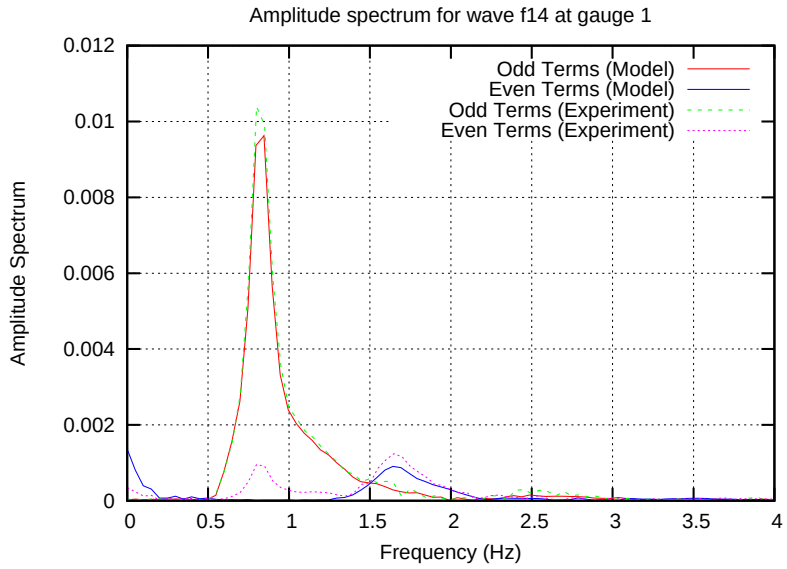


Figure 3.72: Graph showing the observed (blue and green lines) and modelled (red line) amplitude spectra at wave gauge 1 for case F14 decomposed into even- and odd-order terms.

elled and experimental data[1] in which the spectra have been decomposed into the odd- and even-order terms. It can be seen that the second-order effects (the peak at approximately 1.6 Hz) are well reproduced by the model and that it is the first-order effects (the peak at approximately 0.8 Hz) that are being underestimated. As already discussed, the model overestimates the second-order difference terms (the very low frequencies). The underestimate of the first-order terms by the model remains reasonably consistent throughout the length of the beach. These results continue to suggest that the main source of error in the model is the accuracy and schematisation of the boundary conditions and that the wave, once generated, is transmitted through the model with a reasonable degree of accuracy. The third and fourth order terms are generated when expected, in gauges 15 and 16. (Similar figures for all of the gauges are shown in the appendix).

[1]Only one experimental test has been shown here for the sake of clarity.

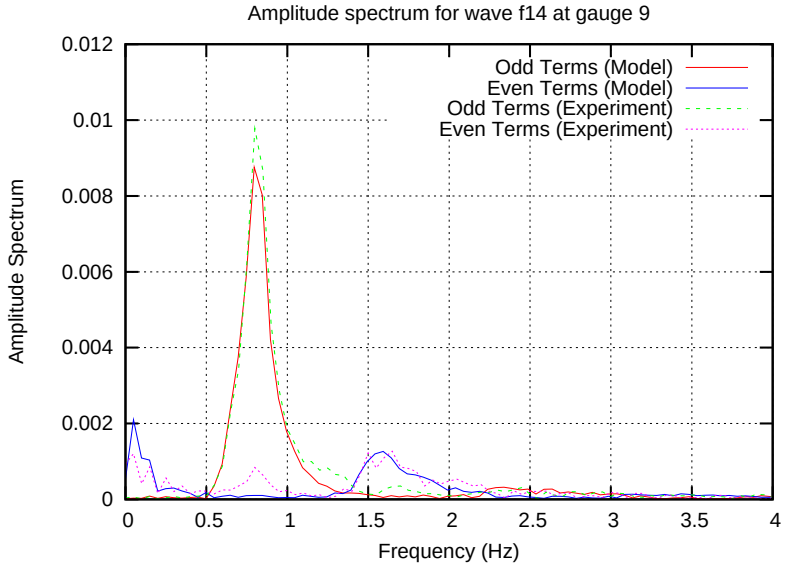


Figure 3.73: Graph showing the observed (blue and green lines) and modelled (red line) amplitude spectra at wave gauge 9 for case F14 decomposed into even- and odd-order terms.

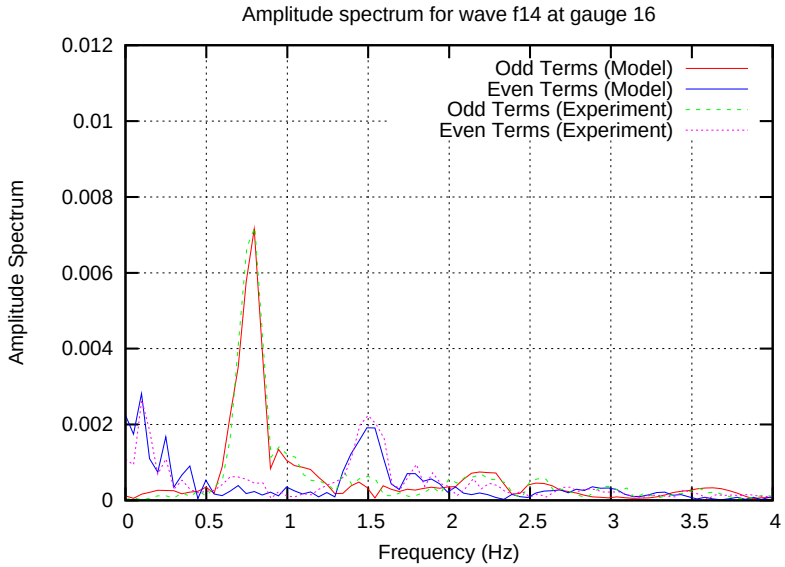


Figure 3.74: Graph showing the observed (blue and green lines) and modelled (red line) amplitude spectra at wave gauge 16 for case F14 decomposed into even- and odd-order terms.

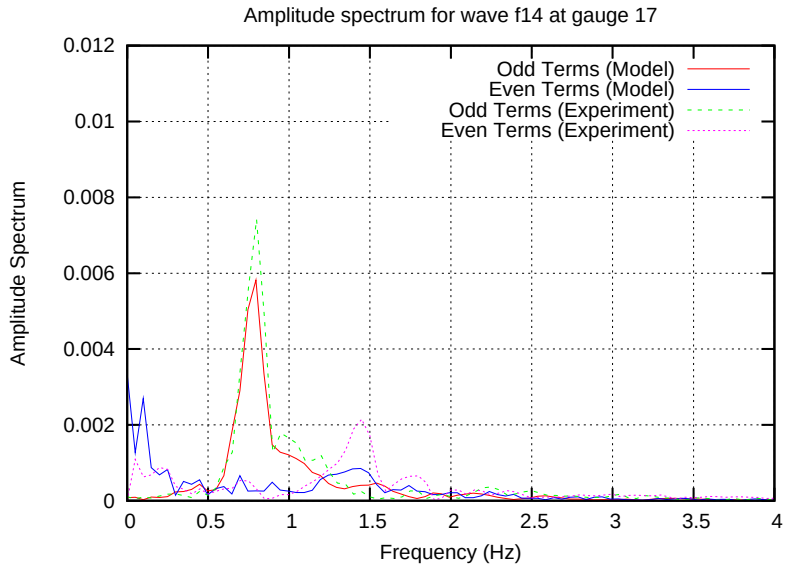


Figure 3.75: Graph showing the observed (blue and green lines) and modelled (red line) amplitude spectra at wave gauge 17 for case F14 decomposed into even- and odd-order terms.

| Wave Case | Mesh | | | |
|---|---|---|---|---|
| | A | B | C | D |
| (a) | $1.432 \times 10^{-3}$ | $1.768 \times 10^{-4}$ | $1.354 \times 10^{-4}$ | —.— |
| (b) | $6.149 \times 10^{-4}$ | $4.411 \times 10^{-5}$ | $6.054 \times 10^{-5}$ | $1.298 \times 10^{-5}$* |
| (c) | $7.430 \times 10^{-4}$* | $1.702 \times 10^{-4}$* | $1.183 \times 10^{-4}$ | —.— |

Table 3.5: Simulation run speeds (in modelled seconds per second of real time) on test system A (4 cores) for each wave case and mesh used in the "Dingemans" test case (values marked * have been scaled from a different number of processors).

## 3.5 Practicality

In order to assess the practicality of the models described above for use by practising civil engineers the run times of the models were calculated. These models were run on test system A, parallelised over one to four cores. Table 3.5 shows the run speed of the "Dingemans" test case runs on each of the meshes and for each of the wave cases.

These speeds correspond to run times of approximately 11 hours for

| GCC Optimisation flags | Run speed (s/s) |
|---|---|
| -O2 | $3.741 \times 10^{-4}$ |
| -O2 -march=core2 -mtune=core2 | $4.823 \times 10^{-4}$ |

Table 3.6: Effect of processor-specific compiler optimisations on the run speed of the "Dingemans" test case.

a minute of simulation on the coarsest mesh. While this means that simulations involving traditional irregular wave series of long duration are not currently practical using this modelling methodology, shorter runs involving regular wave series or focussed wave groups can be accomplished relatively quickly (as over-night simulations) on meshes of this size and density.

It can be seen that the run time increases significantly with mesh density because not only does the computer have to solve more equations but the timestep used in the runs also varies to maintain a constant Courant number, resulting in many more steps being required to cover the same time period. It can also be observed that the more non-linear and violent waves require longer run-times. This, again, is due to the dependency of the timestep on the Courant number.

It was found that, as part of this testing, that significant model speed increases could be achieved at the compilation stage. By default, OpenFOAM (and many other computational models) are configured so that the executables work on any (AMD64 instruction set–based) platform. It is possible, however, to configure OpenFOAM in such a way that the executables are specialised for the particular CPU on which they are to be run (e.g. Intel's "Core2" CPU or AMD's "Shanghai" Opteron CPU). This is generally not done for commercial codes or widely distributed executables as there is no way to know exactly what type of computer the end user has, but can be done with open source codes as the user is free to compile these themselves. Table 3.6 shows the effect of these compiler optimisation flags on the run speeds for a particular run of the "Dingemans" test case on test system A. This run was performed over only a single core in order to remove any effects from the parallelism.

It can be seen that, at the price of generating an executable that will only function on Core2-based processors, the speed of the model can be increased by nearly 30%.

The results from the DHI test case also permit an assessment of the effect on the run speed of the wave parameters. It is expected that larger,

| | kA = 0.05 | kA = 0.10 | kA = 0.20 | kA = 0.30 |
|---|---|---|---|---|
| $\lambda$ = 1.05 | $1.23 \times 10^{-3}$ | $1.12 \times 10^{-3}$ | $3.20 \times 10^{-4}$ | $3.24 \times 10^{-4}$ |
| $\lambda$ = 2.27 | $1.23 \times 10^{-3}$ | $5.82 \times 10^{-4}$ | $5.10 \times 10^{-5}$ | $2.27 \times 10^{-4}$ |
| $\lambda$ = 3.65 | $1.16 \times 10^{-3}$ | $3.19 \times 10^{-4}$ | — | $2.45 \times 10^{-4}$ |

Table 3.7: Run speeds in modelled seconds per second for otherwise identical models with different wave parameters on test system A (1 core).

more violent waves would take longer to simulate due to the increased velocities. The run speeds for the 11 regular waves tested are shown in table 3.7. From this table it can be seen that more violent waves (with greater kA) do take longer to simulate than less violent waves. It can also be seen that there is a (less significant) dependency on the wave length with longer waves taking slightly longer to simulate for an equivalent kA. It should be noted that this dependency is much weaker than that on the kA parameter itself—longer waves take slightly less time to simulate for an equivalent wave height.

It should also be noted that, in this study, the results for the longer, less violent waves were generally better than those for the shorter, steeper ones. Testing on various meshes has shown that shorter waves are better represented on finer meshes, which require longer run-times. It is also expected, from a review of the literature, that the simulation of the turbulence will have more effect in more violent waves and that the accuracy of the simulation would be improved by the introduction of a well calibrated turbulence model. Therefore, in order to obtain an equivalent level of accuracy, much longer run-times are required for more violent waves.

## 3.6 Conclusions

It has been shown that the interFoam model is capable of modelling the transmission and transformation of waves to a reasonable degree of accuracy. Waves can be generated using the approach described in section 2.7 and the model is capable of transmitting these waves for long distances (of more than 90 m) without significant numerical dissipation.

The model is capable of reproducing the "Dingemans" test to a reasonable degree of accuracy, although the computational expense required is likely to exceed that of Boussinesq-type models. It was found that the model was capable of generating the very high frequency wave harmon-

ics that the "Dingemans" test exhibits on top of the breakwater, but that these high frequency waves were subject to numerical dissipation on the meshes used, leading to slight inaccuracies in the model output downstream of the breakwater.

It has been shown that the model is convergent with respect to mesh size, with the accuracy of the modelled waves (as measured by the amplitudes of the modelled wave harmonics) increasing as mesh density increased. It has been shown that the modelled waves are not sensitive to several aspects of the solution scheme, including the use of the momentum predictor step and the use of a higher-order discretisation scheme.

The potential usefulness of the focussed wave group in CFD has been demonstrated, allowing the transmission and transformation of an entire spectrum of waves to be modelled in a very short time. It has been shown that the model is capable of simulating the transmission, transformation and focussing of a wave group to a reasonable degree of accuracy.

It is possible to use the same techniques described in section 2.7 to generate not only regular waves, but also focussed wave groups, although the technique suffers from the problem of Stokes' drift, which is not generally encountered to the same extent in wave flumes and tanks such as the one used at DHI. It may be useful to apply a correction to the wave boundary condition to counteract the effects of Stokes' drift, in the form of a gradual return flow under the wave. This has not been done as part of this work as the boundary condition as-is better represents the real behaviour of waves.

It has been shown that while it is not currently practical to model traditional irregular wave series of long duration due to the high computational cost, shorter simulations such as those involving regular waves and focussed wave groups can be accomplished in time periods short enough to use the model in a practical engineering application. Additionally, it has been demonstrated that the access to the model's source code conveys a significant advantage for the practising engineer as they are then able to take advantage of processor-specific compiler optimisations to produce models that run significantly faster.

# 4 WAVE INTERATION WITH COLUMNS

## 4.1 Validation Test

Chapter 3 has demonstrated that the model is capable of simulating the transmission and transformation of waves over a submerged structure, however another common wave/structure interaction problem is the simulation of wave interaction with surface-piercing structures.

In order to assess the model's performance in the interaction with a surface-piercing structure, another test case from the DHI experiments described in chapter 3 and Zang *et al.* (2010) was used. The model was used to recreate a series of tests performed in the same wave basin arrangement as the previous cases but with a surface-piercing cylinder incorporated and a different arrangement of wave gauges.

## 4.2 DHI Test Case

### Description of case

The basic geometry of the test is an 18 m wide test area built into a shallow basin by the addition of two wooden guide walls. At one end of this area was a 36-segment, directional, piston-type wave maker. A triangular mounting was installed in the centre of the flume. The resulting arrangement is shown in figure 4.1.

Two bed geometries were tested: a flat bed covered by a water depth of 0.505 m (shown in figure 4.2) and the submerged, sloping beach that has already been described in chapter 3 (shown in figure 4.3).

Tests were performed with and without a vertical cylinder of 0.25 m diameter suspended from the triangular mounting on both the flat bed and on the beach.

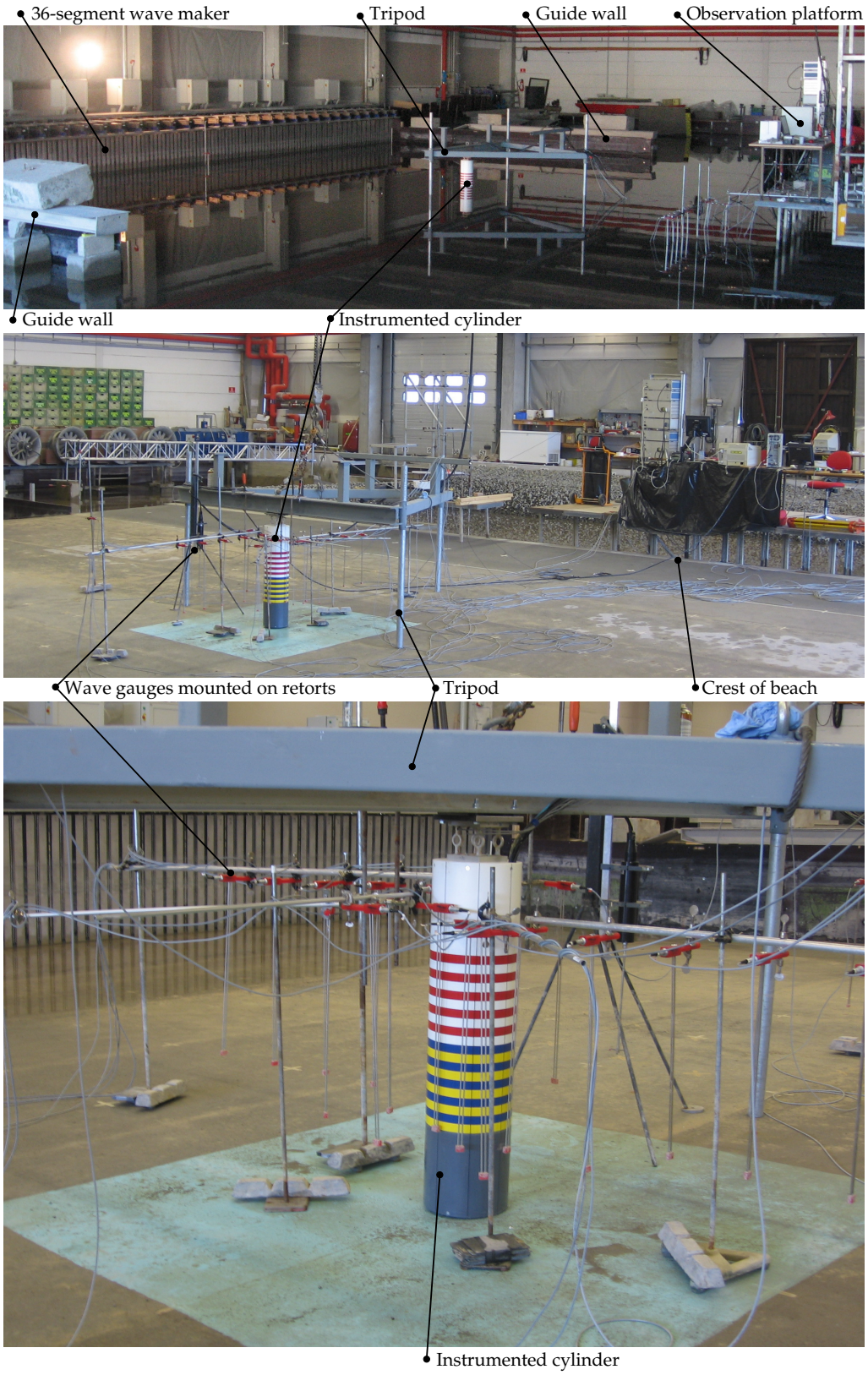


Figure 4.1: Figure with photographs of the experimental set-up.

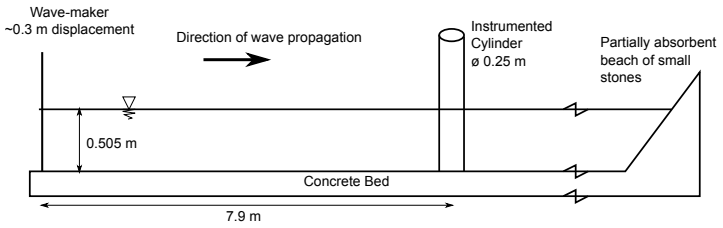


Figure 4.2: Cross-section schematic showing the key dimensions of the geometry of the flat bed cases, including the location of the structure.

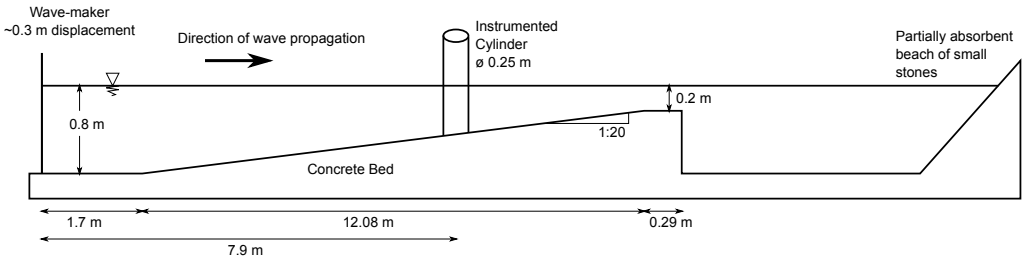


Figure 4.3: Cross-section schematic showing the key dimensions of the geometry of the submerged beach cases, including the location of the structure.

Results were recorded in the experiment using 19 wave gauges, which were positioned as shown in figure 4.4. A set of strain gauges were installed in the connection between the cylinder and the mounting and calibrated to record the total force on the cylinder. An accelerometer was installed at the top of the cylinder and four pressure gauges were installed on the front face at elevations of -0.1 m, 0 m, 0.05 m and 0.15 m relative to the mean water level. An ADV device was installed 7.75 m from the paddle to record velocities at 0.25 m depth in the free field. All of these devices were used with a sampling frequency of 1000 Hz.

In addition to these sensors, the tests were recorded using either one or two digital video cameras, allowing a visual verification of the sensor results.

The wave used in these tests was the same "F14" focussed wave group that was used in section 3.4.

It was intended to focus the wave groups just in front of the cylinder: i.e. a focus distance of 7.775 m, however due to wave transformation processes, especially on the submerged beach, this theoretical value was not always the most appropriate to achieve a large crest at the cylinder. The focal lengths of the wave groups were therefore adjusted with the

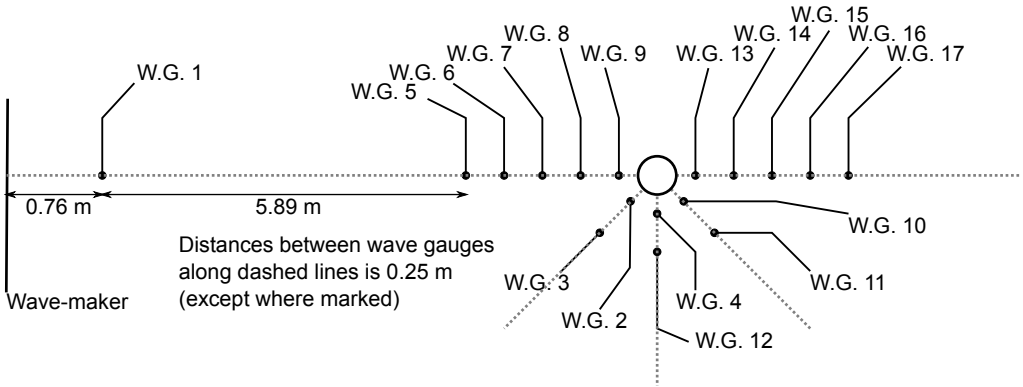


Figure 4.4: Diagram showing the locations of wave gauges 1–17 used in the DHI test cases. Wave gauge 18 was installed as a check on gauge 4, while gauge 19 was installed away from the cylinder as a check on gauge 9.

intention of producing the largest possible crest/trough from each group at the point just in front of the cylinder. This led to the focussed wave group having a different focal length to the theoretical value. The focal distances used for wave F14 were 7.7 m and 7.5 m on the beach and on the flat bed respectively.

In the experiment the tests were designed so that the focussed wave occurred 40 s after the paddle motion started. It was found that very little wave motion occurred in the first 20 s of this period and consequently, in order to reduce the computational expense of the model, the wave was set to focus after only 20 s in the model runs. Other aspects of the wave generation (such as the spectrum and the focal length) were unchanged between the model and experiment.

While the cases described in chapter 3 were two-dimensional in nature, and could be modelled in a two-dimensional vertical plane, this case requires three dimensions. A three metre section from the centre of the test area was modelled rather than the full 18 m in order to reduce computational cost. This value was based on visual observations from the experiment where reflected waves appeared to dissipate within the triangular mounting frame. Some preliminary tests were performed to ensure that no wave reflection was apparent from the side walls of the flume. The symmetry of the problem was used to reduce this further to a 1.5 m wide domain. The base mesh had cells of 0.0121 m $\times$ 0.05 m $\times$ 0.0133 m from which was cut the beach shape with no additional refinement. The cylinder was cut from the domain with two levels of ad-

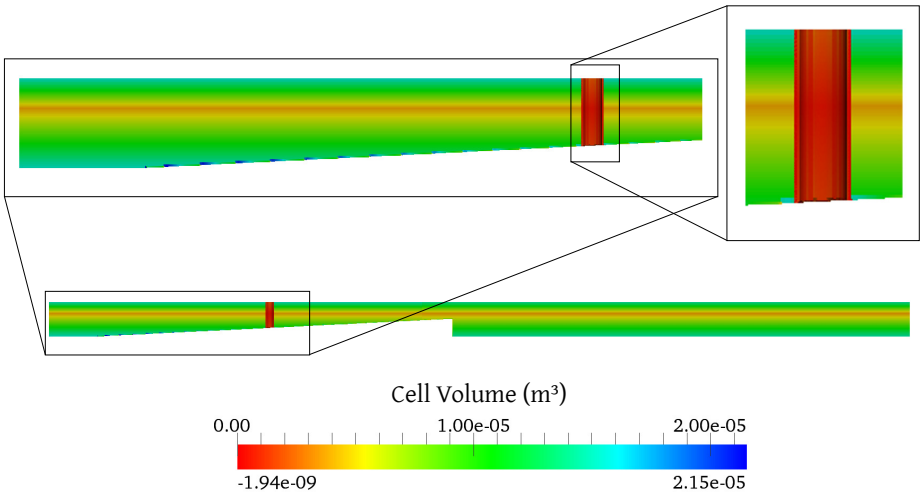


Figure 4.5: Mesh used in the wave interaction simulations with cells coloured according to cell volume.

ditional refinement on its surface. In the model the cylinder extended through the full height of the domain—potential for splashing onto the top of the cylinder was not modelled. Similarly, the mounting tripod was not modelled. The resulting mesh is shown in figure 4.5.

## Validation Results

### Water surface elevation

Figures 4.6 to 4.17 show a selection of the model results with the beach (the full results are given in appendix B). It can be seen that the model produces good agreement with the experimental results, despite the potential problems with Stokes' drift discussed above. No correction has been applied to these results as it can be seen from the wave spectra that many of the wave gauges in the vicinity of the cylinder exhibit low frequency waves which would not be preserved by the simple filtering process used in section 3.4.

The results from the initial gauges, 1–3 and 5–6 are relatively consistent. It can be seen from the spectra that the first order waves dominate the results and that the cylinder has relatively little effect, with the model only slightly underestimating the first order peak. This is borne out by

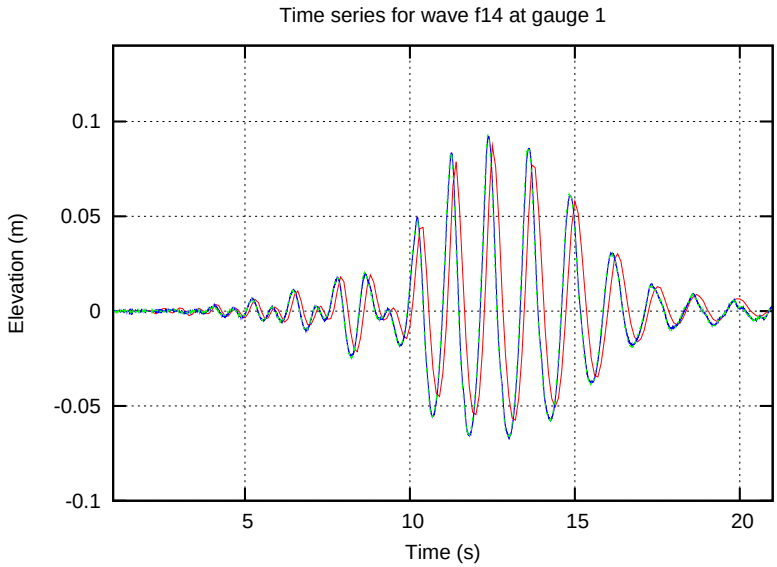


Figure 4.6: Graph showing the observed (blue and green lines) and modelled (red line) elevation time series at wave gauge 1 for case F14 with the beach and cylinder.

the time series which exhibit a good correspondence between the modelled and observed wave forms with the model slightly underestimating the wave peaks. As the wave travels further up the beach and around the cylinder wave transformation occurs, producing a clear third order peak in gauges 10 and 11 and a fourth order peak is visible in the spectra in gauges 13 and 14. In the time series a good correspondence between modelled and observed results is achieved at nearly all of the gauges. Only gauges 13 and 14 where the wave is breaking at the back of the cylinder does an underestimate occur. This underestimate is likely to be due to insufficient mesh quality at the back of the cylinder where the cylinder meets the symmetry plane.

Figure 4.18 shows a series of snapshots of the modelled water surface along the centre of the basin at 0.2 s intervals (with time progressing down the page). The two vertical lines represent the front and back face of the cylinder and the water surface shown between these two lines is the water surface around the surface of the cylinder. It can be seen that the wave breaks a short way in front of the cylinder and the travelling breaking wave slams into the front of the cylinder causing air entrainment as the water is deflected around the sides. It is not possible to accurately model this type of violent wave action in this level of detail except

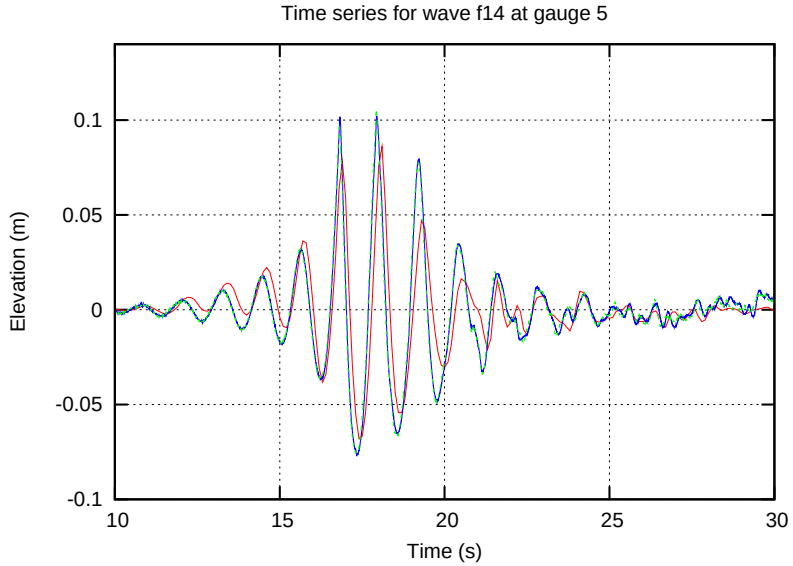


Figure 4.7: Graph showing the observed (blue and green lines) and modelled (red line) elevation time series at wave gauge 5 for case F14 with the beach and cylinder.

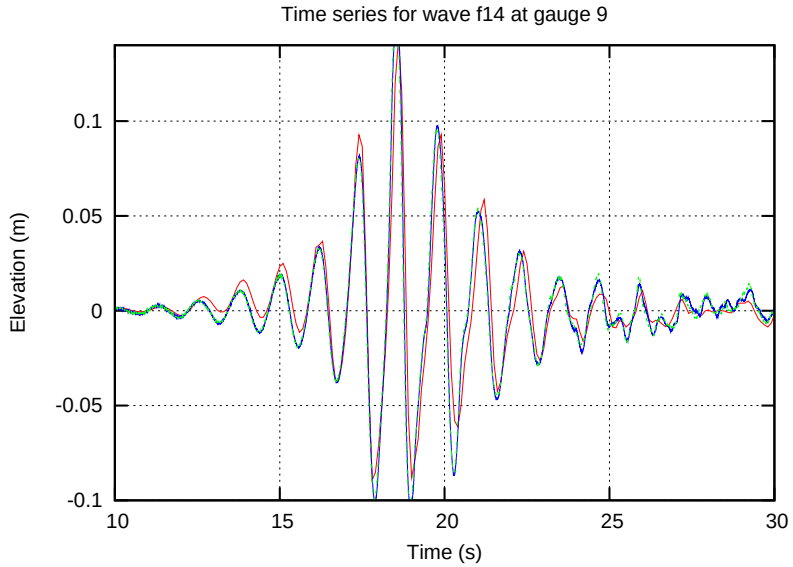


Figure 4.8: Graph showing the observed (blue and green lines) and modelled (red line) elevation time series at wave gauge 9 for case F14 with the beach and cylinder.

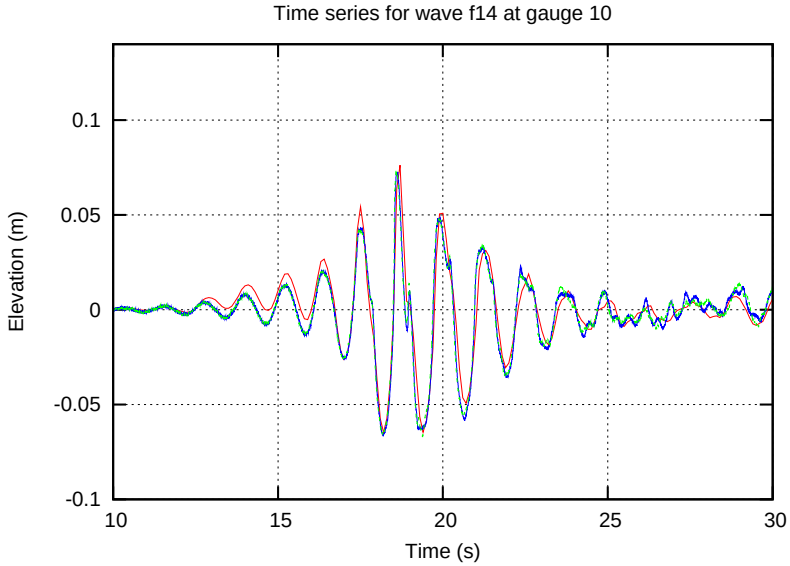


Figure 4.9: Graph showing the observed (blue and green lines) and modelled (red line) elevation time series at wave gauge 10 for case F14 with the beach and cylinder.

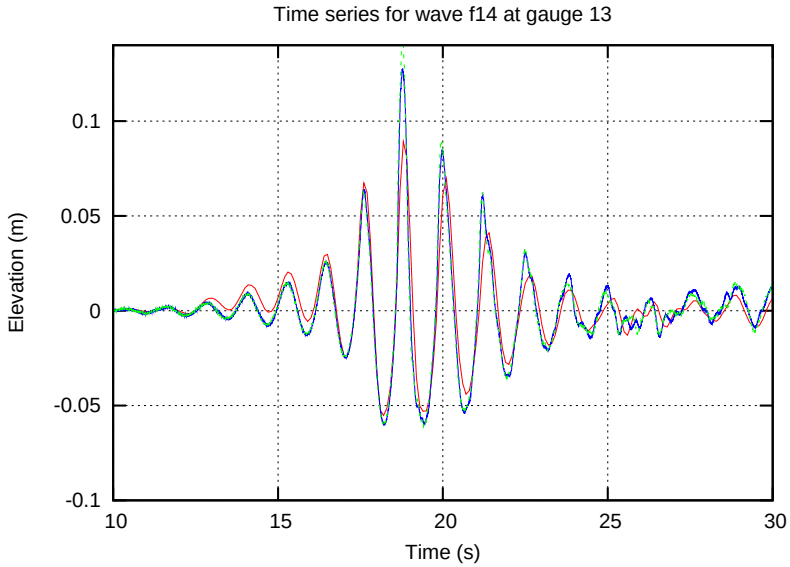


Figure 4.10: Graph showing the observed (blue and green lines) and modelled (red line) elevation time series at wave gauge 13 for case F14 with the beach and cylinder.

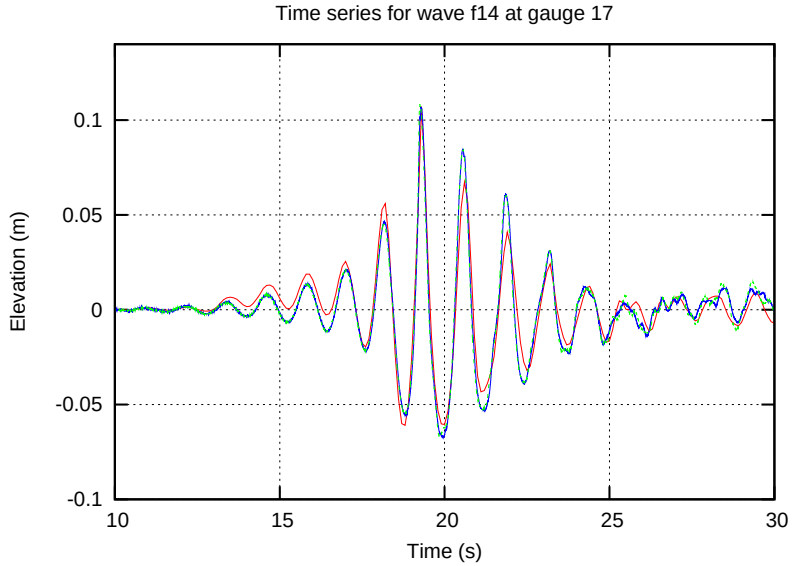


Figure 4.11: Graph showing the observed (blue and green lines) and modelled (red line) elevation time series at wave gauge 17 for case F14 with the beach and cylinder.

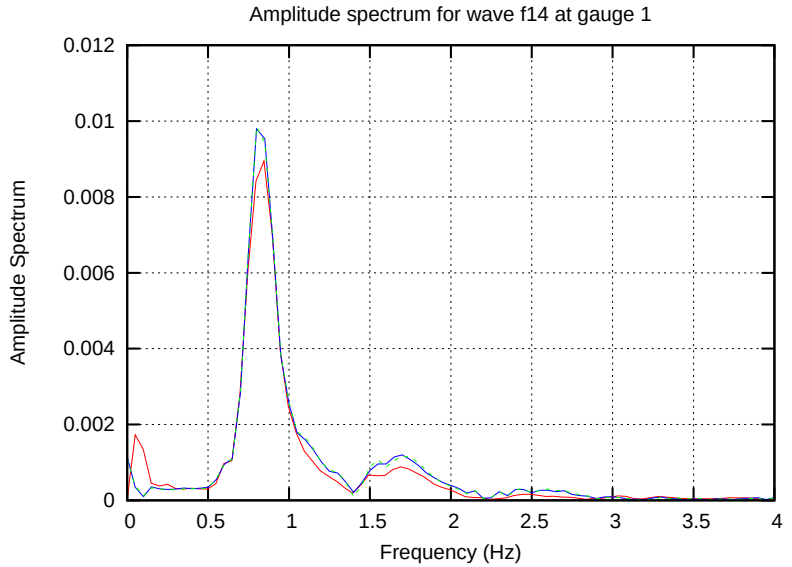


Figure 4.12: Graph showing the observed (blue and green lines) and modelled (red line) amplitude spectra at wave gauge 1 for case F14 with the beach and cylinder.

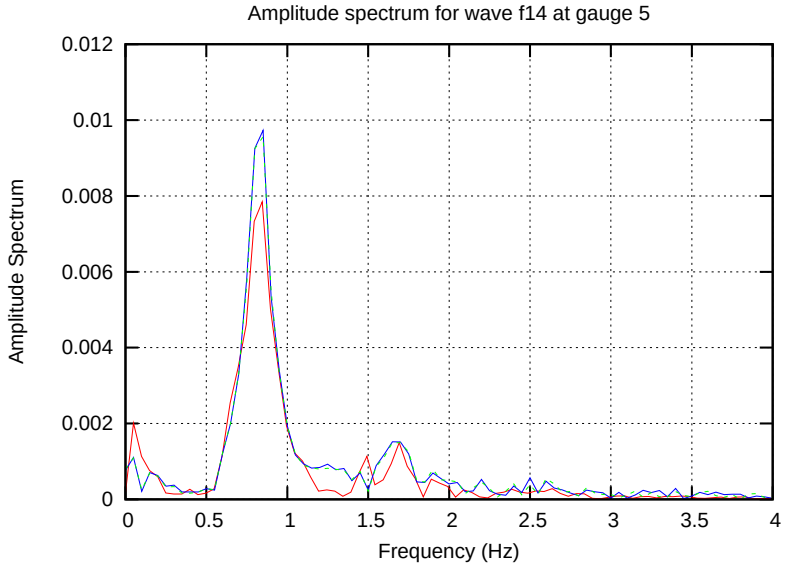


Figure 4.13: Graph showing the observed (blue and green lines) and modelled (red line) amplitude spectra at wave gauge 5 for case F14 with the beach and cylinder.

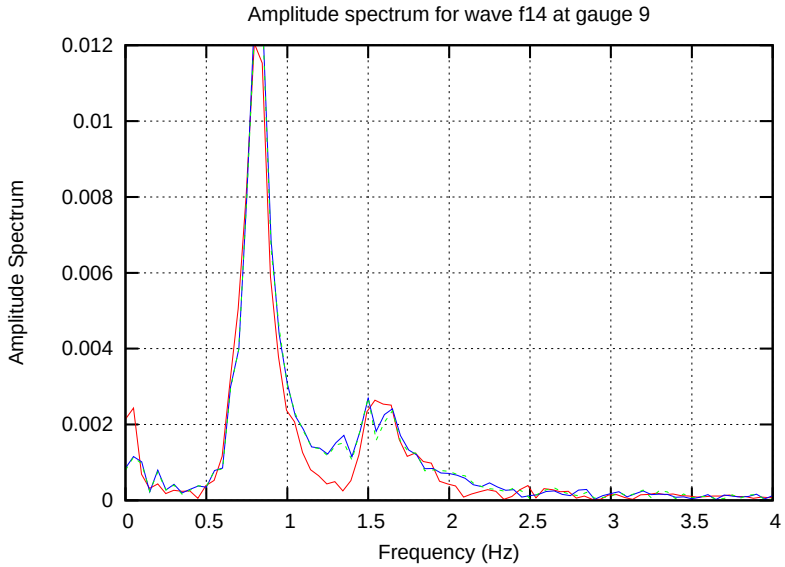


Figure 4.14: Graph showing the observed (blue and green lines) and modelled (red line) amplitude spectra at wave gauge 9 for case F14 with the beach and cylinder.

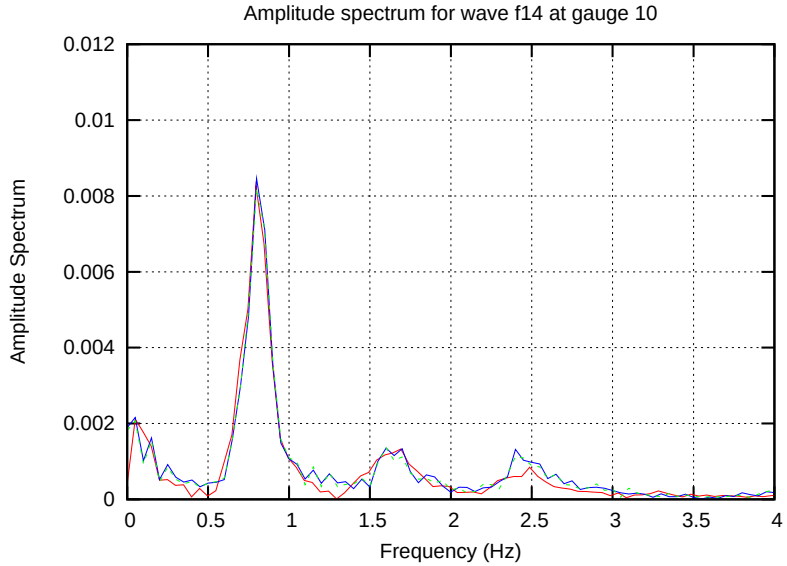


Figure 4.15: Graph showing the observed (blue and green lines) and modelled (red line) amplitude spectra at wave gauge 10 for case F14 with the beach and cylinder.

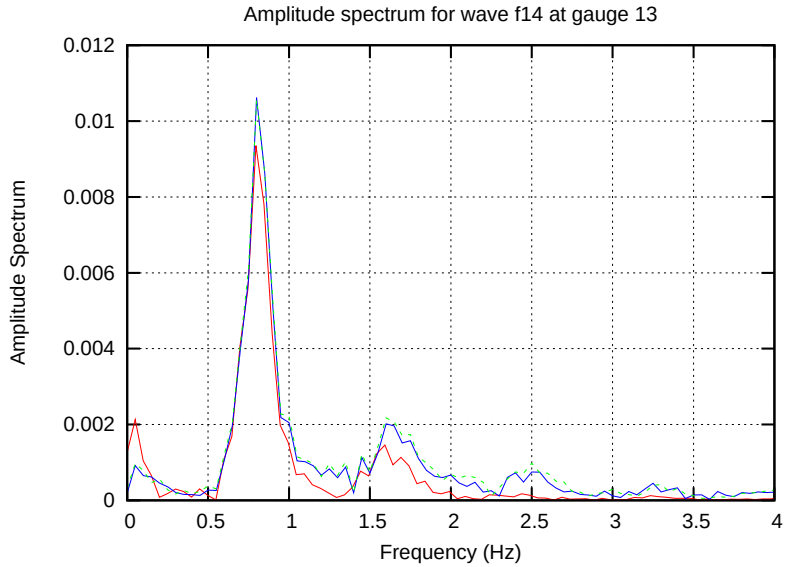


Figure 4.16: Graph showing the observed (blue and green lines) and modelled (red line) amplitude spectra at wave gauge 13 for case F14 with the beach and cylinder.

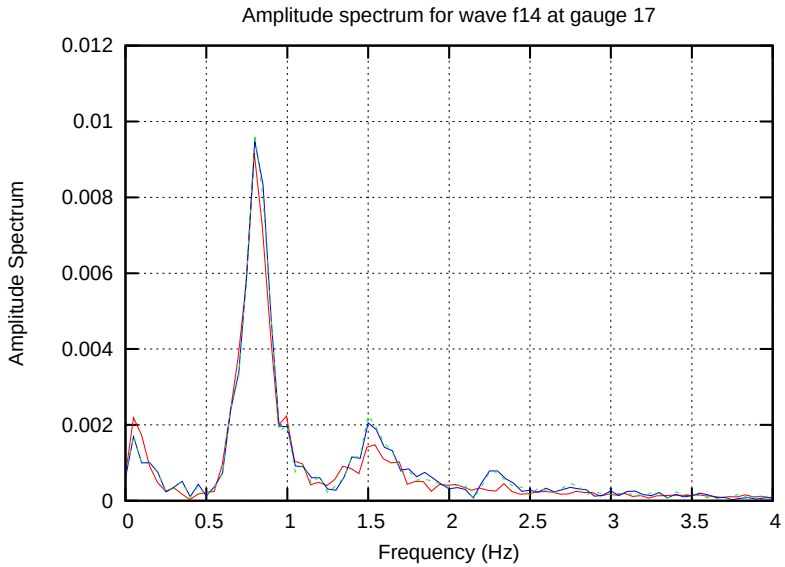


Figure 4.17: Graph showing the observed (blue and green lines) and modelled (red line) amplitude spectra at wave gauge 17 for case F14 with the beach and cylinder.

by using a CFD code.

Figures 4.19 to 4.30 similarly show the results of the model without the beach. As before, it can be seen that a good agreement is achieved between the model and the experimental data.

Here, without the beach, with a slightly different focal distance, and with shallower water, a very violent, nearly breaking wave is generated on the approach to the cylinder and can be seen in the time series results for gauges 5 and 6. As before, at gauges 13 and 14 with the beach, the height of this near-breaking wave is underestimated compared to the result recorded by the wave gauges. Outside of these early gauges, however, the results indicate that the model is reproducing the wave transformation processes around the cylinder very accurately. Unlike the results with the beach, only very small third and fourth order peaks are observed in the spectrum data.

Figure 4.31 shows a series of snapshots of the water surface along the centre of the basin as before. It can be seen that, as with the wave on the beach, the wave breaks a short way in front of the cylinder but that the action is much less violent than the same wave applied on the sloping beach. The interaction with the cylinder is more gentle with the water running up the front face of the cylinder rather than slamming into it.

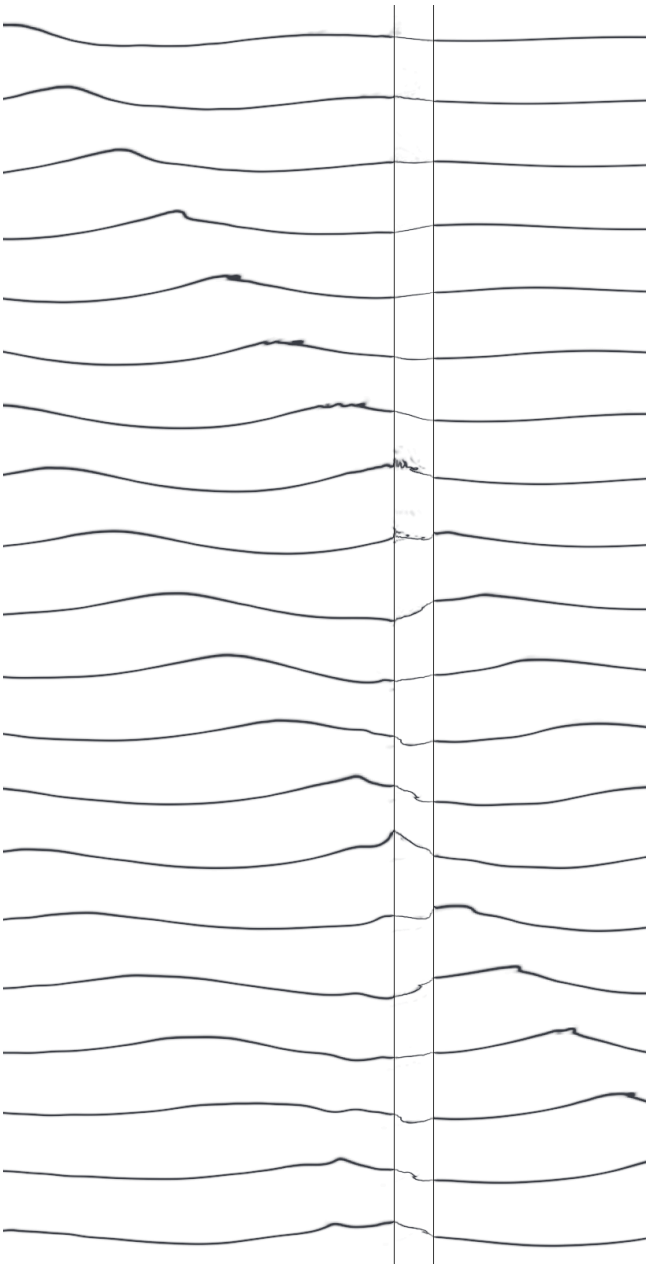

Figure 4.18: Snapshots of the water surface elevation of wave F14 with the cylinder at 0.2 s intervals.

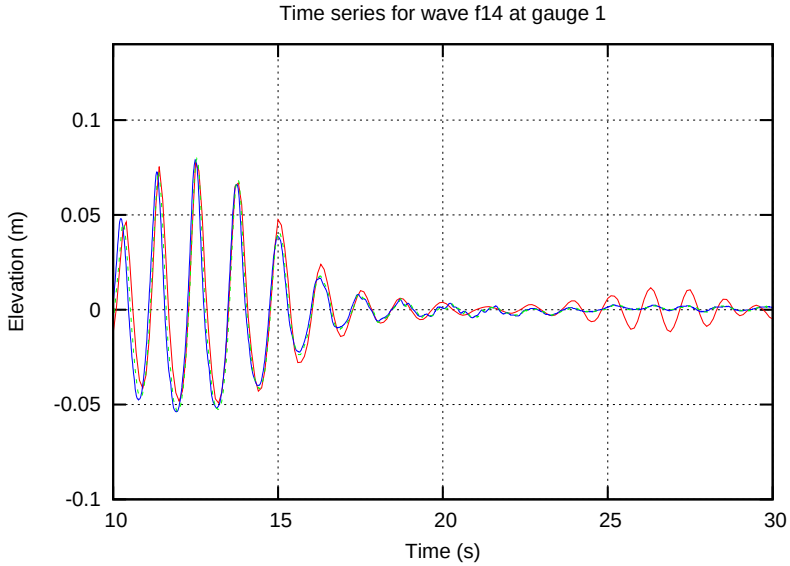


Figure 4.19: Graph showing the observed (blue and green lines) and modelled (red line) elevation time series at wave gauge 1 for case F14 with the beach and cylinder.

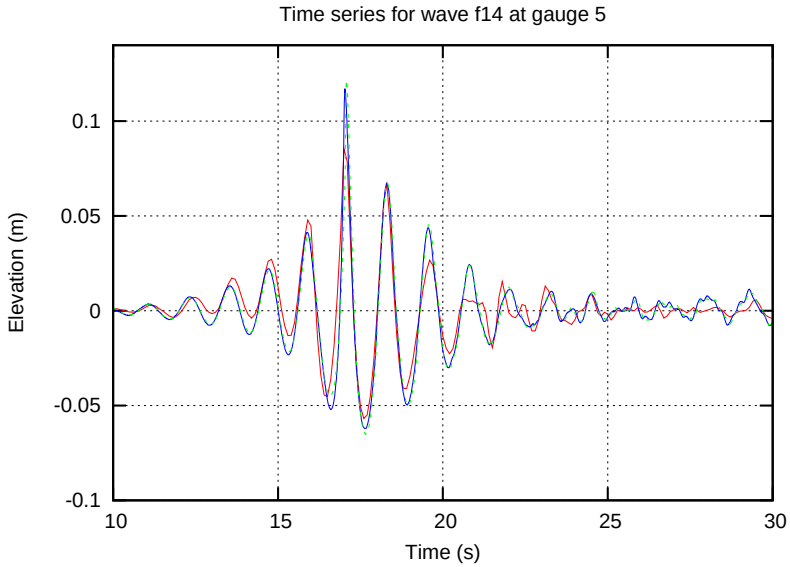


Figure 4.20: Graph showing the observed (blue and green lines) and modelled (red line) elevation time series at wave gauge 5 for case F14 with the beach and cylinder.

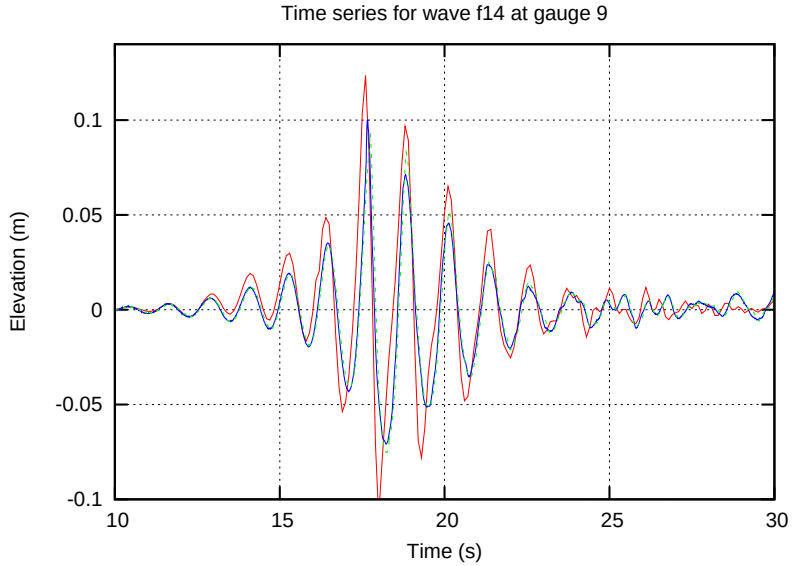


Figure 4.21: Graph showing the observed (blue and green lines) and modelled (red line) elevation time series at wave gauge 9 for case F14 with the beach and cylinder.

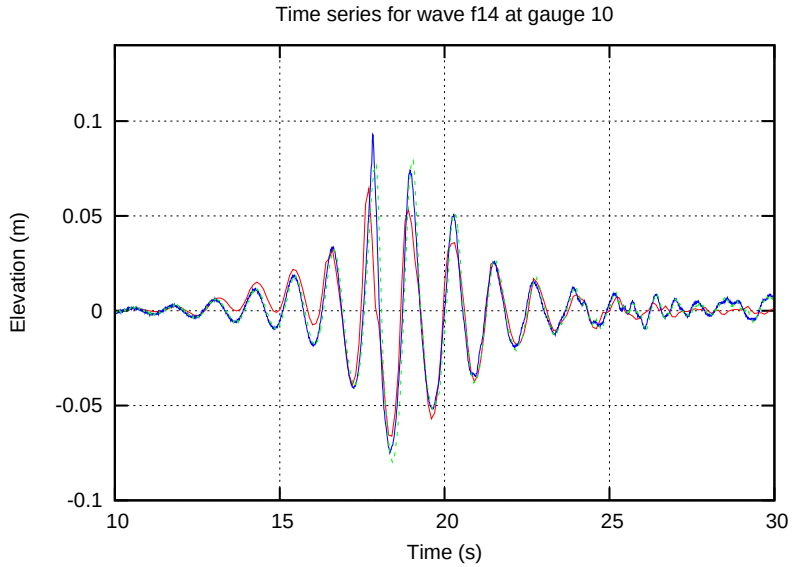


Figure 4.22: Graph showing the observed (blue and green lines) and modelled (red line) elevation time series at wave gauge 10 for case F14 with the beach and cylinder.

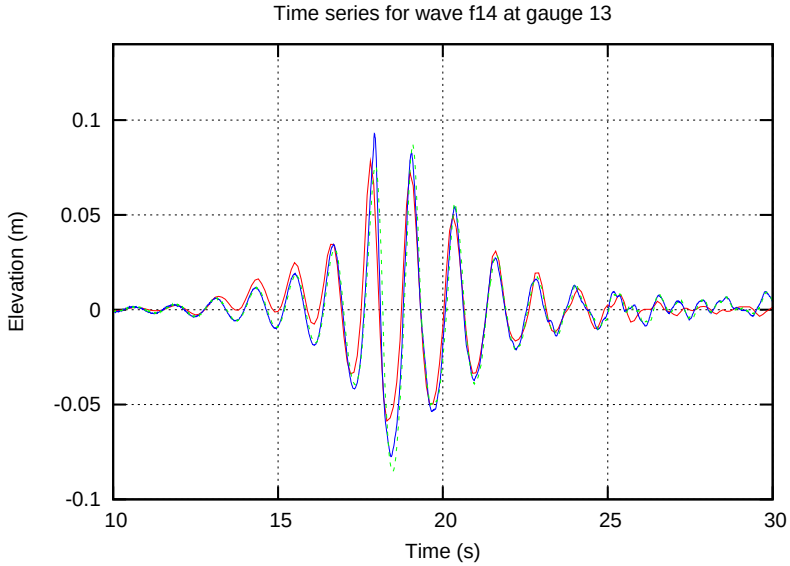


Figure 4.23: Graph showing the observed (blue and green lines) and modelled (red line) elevation time series at wave gauge 13 for case F14 with the beach and cylinder.

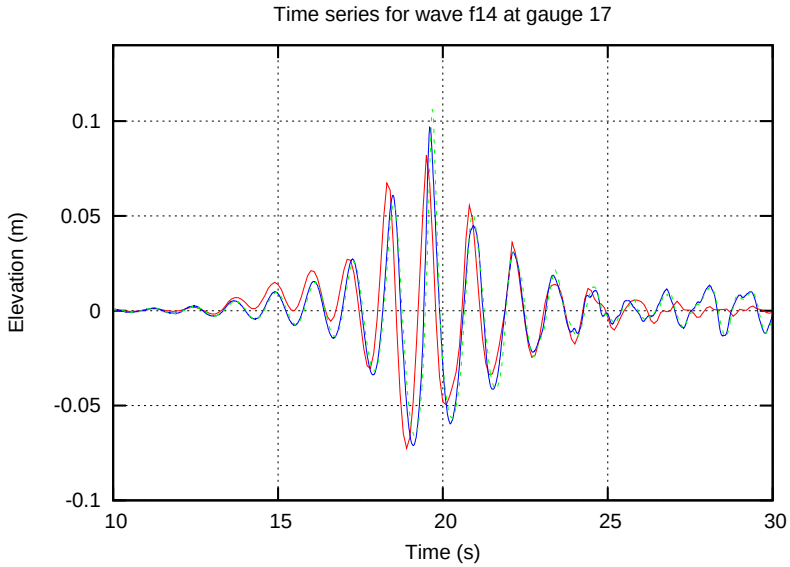


Figure 4.24: Graph showing the observed (blue and green lines) and modelled (red line) elevation time series at wave gauge 17 for case F14 with the beach and cylinder.

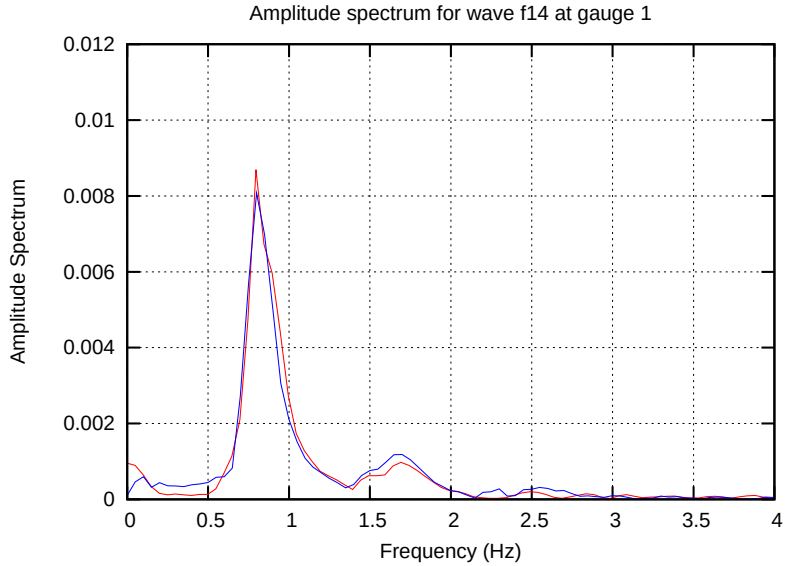


Figure 4.25: Graph showing the observed (blue and green lines) and modelled (red line) amplitude spectra at wave gauge 1 for case F14 with the beach and cylinder.

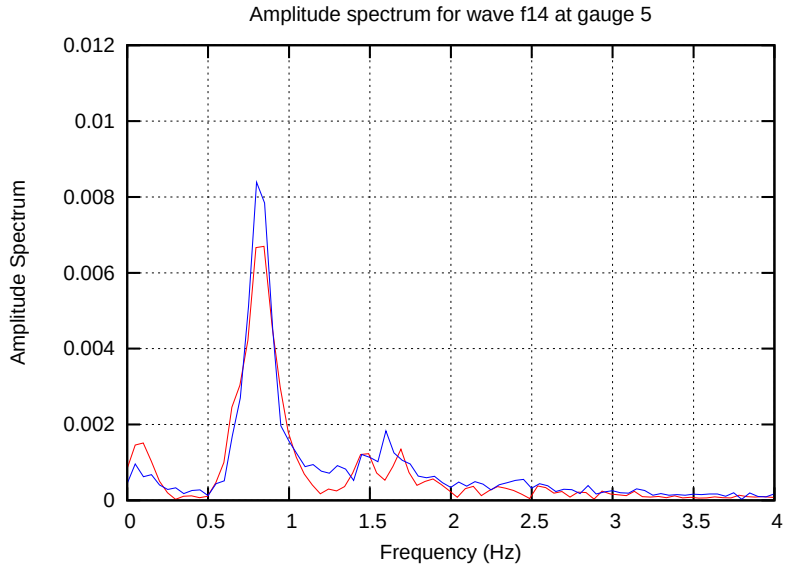


Figure 4.26: Graph showing the observed (blue and green lines) and modelled (red line) amplitude spectra at wave gauge 5 for case F14 with the beach and cylinder.

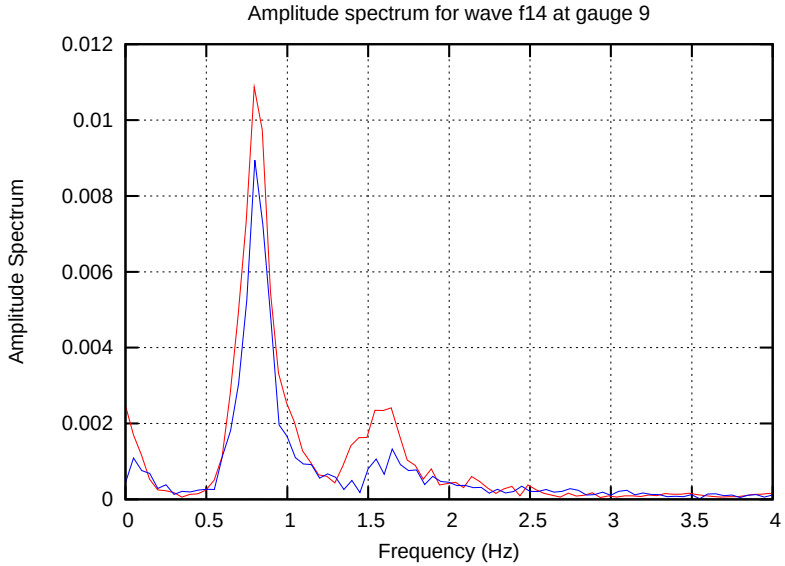


Figure 4.27: Graph showing the observed (blue and green lines) and modelled (red line) amplitude spectra at wave gauge 9 for case F14 with the beach and cylinder.

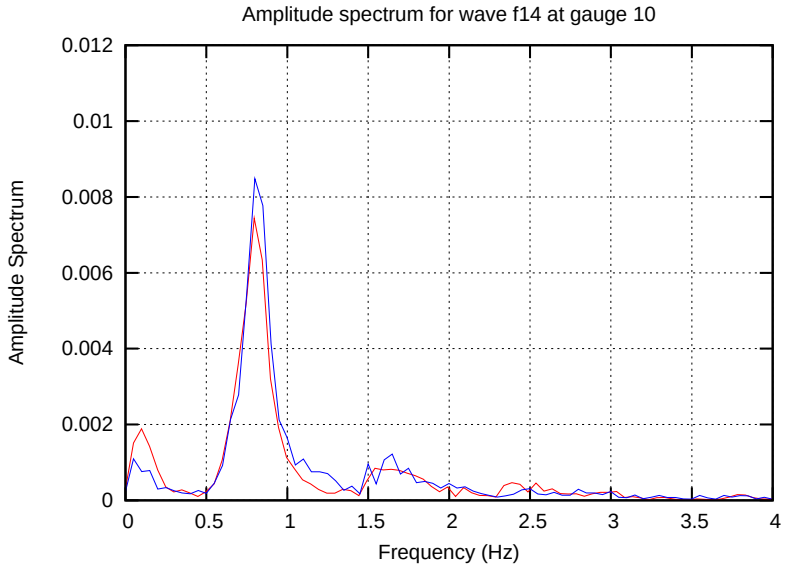


Figure 4.28: Graph showing the observed (blue and green lines) and modelled (red line) amplitude spectra at wave gauge 10 for case F14 with the beach and cylinder.

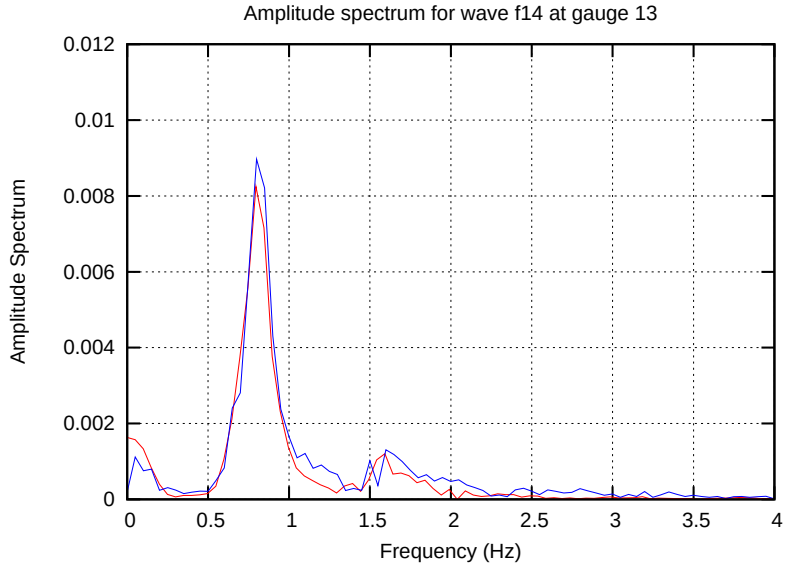


Figure 4.29: Graph showing the observed (blue and green lines) and modelled (red line) amplitude spectra at wave gauge 13 for case F14 with the beach and cylinder.

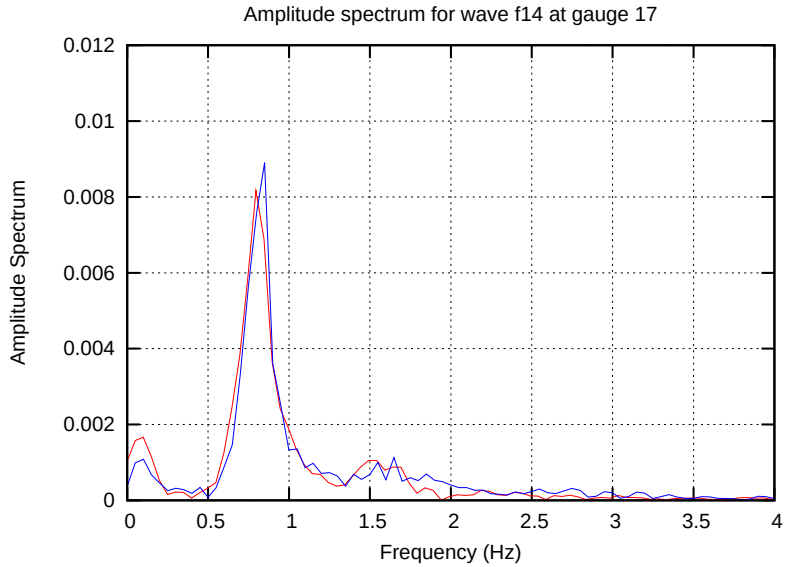


Figure 4.30: Graph showing the observed (blue and green lines) and modelled (red line) amplitude spectra at wave gauge 17 for case F14 with the beach and cylinder.

This difference is likely to explain the underestimation of the first order terms at gauge 9 for the flat bed case as the relatively coarse grid used for these tests will not accurately resolve the boundary layers on the face of the cylinder. This will have the effect of introducing a large numerical roughness to the surface of the cylinder which will dampen this run-up. The effect will be much less pronounced, however, on the sloping beach case, where the water slams into the face of the cylinder at right angles rather than running along its face.

**Direct force**

To assess the model's determination of direct force on the cylinder, the calculated total force on the cylinder was compared to the forces recorded during the experiment from the strain gauges. The pressure field on the cylinder surface was integrated to give the total force on the cylinder in the x direction. This approach neglects the forces due to the friction of the water on the surface of the cylinder but is very simple to apply and calculate. By contrast, accurate determination of the shear stresses is very difficult indeed as it would require either a grid that was extremely fine (and hence computationally expensive) or turbulence modelling which, as discussed elsewhere, brings several practical difficulties. The comparison between the modelled and recorded forces is shown in figures 4.32 and 4.33.

It can be seen that the model performs well in the initial part of the wave group but underestimates the peak force and the second half of the wave group. The comparison of the spectra also reveals that (not unexpectedly) the model, which uses a static, fixed, cylinder, does not reproduce the peak in the spectra at 3.9 Hz which is caused by the resonance of the cylinder at its natural frequency.

Short of introducing a model of the resonance of the cylinder into the interFoam model, it is not possible to represent the variation in force on the cylinder due to the cylinder's movement in the model. It is possible, however, to remove the effects of the high-frequency oscillation from the experimental data in order to effect a better comparison between the two datasets. This has been done using a low-pass filter. The filtered spectrum is shown in figure 4.34 and the resulting time series comparison is shown in figure 4.35.

It can be seen that while the model is still underestimating the peak forces slightly, the fit between the modelled and the experimental data is much improved through the use of the low-pass filter to remove the component of the force due to the natural frequency of the cylinder.

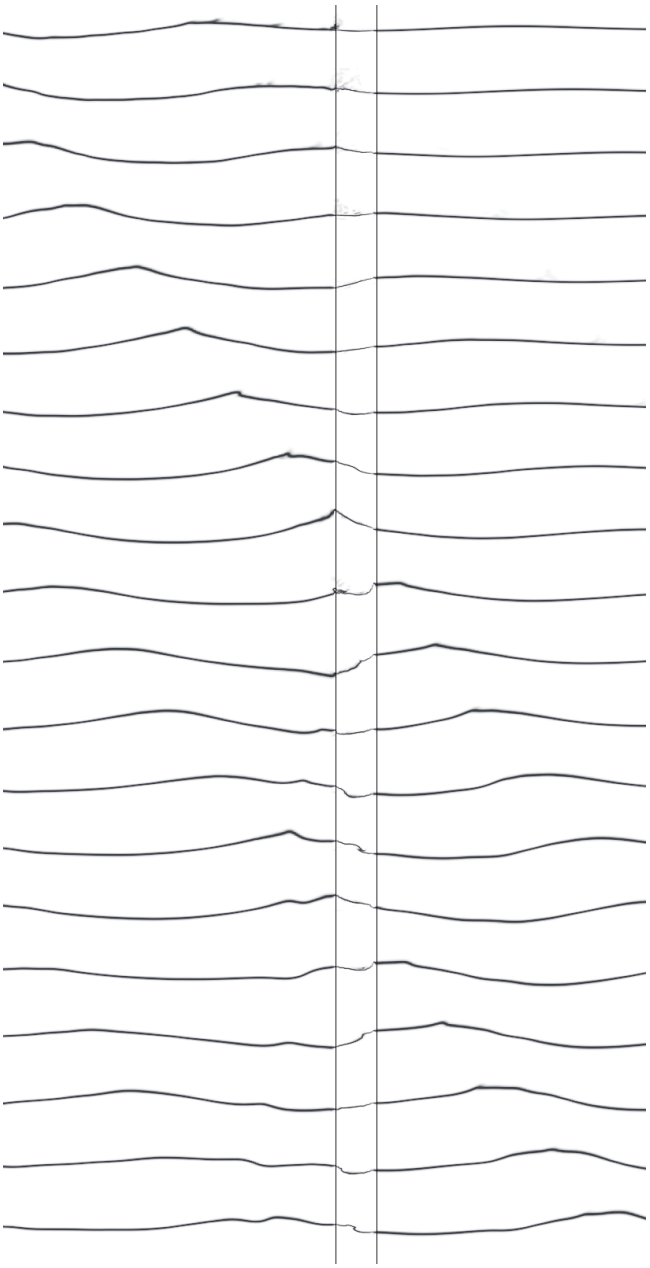

Figure 4.31: Snapshots of the water surface elevation of wave F14 with the cylinder on the flat bed at 0.2 s intervals.

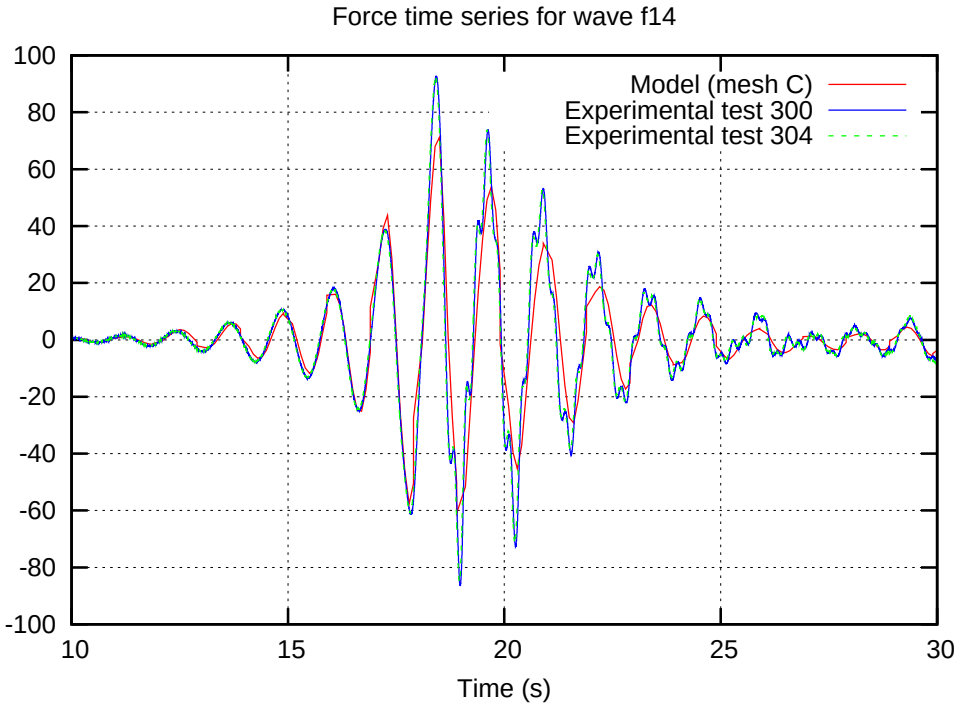


Figure 4.32: Graph showing the comparison between the modelled (red line) and the observed (blue and green lines) total forces on the cylinder.

The large peak in the modelled force spectrum at 0 Hz is indicative of the fact that, as the cylinder is embedded in a sloping bed, more of the cylinder is exposed on one side than the other. This causes integration of the pressures to give a constant force on the cylinder up the slope, which must be corrected for in the force series comparisons. In reality, this force did not exist as the cylinder had a flat base and was suspended slightly above the bed.

## 4.3 Practicality

The models shown here were run on test system B and were spread over four CPUs each. The models had approximately 5 million cells and required 3 GiB of RAM. The recorded run speed was approximately $5.0 \times 10^{-5}$ s/s allowing complete simulations to be run in approximately one week.

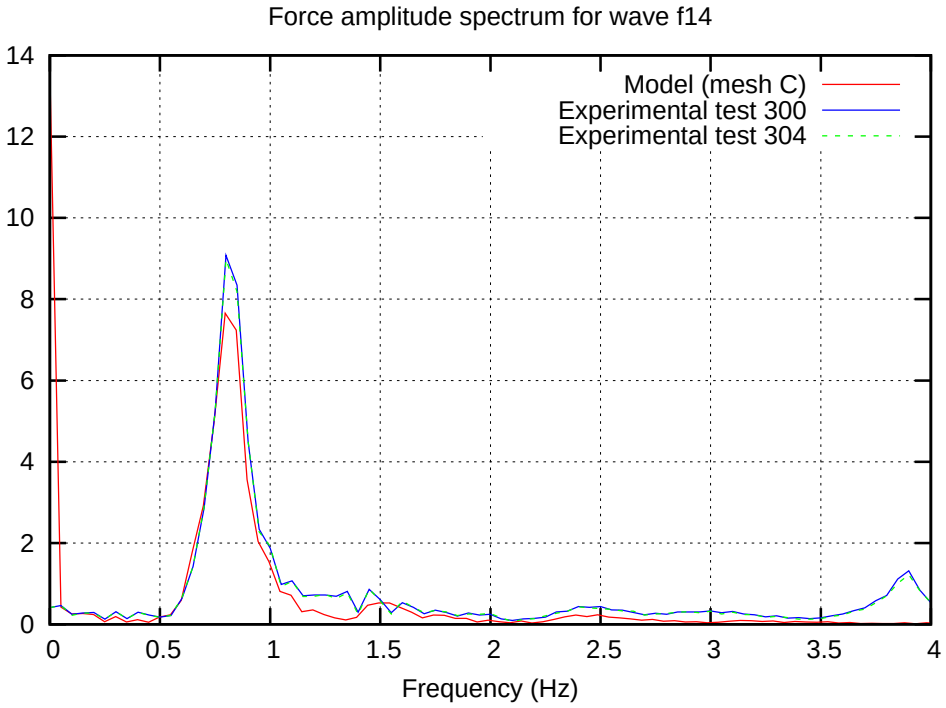


Figure 4.33: Graph showing the comparison between the modelled (red line) and the observed (blue and green lines) total force amplitude spectra on the cylinder.

## 4.4 Conclusions

The application of this new validation case to the model has shown not only that the model is capable of transmitting complex, non-linear wave forms such as focussed wave groups (which was also demonstrated in chapter 3) but also that the interaction between these waves and surface-piercing structures can be adequately modelled.

It has been demonstrated that the model can correctly reproduce the wave diffraction patterns around a circular cylinder, although it has no mechanism (in the form used here) for modelling the cylinder's dynamic response to the interacting waves. It is possible, using OpenFOAM, to model the cylinder using, for example, a linear elastic model to simulate its vibration and resonance and couple this dynamically to the hydraulic model. It is unlikely, however, that this will produce significantly better results than can be achieved using much simpler processes (such as a low-pass filter on the model results) and the additional computational

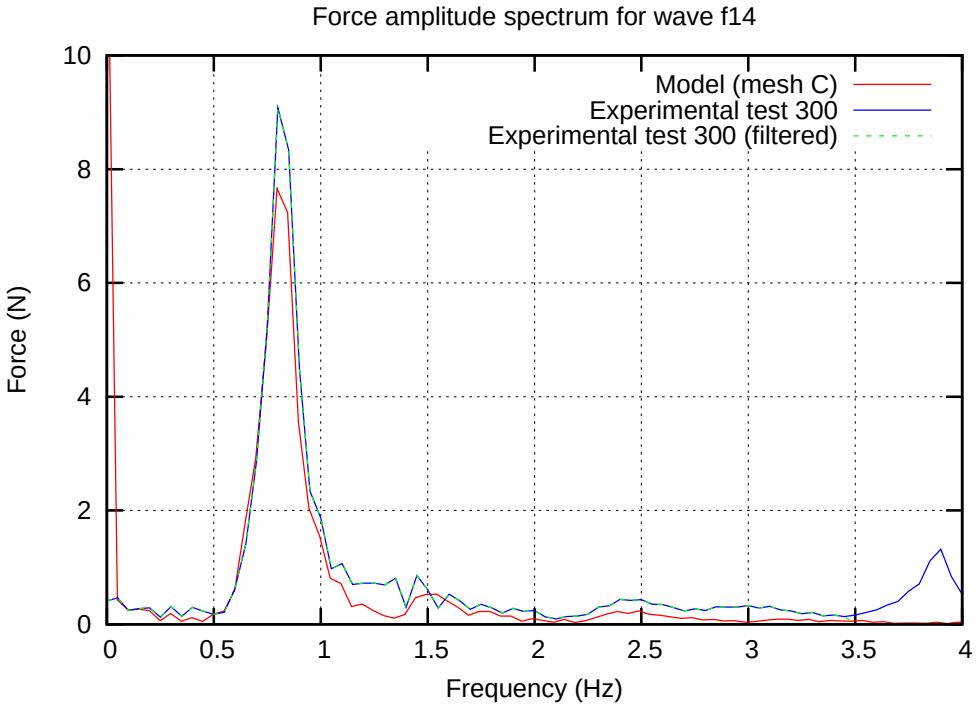


Figure 4.34: Graph showing the comparison between the modelled, observed and the filtered observed total force amplitude spectra on the cylinder.

expense of this approach is therefore hard to justify. Accordingly, further investigation of this approach is left for further work.

The simple procedure for integrating the pressures on the cylinder surface described in section 2.3 has been successfully used to estimate the total direct forces on the cylinder and these have been shown to be broadly similar to the direct forces recorded in the experiment, indicating that the sub-surface fluid pressures calculated by the model are likely to be accurate.

It was found that the models used here ran in a sufficiently short time period that they could be used by practising engineers without significant expense in either time or equipment. The pressure integration procedure used was found to be similarly practical as the time required to perform this was negligible compared to that of the model calculation as a whole.

The practicality of the focussed wave group for use in CFD was further demonstrated as it was shown to be faster to simulate the passage of

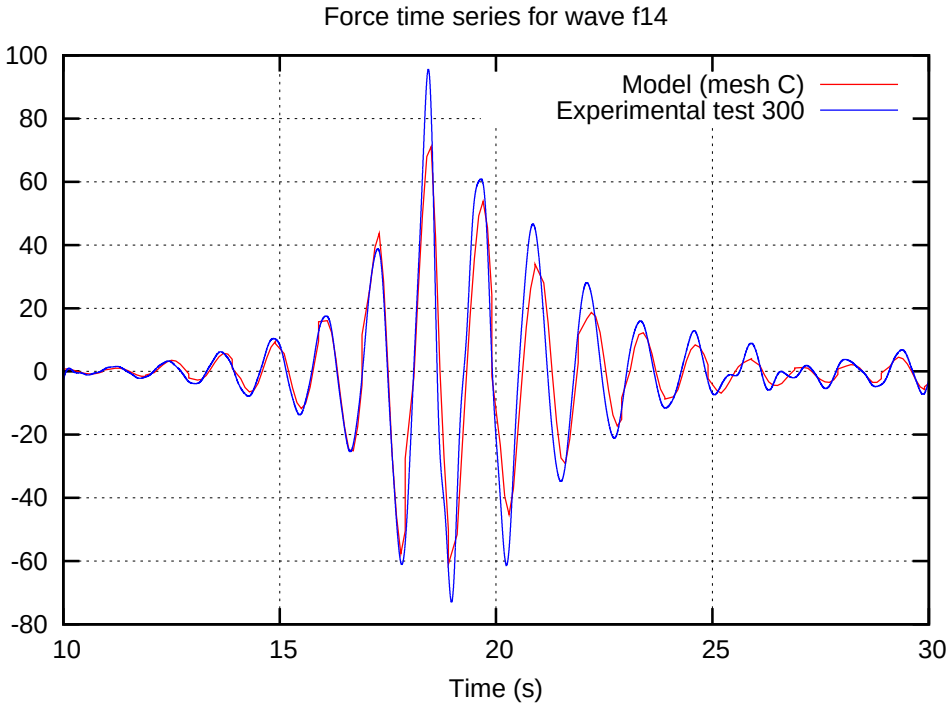


Figure 4.35: Graph showing the comparison between the modelled, observed and the filtered observed total forces on the cylinder.

a focussed wave group through the model than it was to simulate a comparable time period in which regular waves were propagating through the model.

# 5 Wave Action on Rubble Breakwaters

## 5.1 Validation Tests

Most coastal defences (and many fluvial defences) are not constructed from impermeable materials. Most coastal structures are formed from locally available sand covered with rock armouring. These structures are often permeable. As this permeability may have a significant effect on the fluid-structure interaction, particularly in the presence of waves, it is important for the model to be able to represent these effects. The permeability will also allow dynamic hydraulic actions, such as waves and tides, to create transient pore pressures within the structures themselves which could, in extreme circumstances result in failure.

The validation test case used here is based on an experiment conducted in 1997 at the Hydraulics and Coastal Engineering Laboratory at Aalborg University and are described in greater detail by Troch (2000). In these experiments a surface-piercing, porous breakwater structure was constructed in a wave flume and the interaction between this and various regular and irregular wave series was studied.

The approach was then used on a real-world case study of a complex, rock-armoured coastal defence structure. While, due to the limitations discovered in the validation case, the model could not be used quantitatively, the results were successfully used qualitatively to inform the design of the defence.

## 5.2 Aalborg Test Case

### Description of case

The experimental set-up of this case is shown in figure 5.1. The breakwater had one vertical face and one sloping face, with the waves hitting

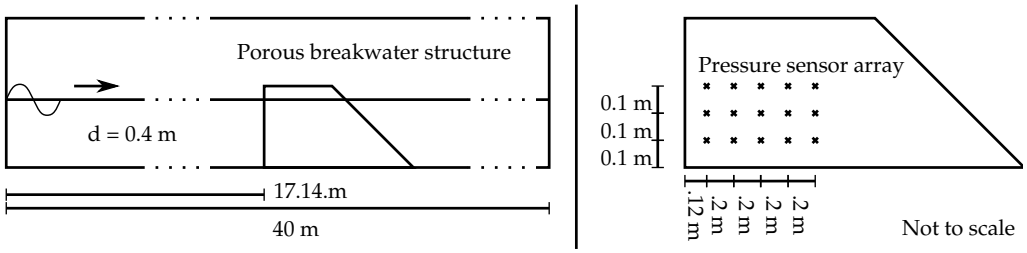


Figure 5.1: Schematic representation of the experimental set-up of the Aalborg test case.

the vertical face after propagating through 17.14 m of water with a depth of 0.4 m. The numerical flume was 40 m long to prevent reflections from the downstream face affecting the results at the breakwater, although in the validation cases the waves transmitted through the breakwater were sufficiently small that contamination of the results due to reflected waves would have been minimal.

The porous breakwater structure was instrumented with an array of $5 \times 3$ pressure sensors that were used to record the wave's progress through the structure. Five wave gauges were also used, with three monitoring the incoming wave, one on the front face of the breakwater and one in the flume behind the breakwater. This arrangement of wave gauges allowed the calculation of the breakwater's coefficients of reflection, run-up and transmission.

The breakwater was constructed from a medium gravel with a $D_{50}$ of 0.0181 m and a porosity of 0.426. Troch (2000) reports the Darcy-Forchheimer shape factors as $\alpha = 3009$ and $\beta = 2.45$.

As detailed wave time series of the irregular tests were not available, only the regular wave tests were used for the validation of the model. The wave cases that were used are given in table 5.1 with the results that were used for comparison in the validation tests.

The numerical flume used for the model validation was 40 m long and 1 m high and a two-dimension assumption was used. The mesh used is shown in figure 5.2. Rather than calculate reflected wave heights from the array of three wave gauges, a straightforward comparison between models with and without the breakwater was used.

It is not practical, in the approach used to model porosity in OpenFOAM to apply porosity to only parts of a cell. It was therefore difficult to accurately model the sloping back face of the breakwater without changing the simplified meshing approach described in section 2.6. However, the vast majority of the measurements involved in the model are not af-

| Wave ID | Wave Height, $H$ (m) | Wave Period, $T$ (s) | Results Available |
|---|---|---|---|
| r01 | 0.0370 | 2.84 | Coefficients |
| r02 | 0.0519 | 2.84 | Coefficients |
| r03 | 0.0655 | 2.84 | Coefficients |
| r04 | 0.0768 | 2.84 | Coefficients |
| r05 | 0.0493 | 2.38 | Coefficients |
| r09 | 0.0367 | 1.80 | Coeffs. & decay curves |
| r10 | 0.0543 | 1.80 | Coeffs. & decay curves |
| r11 | 0.0716 | 1.80 | Coeffs. & decay curves |
| r16 | 0.0554 | 1.60 | Coeffs. & wave gauges |

Table 5.1: Wave properties used in the "Aalborg" validation test cases.

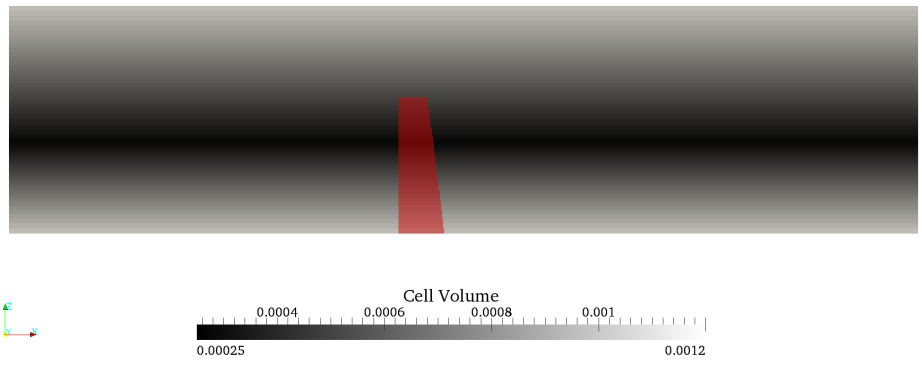


Figure 5.2: Distribution of cell volumes for the baseline mesh used in the Aalborg test case with horizontal scale reduced by 10 times.

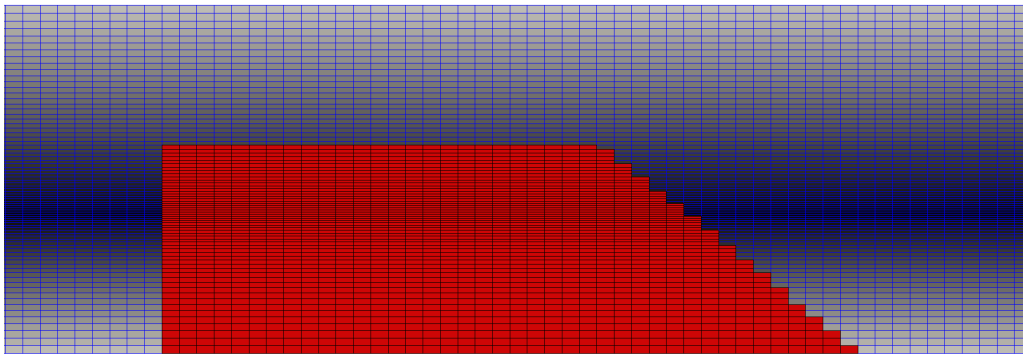

Figure 5.3: Detail of the mesh at the porous breakwater with cells applying the Darcy-Forchheimer equation highlighted (correct aspect ratio).

fected by the precise representation of the back face of the breakwater. The meshing procedure was therefore kept simple and the back face of the breakwater was represented using a stair-step approach as shown in figure 5.3.

## Initial validation results

The information available in Troch (2000) was, for each wave, the reflection coefficient, $C_r$, and for some of the waves, the wave decay through the breakwater measured by the pressure gauges or the water surface elevations recorded by the wave gauges. Table 5.2 shows the measured reflection coefficients for each wave and the corresponding model coefficient (derived from a comparison between models with and without the breakwater in place).

It can be seen that the model severely underestimates the reflection coefficients. This is due to the reported values of the Darcy-Forchheimer coefficients being used in the model despite the very dynamic flow conditions.

## Parameter Search

The initial validation results above demonstrate that it is critical to have an understanding of how sensitive the model is to errors in the parameters $n$, $\alpha$ and $\beta$ as it is extremely difficult to accurately determine these values without extensive testing of the in-situ material. It was shown in

| Wave ID | $C_r$ observed | $C_r$ modelled |
|---|---|---|
| r01 | 0.744 | 0.326 |
| r02 | 0.788 | 0.303 |
| r03 | 0.839 | 0.309 |
| r04 | 0.862 | 0.420 |
| r05 | 0.695 | 0.344 |
| r09 | 0.677 | 0.259 |
| r10 | 0.698 | 0.211 |
| r11 | 0.716 | 0.242 |
| r16 | 0.675 | 0.267 |

Table 5.2: Comparison of reflection coefficients for each modelled wave in the Aalborg test case using the reported Darcy parameters.

section 2.4 that, while methods exist for estimating $\alpha$ and $\beta$ from $n$ and $D_{50}$, these methods are highly variable and can lead to answers that differ by orders of magnitude from other, similarly accepted formulae.

In order to investigate this variability, models were run for a wide variety of porosity parameters. Table 5.3 shows all the values of all the parameters that were studied as part of this work. These values were derived by estimating the $\alpha$ and $\beta$ values for the breakwater using every equation discussed in Sidiropoulou *et al.* (2007) and converting these to the $D$ and $F$ parameters to define the plausible range for each parameter. All the possible combinations of these parameters were simulated, leading to a total of 3,780 model simulations. From these simulations, plots were made showing how the wave transmission, wave run-up, and wave decay through the breakwater was affected by the changes in each parameter.

A preliminary analysis of these results indicated that, within the ranges tested, the model was very insensitive to the value of the Forchheimer parameter, $F$. $F = 0.2$ has been used in all the subsequent results except where noted.

The model was shown to be extremely sensitive to the value of $D$ and moderately sensitive to the value of $n$. This can be demonstrated by figure 5.4 which is typical of the results from the parameter search as a whole. Figure 5.4 shows how the coefficients of reflection, transmission and run-up vary with the values of $D$ and $n$ for wave r16.

| Variable | Values used | Number of Values |
|---|---|---|
| Wave ID | r01, r02, r03, r04, r05, r08, r09, r10, r16, r17, r18, r19 | 12 |
| Porosity, $n$ | 0.1, 0.2, 0.3, 0.4, 0.5, 0.6, 0.7, 0.8, 0.9, 1.0 | 9 |
| Darcy Param. $D$ | $4 \times 10^{-6}$, $6 \times 10^{-6}$, $8 \times 10^{-6}$, $1 \times 10^{-7}$, $2 \times 10^{-7}$, $3 \times 10^{-7}$, $4 \times 10^{-7}$ | 7 |
| Forchheimer Param. $F$ | 0.02, 0.05, 0.2, 0.5, 2.0 | 5 |
| | Total Simulations | 3,780 |

Table 5.3: Parameters used in the Aalborg parameter search.

## Model calibration

The results from the parameter search indicated that it was necessary to calibrate the model. As it is expected that the value of $n$ will be much better defined using laboratory tests and theory than the value of $D$, the Darcy parameter was chosen as the primary calibration variable. The model was calibrated using the results from the parameter search to compare the modelled wave decay curve for wave r09 with the experimentally recorded curve. The results of this comparison are shown in figure 5.5.

This figure shows the modelled and recorded wave amplitudes (measured in Pascals) from the pressure gauge array. It is worth noting that a perfect fit to the experimental data is not possible using the current model as the experimental data indicate that the wave amplitude increases between the fourth and fifth pressure sensors. Such an increase in wave amplitude is not modellable by the Darcy-Forchheimer equation. Despite this drawback, however, the value $D = 1 \times 10^7$ was selected to produce the closest fit between the modelled and observed data.

## Calibrated results

Figures 5.6–5.8 show the measured wave decay curves reported by Troch plotted against the modelled wave decay curves using this calibrated value of the Darcy parameter. It can be seen that the fit is reasonable for these larger waves as well as the r09 wave.

Table 5.4 shows the reflection coefficients from the calibrated model compared to those derived from the experiment. It can be seen that,

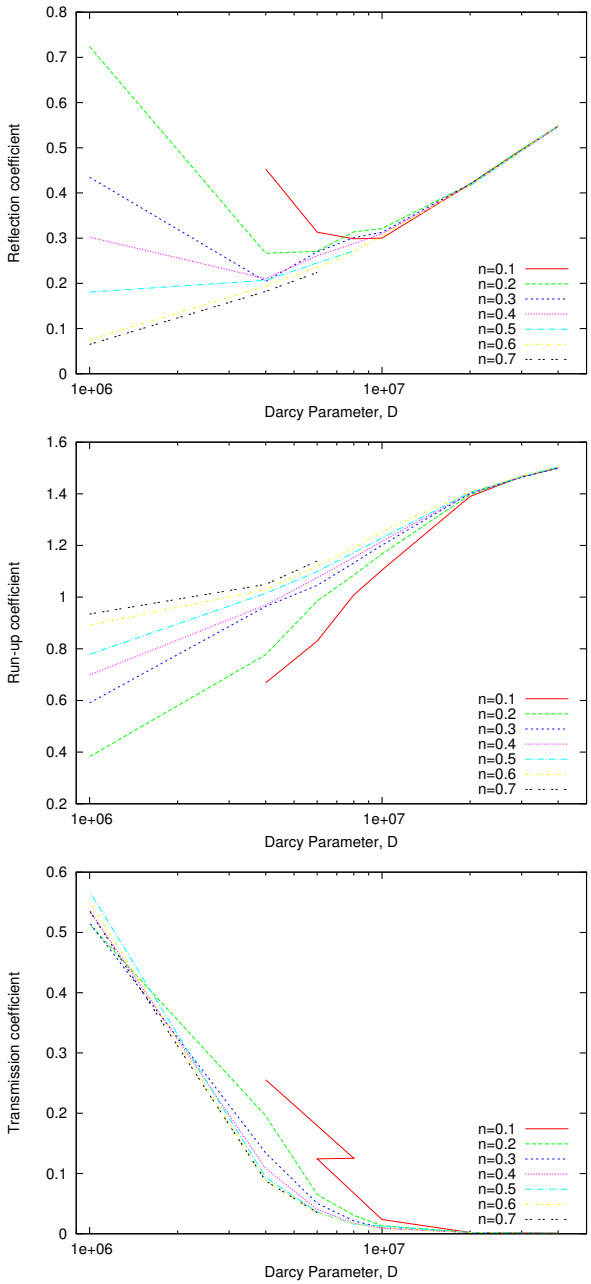


Figure 5.4: Graphs showing the effect of the $D$ and $n$ parameters on the wave reflection, run-up and transmission coefficients.

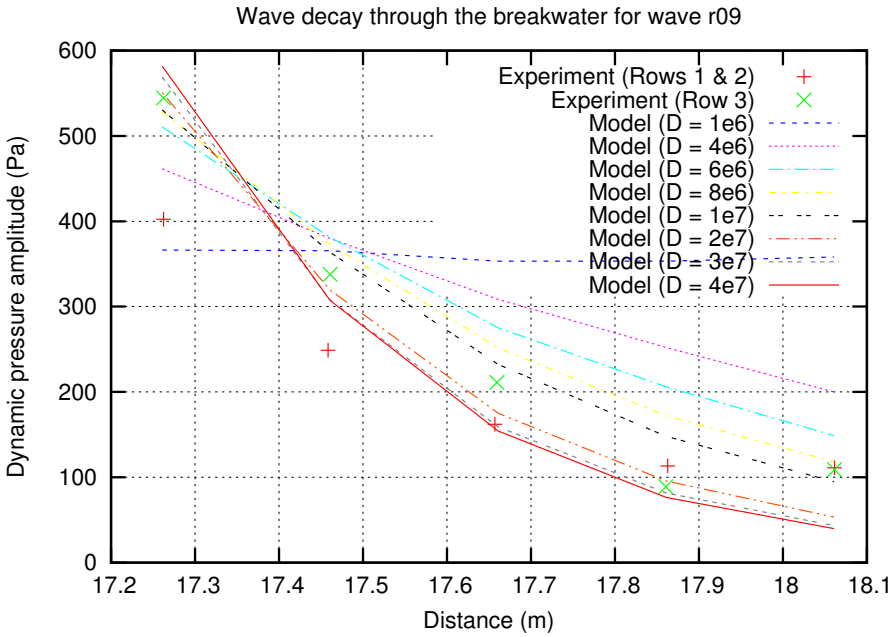


Figure 5.5: Comparison of experimental results to the modelled wave decay curves through the breakwater for wave r09 with $n = 0.4$.

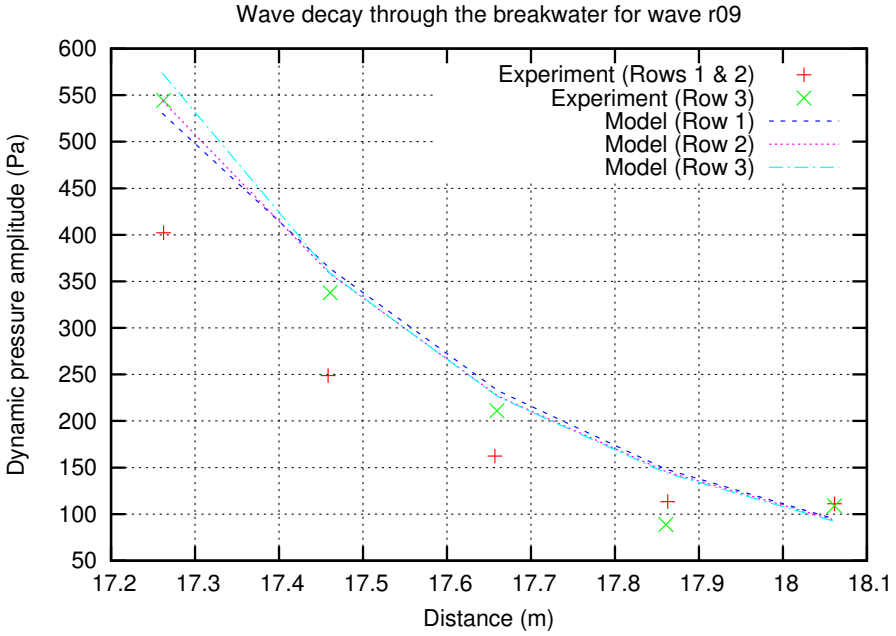


Figure 5.6: Comparison of experimental results to the calibrated model's wave decay curves through the breakwater for wave r09 with $n = 0.4$.

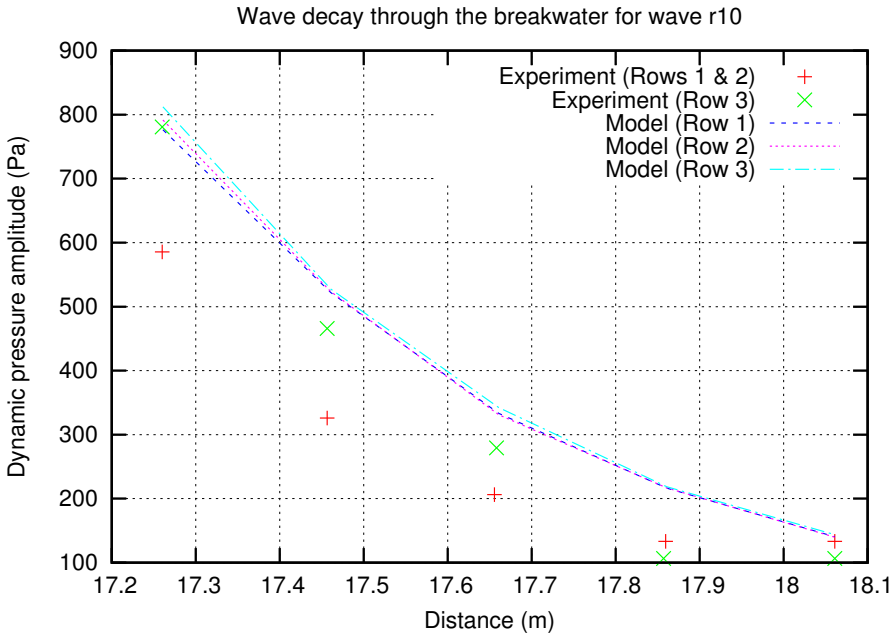


Figure 5.7: Comparison of experimental results to the calibrated model's wave decay curves through the breakwater for wave r10 with $n = 0.4$.

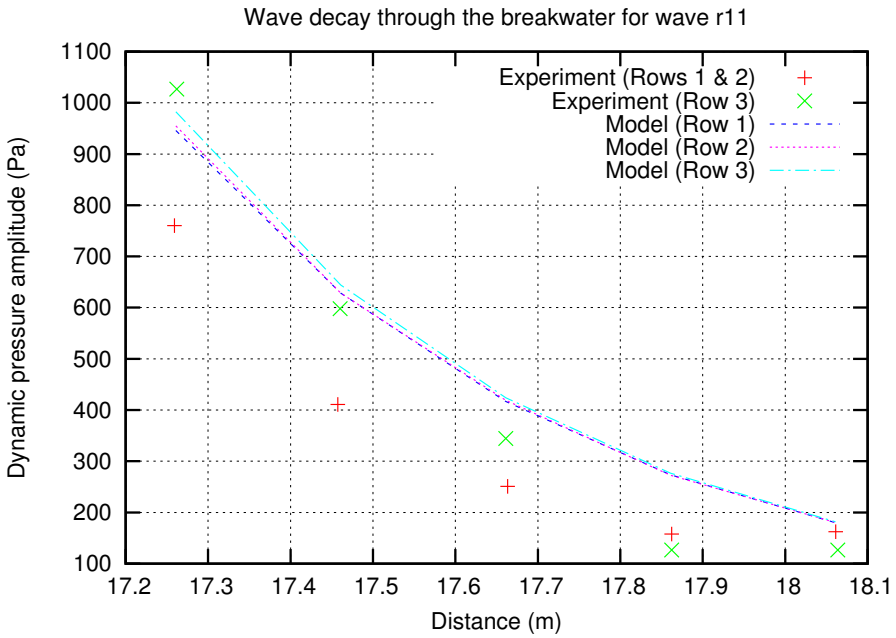


Figure 5.8: Comparison of experimental results to the calibrated model's wave decay curves through the breakwater for wave r11 with $n = 0.4$.

| Wave ID | $C_r$ observed | $C_r$ modelled |
|---|---|---|
| r01 | 0.744 | 0.717 |
| r02 | 0.788 | 0.712 |
| r03 | 0.839 | 0.714 |
| r04 | 0.862 | 0.750 |
| r05 | 0.695 | 0.656 |
| r09 | 0.677 | 0.611 |
| r10 | 0.698 | 0.605 |
| r11 | 0.716 | 0.626 |
| r16 | 0.675 | 0.644 |

Table 5.4: Comparison of reflection coefficients for each modelled wave in the Aalborg test case using the calibrated Darcy parameters.

while the model still generally underestimates the reflection coefficients, the accuracy of the calibrated model is much better than the initial model.

### Mesh Sensitivity

The above models were conducted on two meshes, with the results shown above being from the coarser of the two. The finer mesh was formed by evenly subdividing each cell in the coarse mesh into four. A comparison of the results from the two meshes is shown in figures 5.9 (comparing the water surface elevation away from the breakwater) and 5.10 (comparing the pressure fluctuations at the central pressure gauge). It can be seen that the increased mesh density does not have a significant effect on the results.

## 5.3 Coastal Defence Case Study

### Background

This case study describes the use of interFoam in a qualitative manner to assess flow patterns around a complex rock-armoured sea defence structure. The model results were used to inform the engineering design team about potential locations of scour and rock armour damage. interFoam was selected for this project as there was insufficient money available to do a physical model but the structure was sufficiently complex that it was

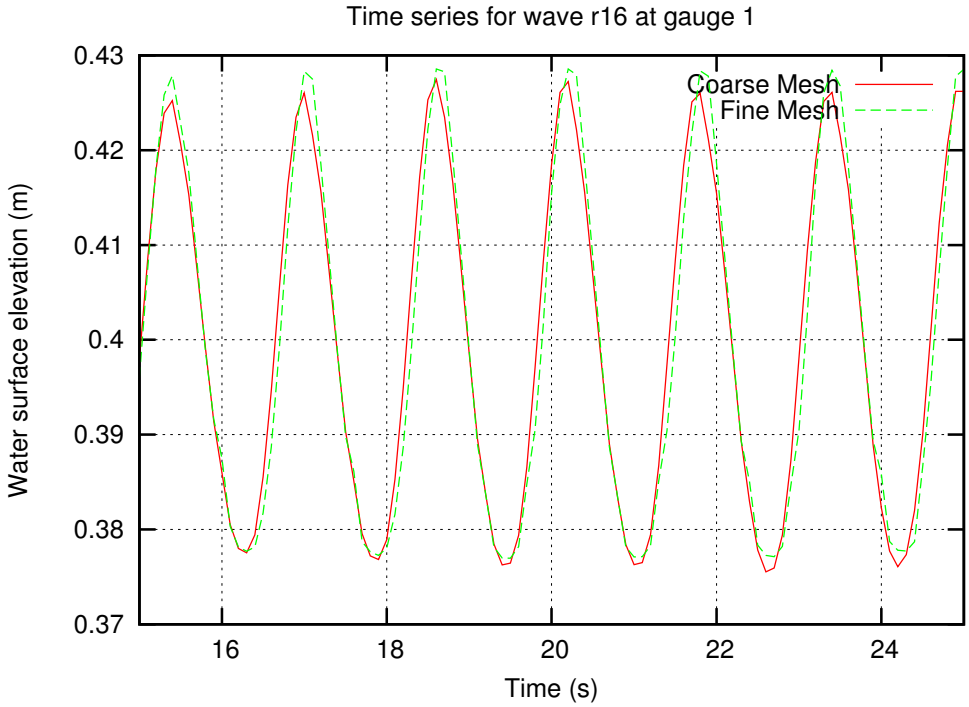


Figure 5.9: Modelled incoming wave on the two meshes.

felt important to supplement standard design methods with a greater understanding of flow through the structure.

interFoam was used in this case as the structure was subject to several critical design constraints which fixed, in some areas, the location of both the toe and the crest of the defence, resulting in an unusually steep structure on the eastern side. An additional constraint on the project was provided by the local scarcity of large armour stones leading to a maximum possible armour stone weight of 3 t. Figure 5.11 shows a schematic from an initial design stage. The red line shows the seaward constraint to the east while the innermost line represents the landward constraint.

The shape of the land to be protected made the use of many conventional design methods difficult. The defence could neither reasonably be considered to behave as a linear defence of infinite length nor to be a classic "round-head" shape. Further, the design required integration with other defence schemes, designed independently. As has already been noted, the interfaces between coastal and flood defence structures are often found to be the weakest points and therefore require special attention. The CFD modelling was used to assess potential flow or stress

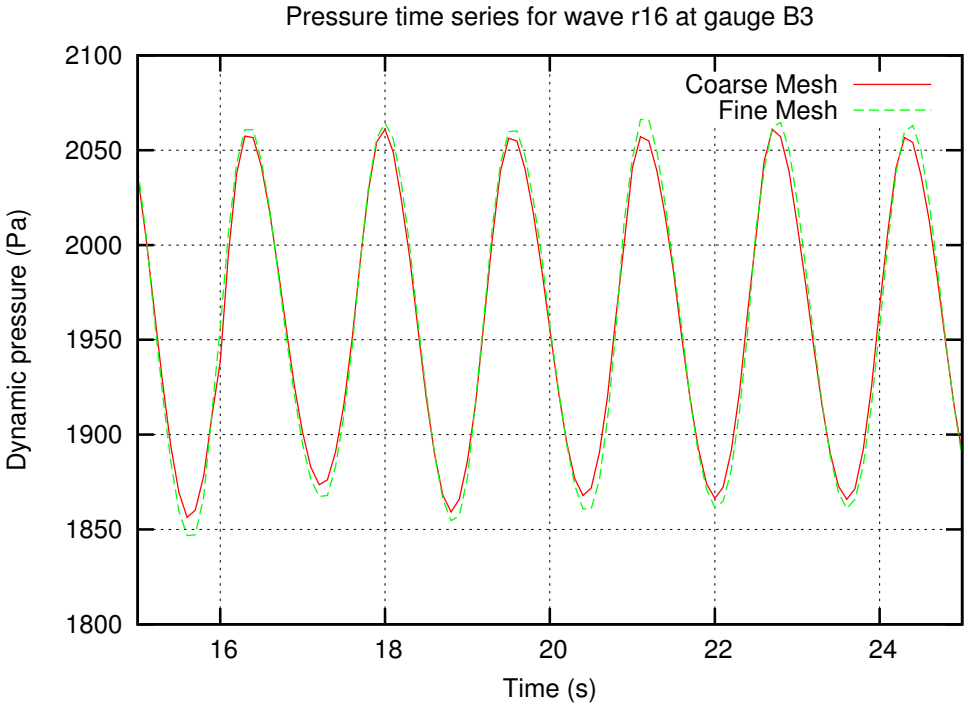


Figure 5.10: Modelled pressure fluctuations from the central gauge on the two meshes.

concentrations caused by the interface of the different schemes.

## Simulations

A total of six simulations were carried out as part of this project, covering three wave directions with two potential structure designs. The simulations were performed using regular waves with H = 2.25 m and L = 43 m and were run for sufficient time for three complete waves to interact with the structure.

The critical wave directions were determined to be 330°, 0° and 30°. Rather than introduce the waves into the domain at an angle, the waves were introduce into the domain travelling perpendicular to the source face and the structure was rotated, creating a new mesh for each incident wave angle. This allowed additional wave-guide structures to be placed in each mesh to control the reflected waves by reflecting them out into the areas of the model away from the area of interest.

In the models, the sand core of the structure was modelled as a solid (non-porous) structure with the two gradings of armour covering it mod-

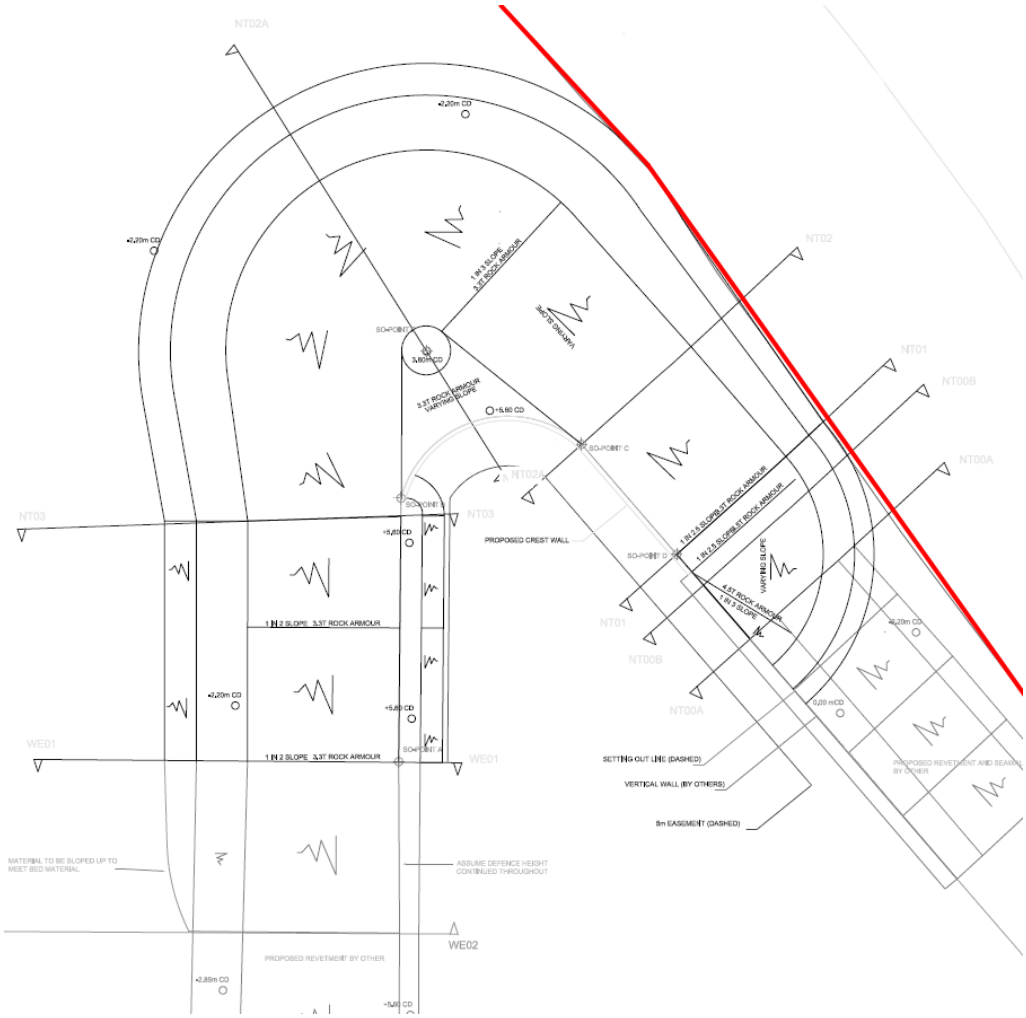


Figure 5.11: Plan of an early design of the coastal defence, showing seaward constraint to the east (red).

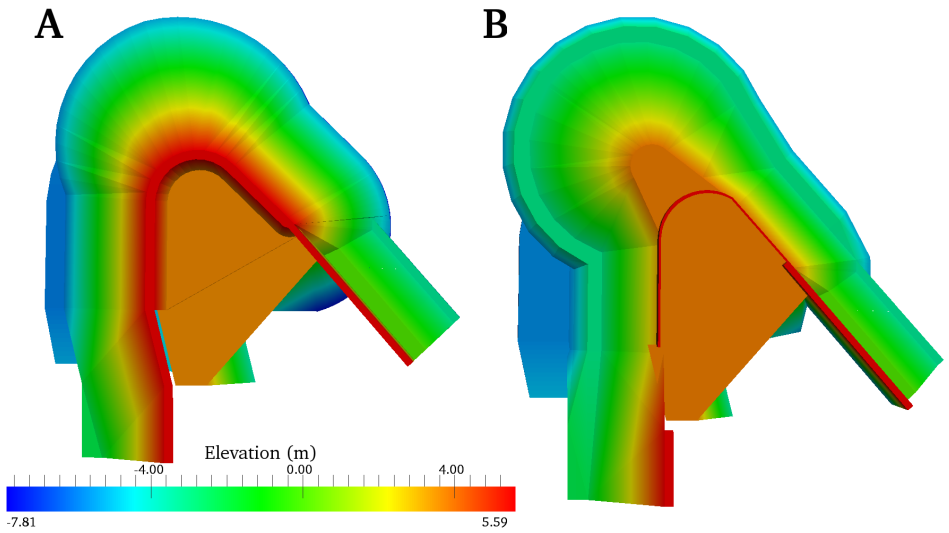


Figure 5.12: Overview of structures A and B showing the outer layers of the rock armour and the vertical walls.

elled using two different levels of porosity. In the absence of reliable data for the porosity of rock armour layers the porosity parameters for these layers were estimated from comparable values in table 1 of Sidiropoulou *et al.* (2007). It is the large uncertainty in these values that renders this particular set of models only reliable for qualitative use. The adopted values for the outer rock armour porosity were $n = 0.4$, $D = 2.5 \times 10^3$ and $F = 4 \times 10^{-3}$; while the inner rock armour was modelled with $n = 0.4$, $D = 4 \times 10^3$ and $F = 4 \times 10^{-3}$.

Two designs for the structure were tested, and images of these designs are shown in figure 5.12. The figures show the structures in plan, with the outer layers of the rock armour indicated. Structure A was the original design, based only on conventional engineering design procedures, while structure B was an improved design, made after the numerical tests from structure A had been processed.

The meshes for each domain are shown in figures 5.13 and 5.14. It can be seen that in addition to the solid cores of the structures to be studied, other shapes have been "cut out" of the domain either to remove areas of the model where insufficient data was available, control wave reflections, or remove areas of the model which represented unnecessary computational expense. It should be noted that the figures still show the mesh used to model the porous armour layers—only the inner, sand core has

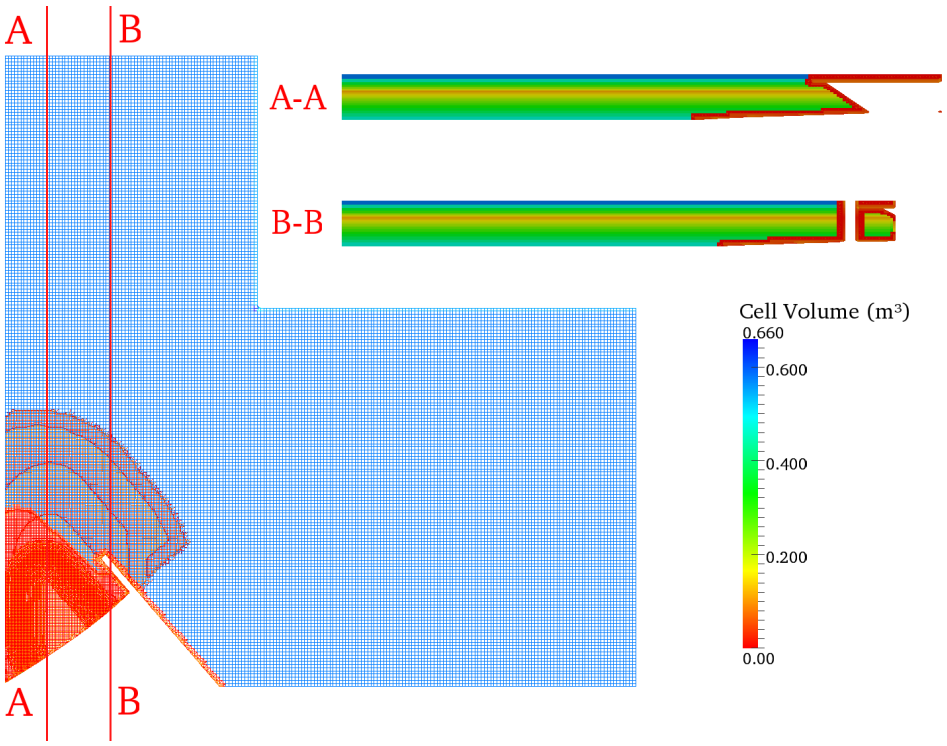


Figure 5.13: Overview of computational mesh for structure A with incoming waves at 0°.

been removed.

## Results

## Structure A

Visualisations of the results from structure A are shown in figures 5.15–5.17. Two critical issues with the initial design of structure A were identified by the CFD modelling and the resulting visualisations.

Figure 5.15 illustrates that waves impacting on structure A cause a flow concentration at the interface between the steep section of rock armour on the eastern side and the vertical wall structure that was part of the existing design. Geometric changes were made to the layout of the embankment to mitigate this flow concentration.

Figure 5.16 shows that a significant flow of water could occur through the rock armour layers in the steepest part of the slope. It was considered that the strength of this flow, depending on the nature of the incoming

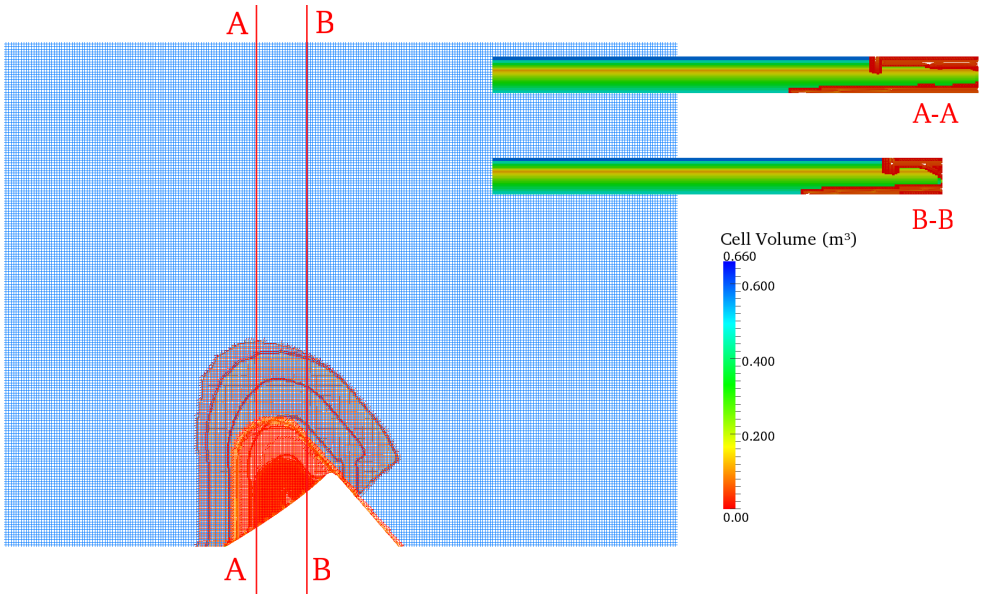


Figure 5.14: Overview of computational mesh for structure B with incoming waves at 0°.

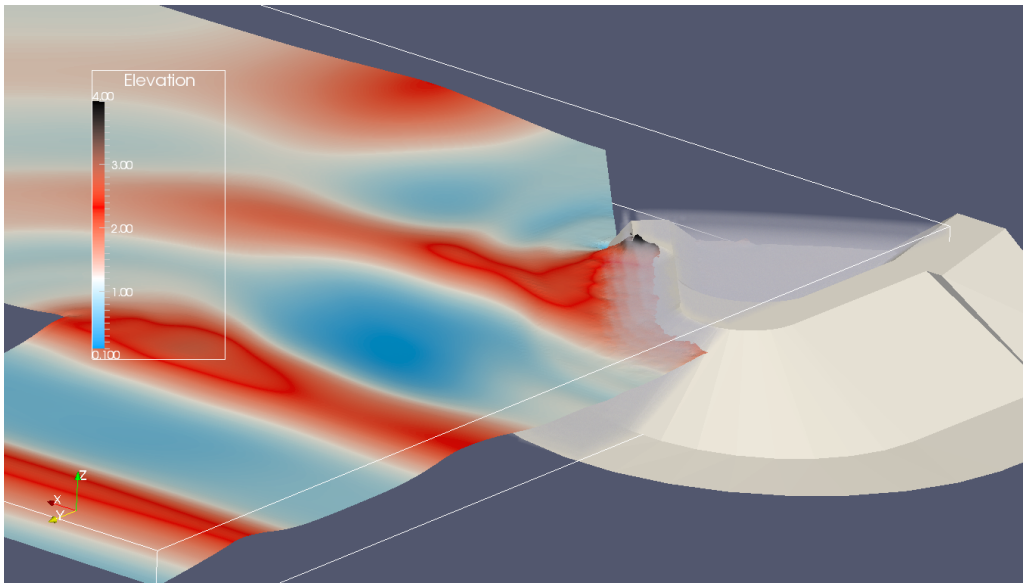


Figure 5.15: Oblique view of structure A with waves from 0° showing flow concentration within the rock armour behind the vertical wall.

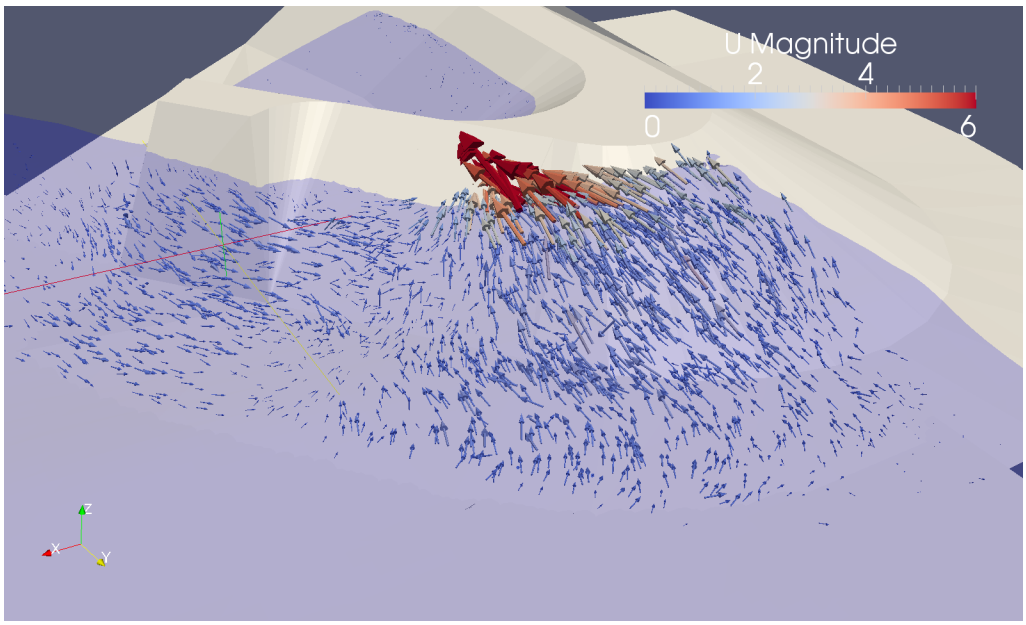


Figure 5.16: Oblique view of structure A with waves from 0° showing high velocities within the rock armour.

wave, could be sufficient to cause "plucking" of the rocks from the rock armour layer and instigate damage to the defence. Accordingly, the design of the embankment was changed slightly to give the steep slope more protection from incoming waves.

Figure 5.17 is a plot of the near-bed velocities from the model in the vicinity of the structure. The red and purple areas indicate high velocity and hence greater probability of scour at the toe of the embankment. It can be seen that the velocities are well distributed along the toe, suggesting that toe scour at the embankment will be relatively even.

## Structure B

Based on the results from the models of structure A, as well as other calculations, the design was revised to the form of structure B. The interface between the structure and the vertical wall on the east side of the site was altered and the "head" of the structure was enlarged to afford more protection to the vulnerable steep slope.

Figure 5.18 shows the revised interface design at the same instant of model time as figure 5.15. It can be seen that less water is directed behind the vertical wall.

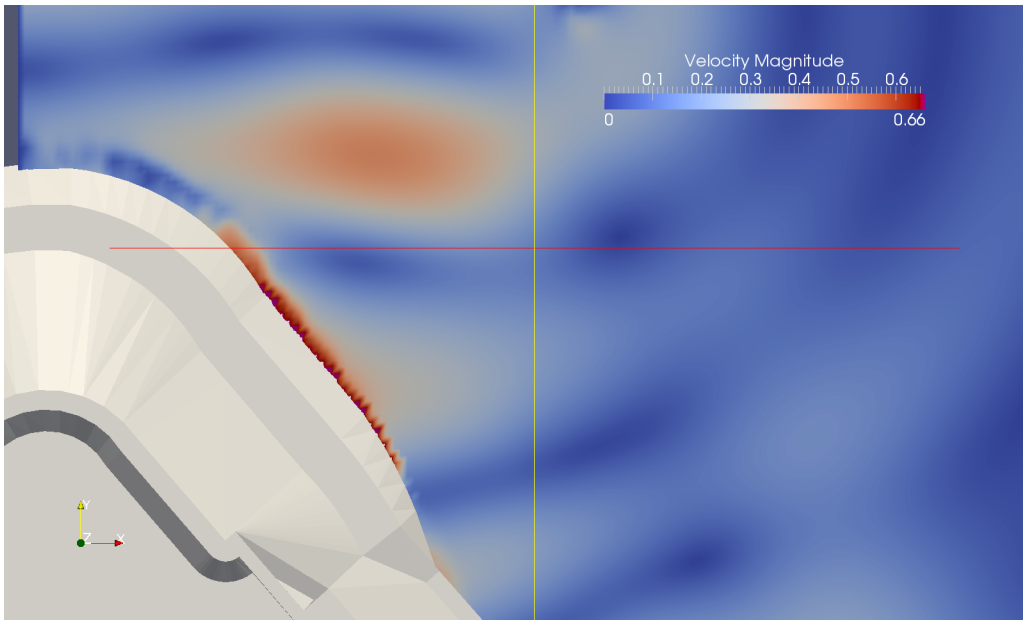


Figure 5.17: Plan view of structure A with waves from 0° showing high near-bed velocities at the toe of the structure.

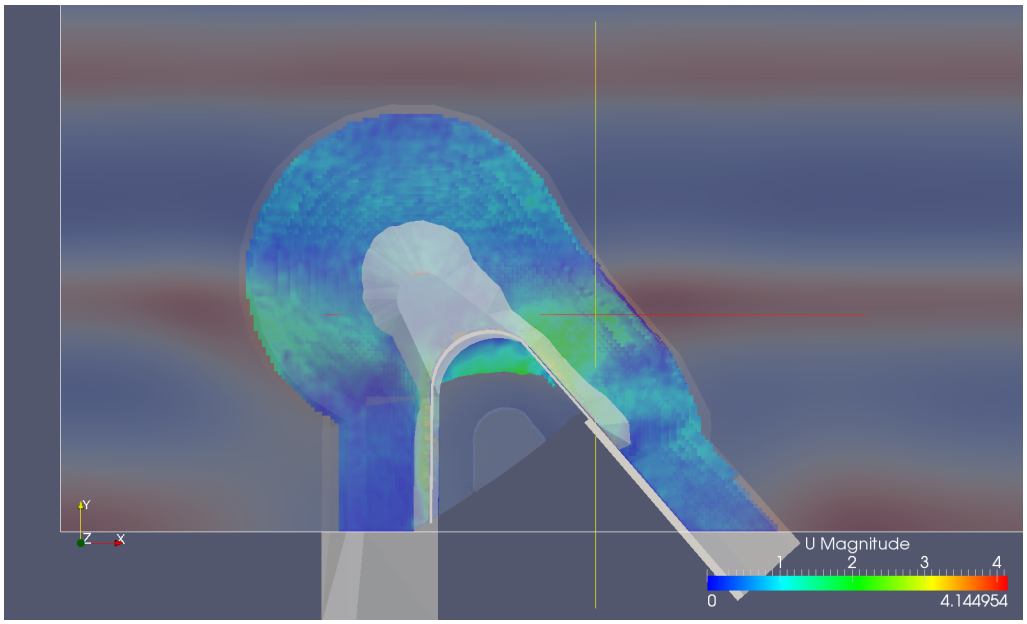


Figure 5.18: Plan view of structure B with waves from 0° showing velocities on the surface of the rock armour.

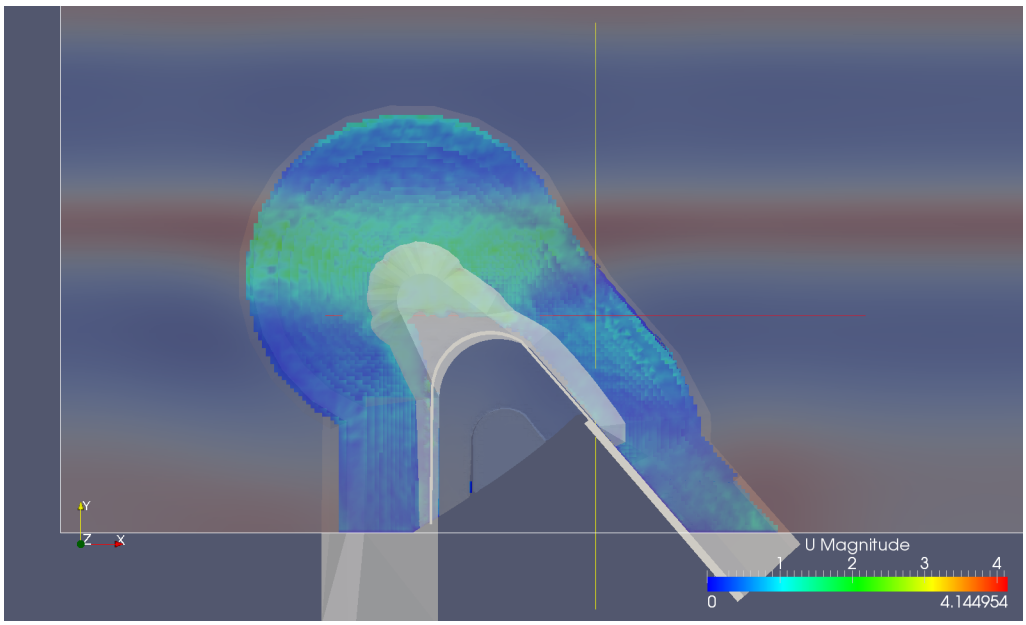


Figure 5.19: Plan view of structure B with waves from 0° showing velocities on the surface of the rock armour.

Figure 5.19 shows the flow through the rock armour layers in structure B at the same instant as 5.16. It can be seen that the additional structure and rock armour at the head of the structure has reduced the flow through the steep section of rock armour.

## 5.4 Practicality

The preceding chapters have already shown that simple two-dimensional models of wave transmission are sufficiently fast to be practically applicable in a practical engineering design context, however this validation test has two differences from the earlier wave transmission tests which affect the practicality of the model.

The first, and most critical of these differences is the presence of the porous media in the domain. It is clear that the presence of the porous media will cause the model to be slightly slower as the Darcy and Forchheimer terms must be calculated in addition to the equations that would normally be solved.

The porous media implementation in OpenFOAM mitigates the effects of this to some extent by only calculating the Darcy and Forchheimer parameters as a correction to the Navier-Stokes equations for the

| Darcy Parameter | Forchheimer Parameter | | | | |
|---|---|---|---|---|---|
| | 0.02 | 0.05 | 0.2 | 0.5 | 2.0 |
| $1.0 \times 10^{-6}$ | 3411 | 3355 | 3439 | 3253 | 2999 |
| $4.0 \times 10^{-6}$ | 2608 | 2630 | 2610 | 2598 | 2580 |
| $6.0 \times 10^{-6}$ | 2655 | 2643 | 2638 | 2625 | 2591 |
| $8.0 \times 10^{-6}$ | 2518 | 2526 | 2614 | 2516 | — |
| $1.0 \times 10^{-7}$ | 2444 | 2446 | 2443 | 2443 | 2444 |
| $2.0 \times 10^{-7}$ | 2608 | 2608 | 2608 | 2608 | — |
| $3.0 \times 10^{-7}$ | 2802 | 2803 | 2803 | 2802 | 2806 |
| $4.0 \times 10^{-7}$ | 2893 | 2893 | 2894 | 2894 | 2893 |

Table 5.5: Number of timesteps required for 40 s simulation of case r16 with a variety of porosity parameters.

cells in which porosity is applied. No additional computation is necessary for non-porous cells.

The porosity of the cells also has secondary effects on the run speed, however. Porous media in the simulation can have a dampening effect on the fluid velocity. Due to the adaptive timestepping approach used here, this has the potential to cause an increase in run speed as the simulation's maximum velocity may fall and the timestep can therefore be increased to maintain a constant maximum Courant number.

Cells in the domain with very low porosity or permeability, however, have the potential to decrease the run speed. As the effects of porosity are applied to the simulation in the form of a correction at the end of each solution iteration, the more the porosity changes the result compared to the solution with no porosity applied, the more iterations are required to effect that change.

It has already been shown that models of this size can be run in reasonable time, but it is interesting to observe the effect that different levels of porosity have on the timestep. Table 5.5 shows the number of timesteps required to complete a 40 s simulation with wave r16 and a porosity of 0.3 for various values of the $D$ and $F$ parameter. It can be seen that the Forchheimer parameter has little effect on the number of timesteps within the range tested but that the models exhibit a greater dependency between the number of timesteps (and hence the run time) and the value of the Darcy parameter, $D$.

The second difference between this model and the wave transmission tests described in chapter 3 is that this test has no solid structures within the numerical flume. The result of this is that there are no cut cells: all

of the cells in the mesh are hexahedral and the mesh is purely orthogonal. This allows several solution iterations which are normally run to correct for non-orthogonality in the mesh to be neglected, resulting in an increase in run speed.

This run speed increase is difficult to measure effectively. The computation time required for the correction steps varies depending on the non-orthogonality of the mesh (the steps take very little time on orthogonal meshes) and a comparison cannot be made on a non-orthogonal mesh as the calculated results would be wrong for the test without the non-orthogonal correctors and this error would affect the adaptive timestepping and therefore the run speed. It is clear, however, from observation of the model during a run, that these correction steps do take an observable amount of time and that there is therefore a run speed advantage in using purely orthogonal meshes.

## 5.5 Conclusions

This validation test case has shown that the modified model is capable of modelling porous media by applying a correction to the Navier-Stokes momentum equation based on the Darcy-Forchheimer equation using the process described by Hafsteinsson (2009). The model is capable of producing wave decay through porous media and the qualitative nature of the results match what might be expected of a Darcy-Forchheimer–based model.

The use of porous media is complicated by the sensitivity of the model to the Darcy parameter and the fact that laboratory-derived values of the Darcy parameter are not generally suitable for use in models involving dynamic flows or waves due to the dependency of the Darcy and Forchheimer parameters on the nature of the fluid flow.

It has been shown that, because of this strong dependency on an accurate and appropriate value of the Darcy parameter which is generally not available, the simulation of porous media requires calibration against observed data for the structure under test or structures with similar material. Without such calibration, the results from the CFD modelling of porous media must be treated as a purely qualitative result.

It has been shown that, even with the addition of porous media to the model, simulation run speeds remain practical for engineering and design problems. The use of porous media can have both positive and negative effects on the speed of a model and it may even be possible to

use porous media (in areas of the domain which are of little interest) to reduce maximum velocities and hence increase model run speeds.

A practical advantage to using purely orthogonal meshes was identified, allowing run speeds to be increased in cases where the structure under test, like the one used in this validation, consists entirely of porous media. The magnitude of this speed advantage could not be adequately ascertained.

The coastal defence case study has shown that the model remains practical even when modelling fully three-dimensional structures and that, even in the absence of reliable data for the Darcy and Forchheimer parameters, the model can be useful to design engineers as a qualitative tool. Several design issues can be identified by using the three-dimensional modelling approach which would have been difficult to identify using traditional engineering design methods, which do not cover complex or unusual geometries or the interfaces between different geometries which are often critical to the failures of defences (Allsop *et al.* 2007).

While the run-times of the models used in the case study were not insignificant, it is important to note that the engineer-time required to prepare, run and process the models and their results was very small due to the simplified meshing procedure and the ease with which the three-dimensional structure models could be created. The computational time required for the modelling was not significantly different to the time taken by the engineering team to fully assess the defence using traditional methods and the two processes could therefore proceed simultaneously, with very little additional cost associated with the use of the CFD.

# CONCLUSIONS 6

Three-dimensional wave-structure interaction is a complex process the simulation of which requires complex, three-dimensional modelling if the processes involved are to be completely understood. The interaction of violent and breaking waves with shallow submerged or surface-piercing structures such as breakwaters, bars, sea defences and wind turbine columns is an important consideration in the design of these structures and there is a need for practical numerical models that can assist engineers at the design stage without the time and expense of physical model testing being incurred.

In this work the free, open-source "interFoam" model has been validated for a variety of problems which are common in the assessment of wave structure interaction and the reliability of coastal structures such as flood defences or monopiles. It has been found that the model is suitable for modelling the propagation and transformation of waves and focussed wave groups in the near-shore region, the interaction of breaking waves and wave groups with surface-piercing structures and the modelling of wave transmission and decay through porous media such as sand and gravel fills as well as coarser, rock armouring using the Darcy-Forchheimer equation.

In this work the effects of turbulence have been neglected and the problem of determining appropriate estimations of inlet turbulence and appropriate turbulence modelling methodologies for the problems under consideration has been left for further research. Despite this, the simulations conducted using the model were found to produce good results for all the problems under consideration. A notable lack of research was identified into the problem of generating reasonable estimates for the turbulence in flow under waves in the near-shore region and in open-channel fluvial flows that is appropriate to the scale of modelling used in this work.

The interFoam model has been validated against several real experimental data-sets as part of this research. These include the Beji & Battjes (1993) results for wave propagation over a bar, the results from Aalborg

University for wave propagation and decay through porous media described by Troch (2000), as well as new data-sets generated during this research project for the propagation of waves over a submerged beach and the interaction of waves, focussed wave groups and breaking waves with a surface-piercing vertical cylinder (Zang *et al.* 2010).

As part of this work, new boundary conditions have been developed for the OpenFOAM library that allow for the simulation of first and second order regular waves and for the superposition of these regular waves to form focussed wave groups and irregular wave series. While there remain some practical issues with the use of these boundaries for long simulations relating not only to the computational effort required for simulations of significant length but also to numerical issues such as the simulation of Stokes' drift in the boundary condition, these boundary conditions have been made available for other researchers to use and have proven practical for a wide range of coastal applications.

Above all, the approach of using a vertical two-dimensional or three-dimensional CFD model to assess wave and flow parameters was found to be *practical* in both a design and an assessment context. This practicality of the model was demonstrated by applying the model in both a quantitative and qualitative manner to a real civil engineering case study: the design of a new coastal defence structure.

All of the computational modelling done as part of this research has been performed using only modest computational requirements. This has demonstrated that the approaches described in this thesis are available to practising engineers even in small companies without access to large and expensive clusters or super-computers.

# FURTHER WORK 7

## 7.1 Turbulence modelling

Several potential new research topics present themselves as a result of this work. Most critically this project has, as discussed above, neglected the effects of turbulence on the flow due to the high uncertainties associated with the turbulence parameters and the general lack of guidance in the literature as to the merits of the various turbulence approaches. The model described in this project should be investigated further with a view to determining which turbulence formulations are most appropriate to the problem of defence overtopping and breaching and developing some reasonable methods of approximating appropriate values of turbulence parameters on the boundary conditions. It has been found that there is very little guidance in the literature for the estimation of turbulence parameters in practical situations.

## 7.2 Mathematical methods and model benchmarking

This research has also neglected any detailed study of the underlying mathematics of the discretisation scheme, matrix solver and solution algorithm for the Navier-Stokes equations, focussing instead on broader practical aspects. Some basic tests that were conducted as an aside to this project have, however, suggested that the choice of these methods could have a significant effect on the run-time (and hence the practicality) of the simulations. One of the advantages of using a modular, highly-object-oriented software like OpenFOAM is that it is easy to switch out different solution methodologies and discretisation schemes without making any significant changes to the model code. This makes OpenFOAM a potentially very useful tool for the assessment of the relative computational efficiencies of different discretisation schemes and solution algorithms

as it allows only the mathematics under test to be changed while keeping the remainder of the code constant. A detailed benchmarking study comparing the relative merits of the different discretisation and solution approaches has the potential to greatly enhance the practicality of the methods discussed in this report.

## 7.3 Extension of the model to erosion

Many existing breach models, including those by Visser (1998) and, later Zhu (2006), consider erosion as the primary method of breach development, and it is widely accepted that the erosive action of the water plays a very important part in the development of a breach, after its formation. It is therefore important to consider accurate models for the erosion and transport of sediment as part of a breach model.

The incorporation of a simple erosion model into the interFoam code used in this thesis would be relatively straightforward. By using OpenFOAM's dynamic meshing capability it should be possible to make a boundary condition that moves the mesh vertices on the boundary downwards when a critical velocity or shear stress at the boundary is exceeded.

## 7.4 Incorporation of soil as a third phase

(de Medina 2008) considered the problem of sediment transport by attempting to model the soil using the Navier-Stokes equations and simply incorporating the solids as a third fluid phase. This requires some special treatment of the stress term in the equations as clearly the Newtonian Fluid assumption (equation 2.4) is quite inappropriate for the modelling of soil, even if the viscosity is increased. This can be dealt with, to a certain extent, by replacing this equation for the soil phase with a different rheological model that better represents the behaviour of the soil.

A second problem with this type of approach is that it introduces a very large discrepancy in the viscosity (several orders of magnitude) and this can reduce the stability of the model. However in soils where the water content is very high such as clays on sea and river beds, simulations are possible, although very small time-steps are required, rendering this approach very computationally expensive.

Further work on this approach would yield a potentially very useful approach to the problem of embankment breaching if an appropriate dis-

cretisation and numerical scheme could be found that allowed the model to run in a reasonable time.

## 7.5 Coupling with other models

Another direction in which further research could venture is into closer coupling with geotechnical models. As discussed in the introductory material, the long-term goal of this project is the modelling of the breaching process. The goal of such a model would be the calculation of a failure probability for an embankment or directly assessing a breach. Such an assessment could be performed by taking the deterministic hydraulic outputs produced using the methods discussed in this thesis and applying them to a probabilistic geotechnical model or even simply introducing a direct deterministic calculation of the soil dynamics into the OpenFOAM model. Both approaches have prospects for further research.

Additionally, as discussed in section 4.4, it is currently possible to directly couple the interFoam model to a simple linear-elastic stress model with a code known as "interFSIFoam". While this code is only in the early stages of development it may be possible to use it to reproduce the results in chapter 4 with the additional force peak caused by the natural resonance of the cylinder.

## 7.6 Boundary conditions

As has been highlighted in the results presented in chapters 3 and 4, some of the largest errors present in the results of the current model stem from inaccuracies in the wave-generating boundary condition. Several improvements suggest themselves, in particular:

- Implementation of a correction for Stokes' drift, either as a separate flow area in the boundary condition that subtracts the required volume from the model, or as a general correction to the inlet velocity field.

- The implementation of a scheme to allow the wave generating boundary to dynamically absorb reflected waves. Schemes such as AWAVOF go some way towards this and could be implemented, but would require extension as few are designed with wave generation boundaries that specify a spatially varying velocity field in mind.

- A sensitivity analysis to increasing the order of the wave equations applied at the boundaries. In particular, it would be useful to determine what practical benefit any increases in order would effect.

For boundary conditions in models for fluvial flow, it would be useful to implement dynamic linking between interFoam and other, simpler fluvial flow models such as ISIS or TUFLOW that could model the fluvial system as a whole. This would allow interFoam to be usefully applied to model complex fluvial structures such as bridges and weirs for which no accurate stage-flow relationship is available.

# A DINGEMANS TEST CASE RESULTS

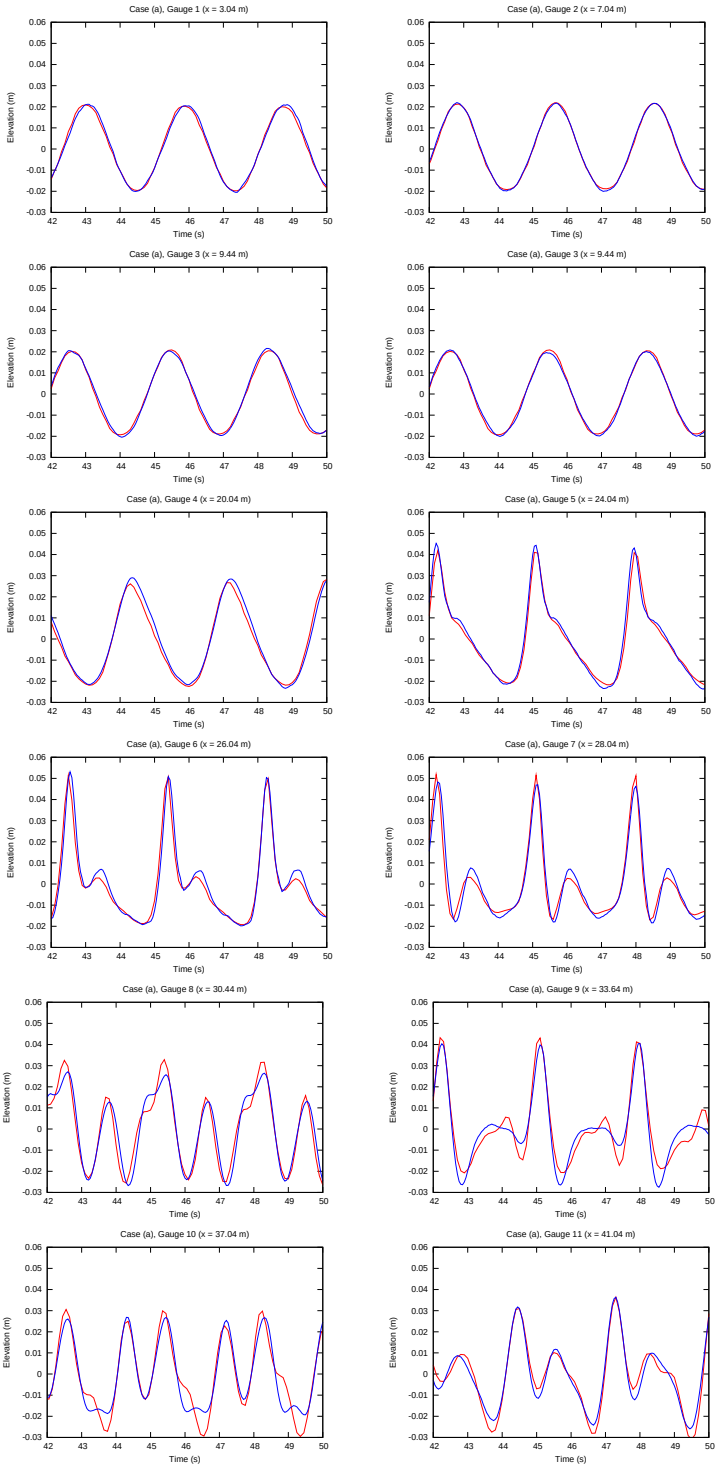


Figure A.1: Graphs showing the observed (blue line) and modelled (red line) elevation time series at each wave gauge for case A. Note that gauge 3 has two sets of experimental data available.

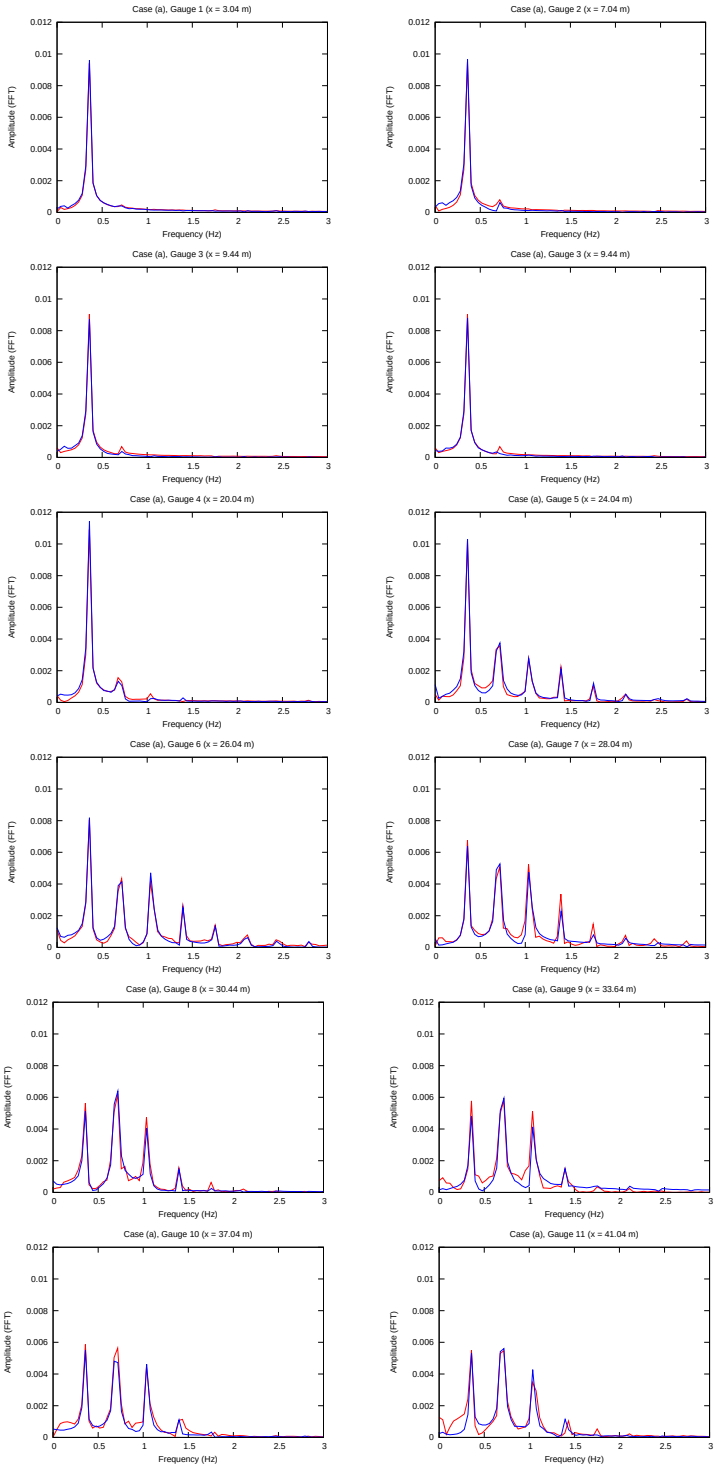


Figure A.2: Graphs showing the experimental (blue line) and modelled (red line) frequency spectra at each wave gauge for case A. Note that gauge 3 has two sets of experimental data available.

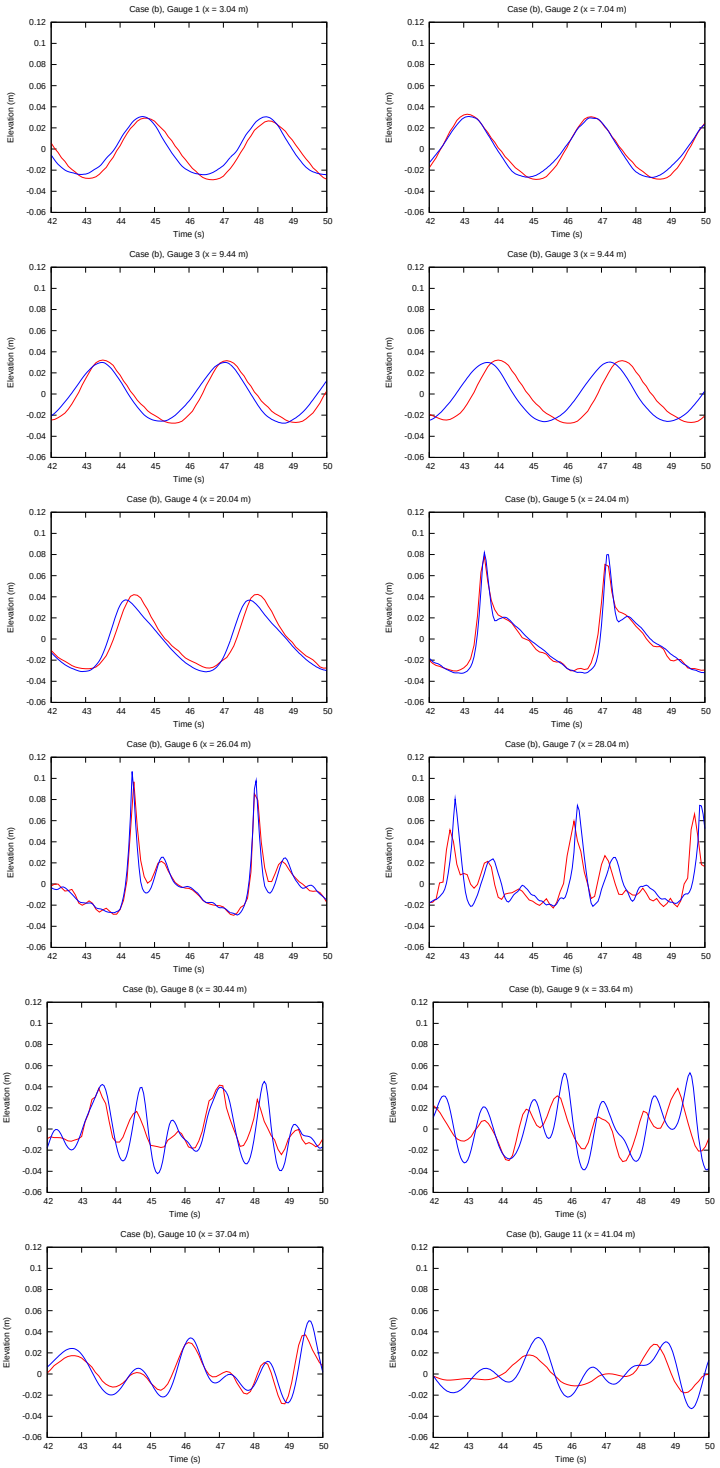


Figure A.3: Graphs showing the observed (blue line) and modelled (red line) elevation time series at each wave gauge for case B. Note that gauge 3 has two sets of experimental data available.

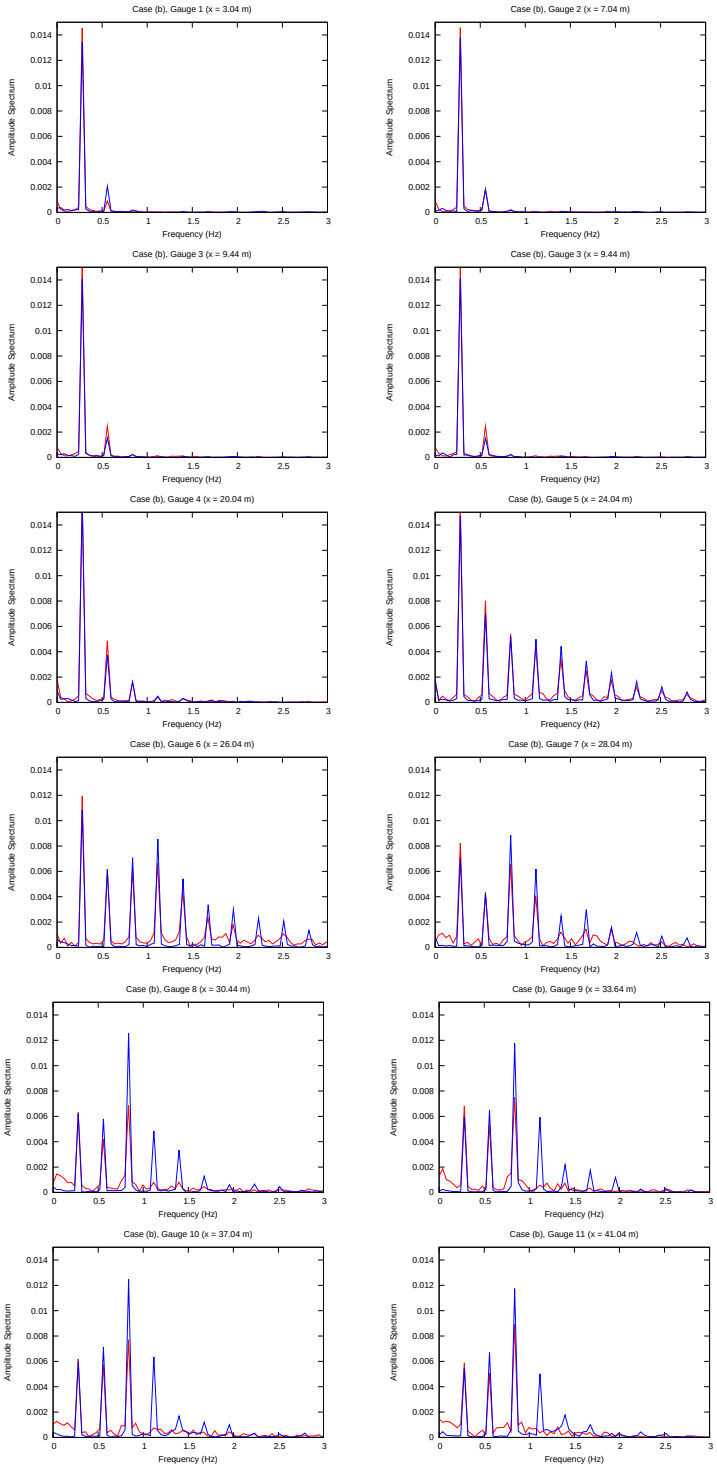


Figure A.4: Graphs showing the experimental (blue line) and modelled (red line) frequency spectra at each wave gauge for case B. Note that gauge 3 has two sets of experimental data available.

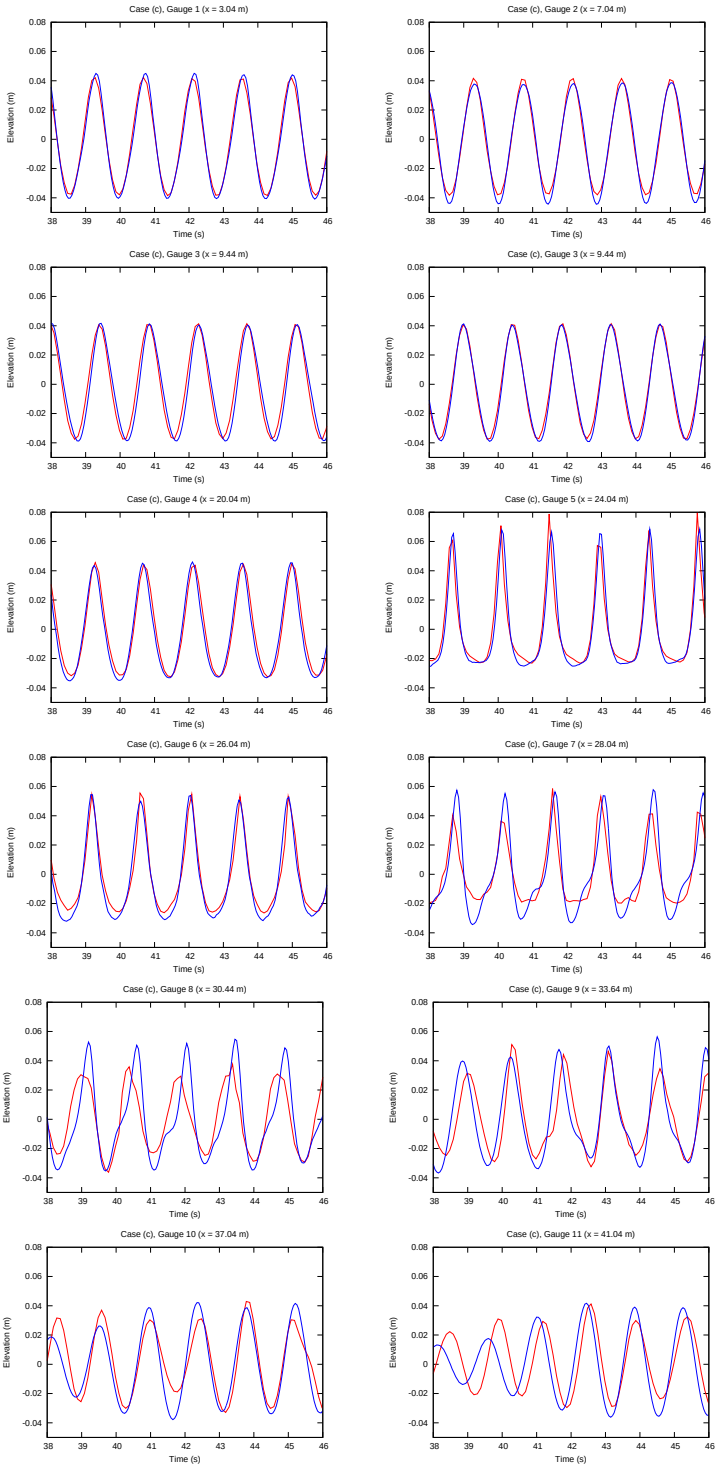


Figure A.5: Graphs showing the observed (blue line) and modelled (red line) elevation time series at each wave gauge for case C. Note that gauge 3 has two sets of experimental data available.

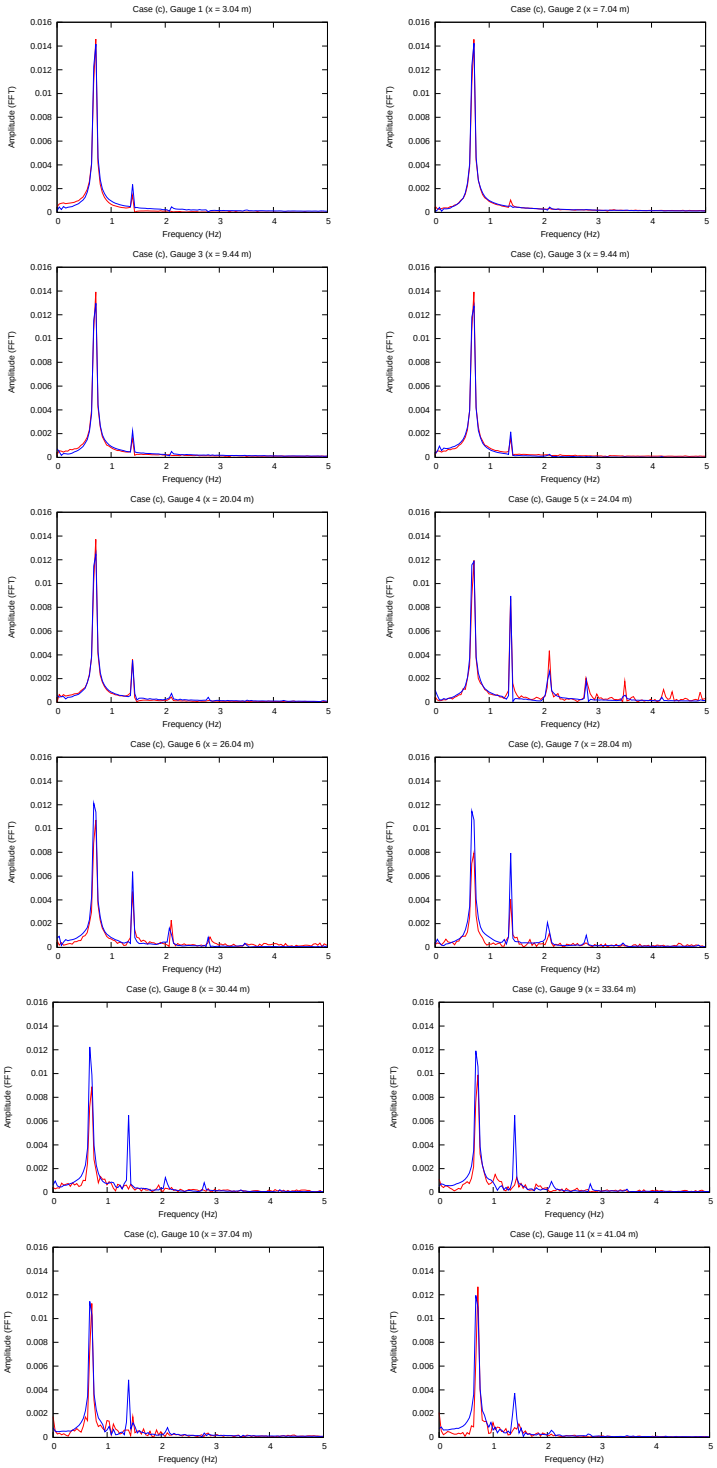


Figure A.6: Graphs showing the experimental (blue line) and modelled (red line) frequency spectra at each wave gauge for case C. Note that gauge 3 has two sets of experimental data available.

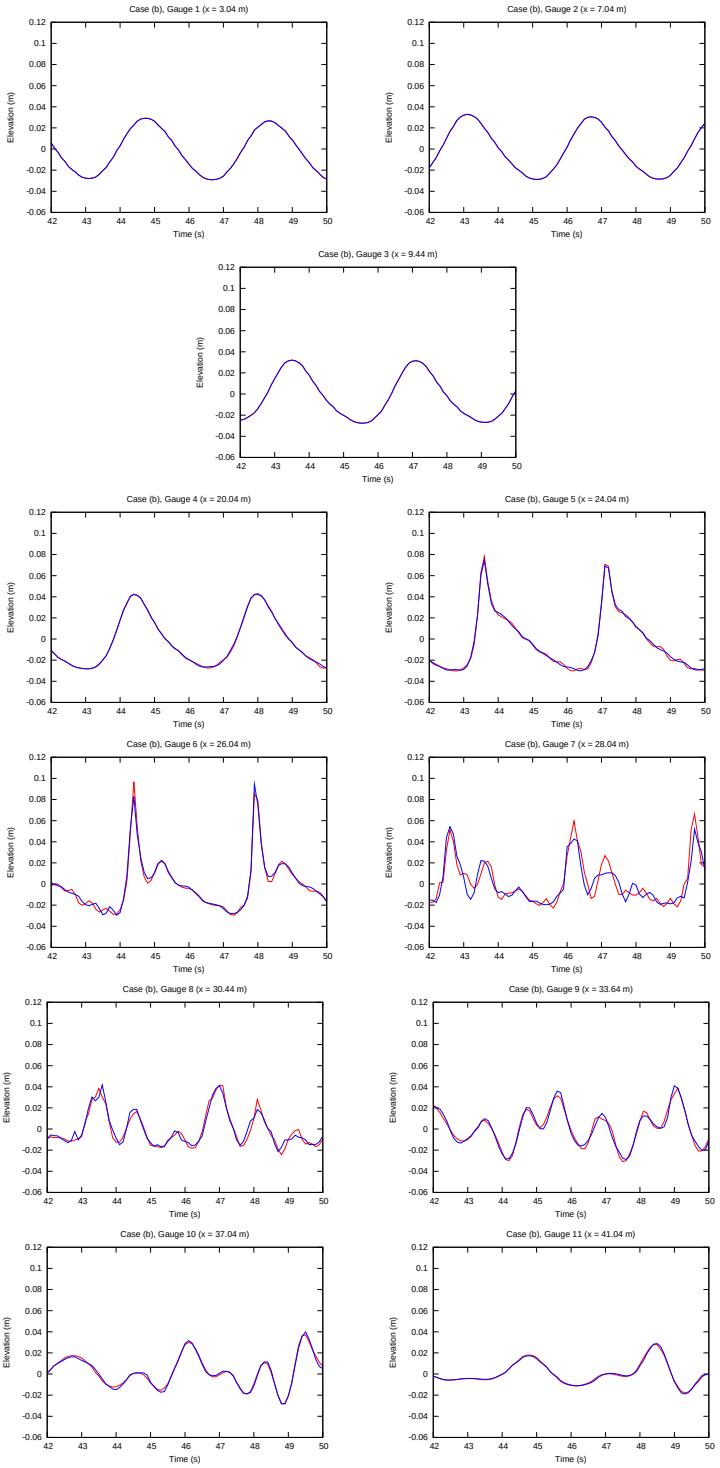


Figure A.7: Graphs showing modelled results using the linear scheme (red line) and cubic scheme (blue line).

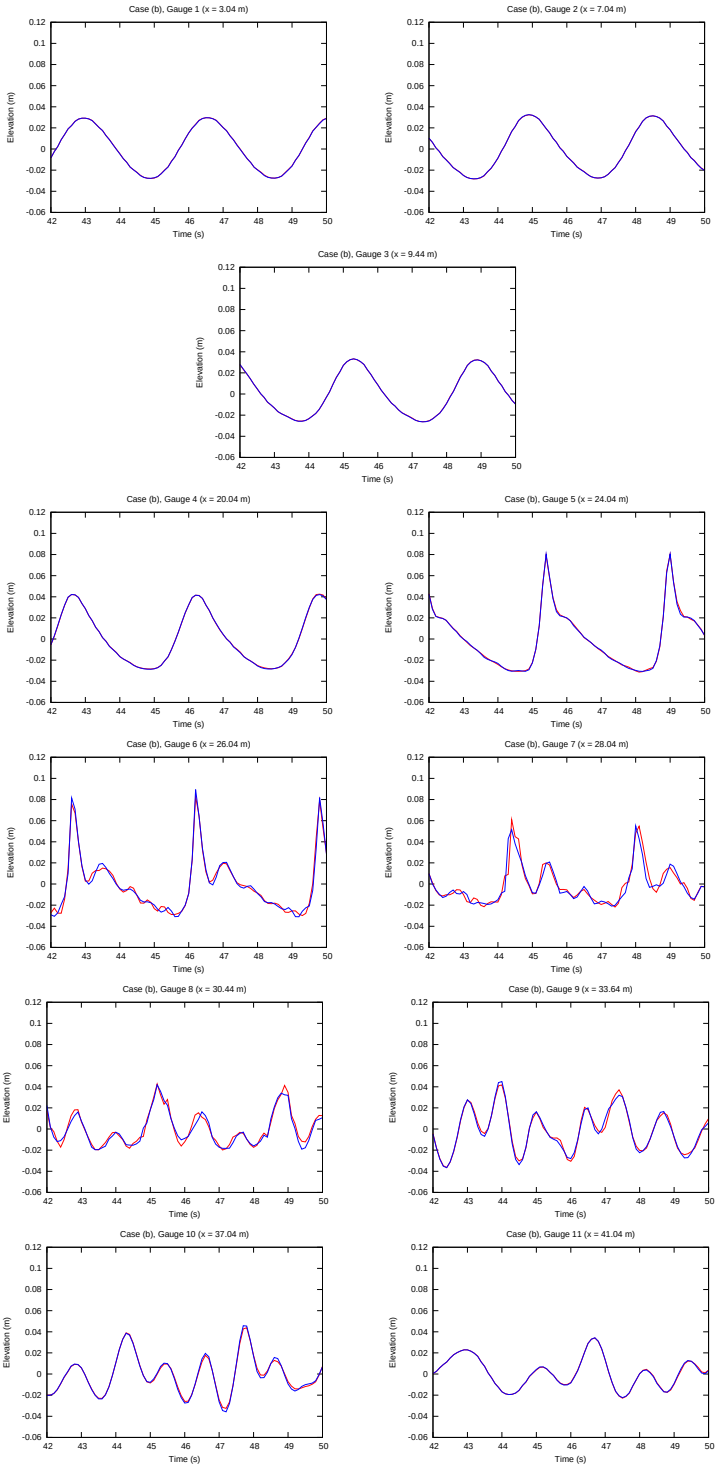


Figure A.8: Graphs showing modelled results without the momentum predictor (solid line) and with the momentum predictor (dashed line).

# B DHI Test Case Results

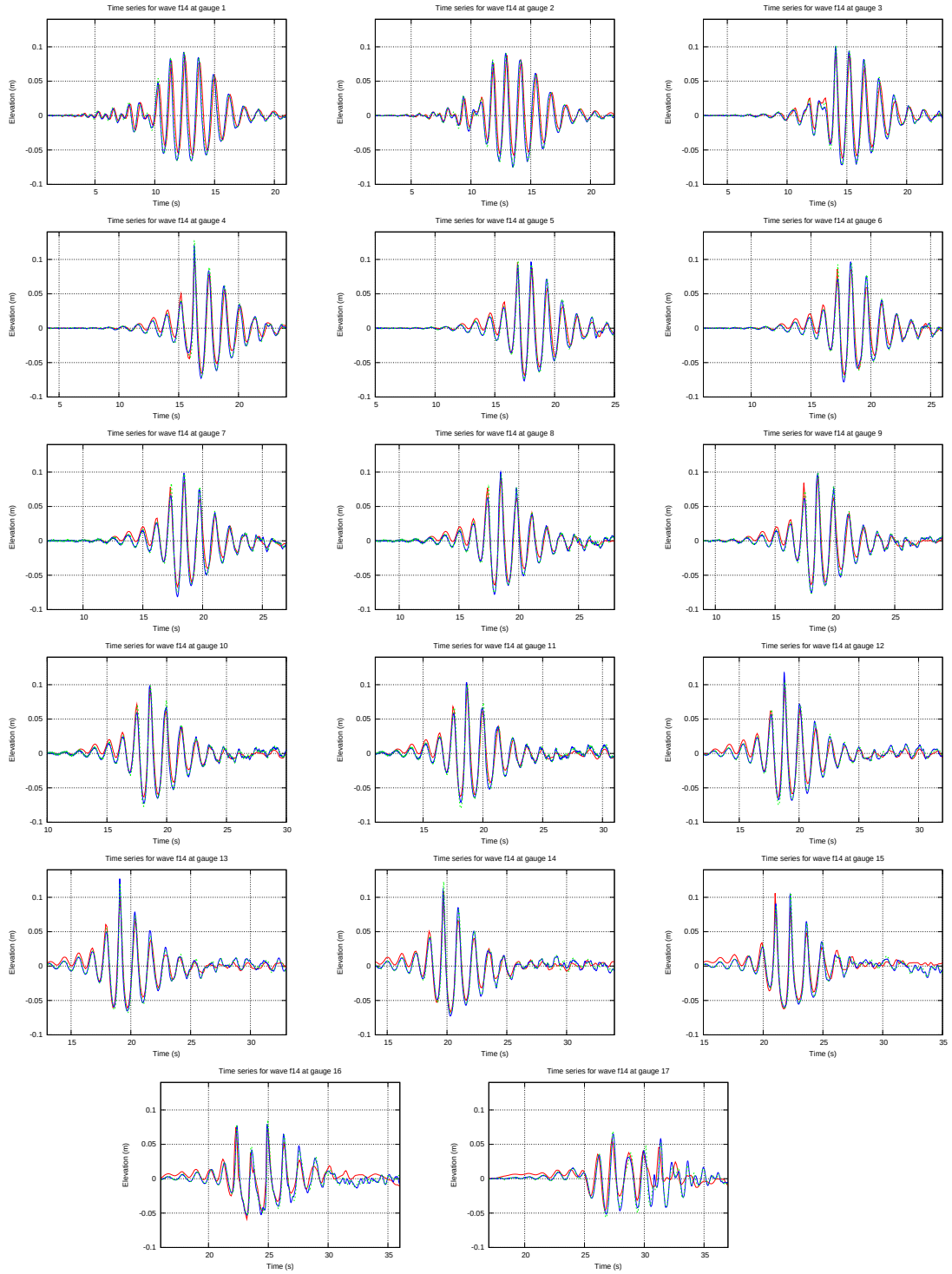


Figure B.1: Graphs showing the observed (dashed lines) and modelled (solid line) elevation time series at each wave gauge for case F14.

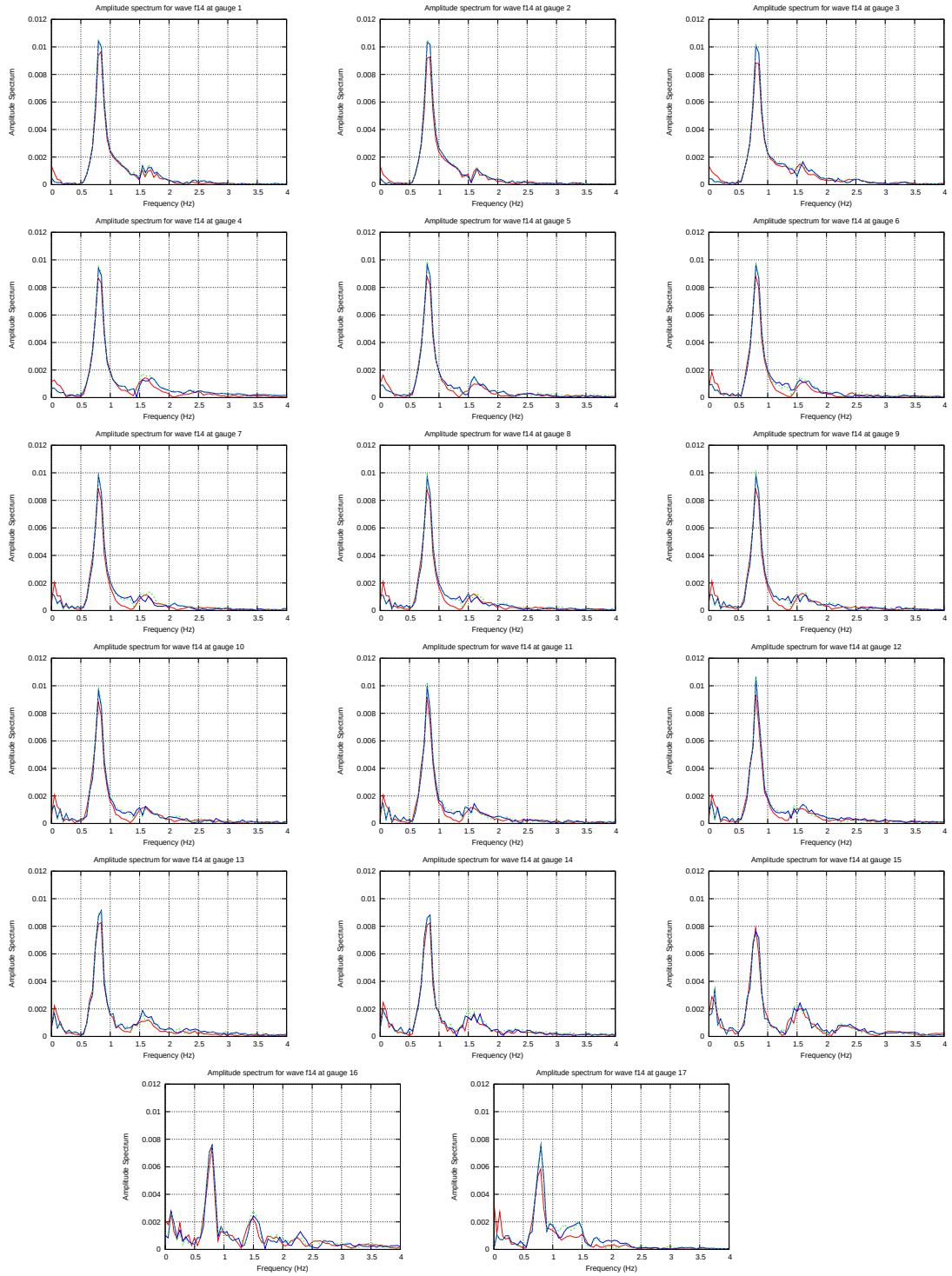


Figure B.2: Graphs showing the observed (dashed lines) and modelled (solid line) amplitude spectra at each wave gauge for case F14.

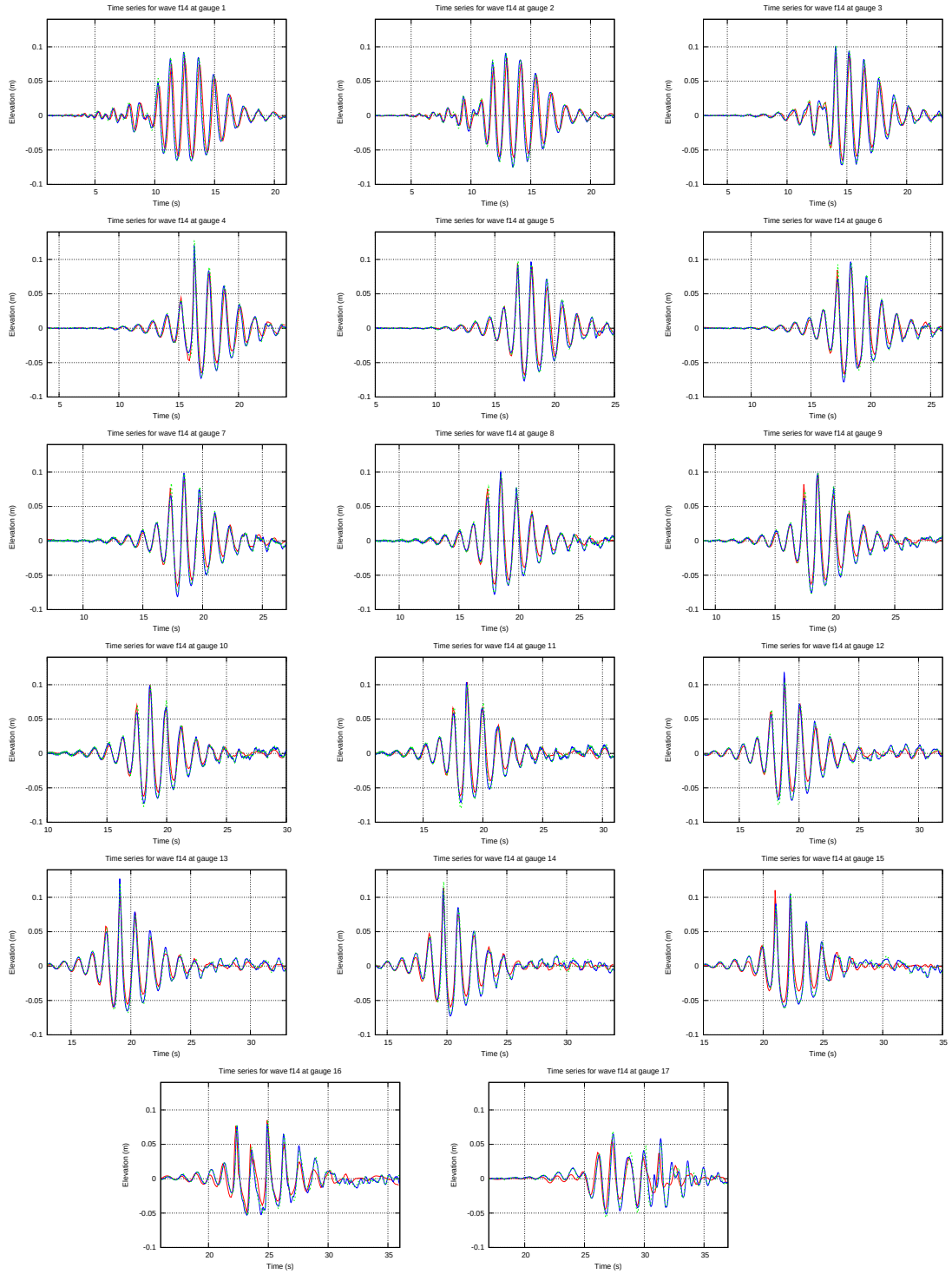


Figure B.3: Graphs showing the observed (dashed lines) and modelled (solid line) elevation time series adjusted for Stokes' drift at each wave gauge for case F14.

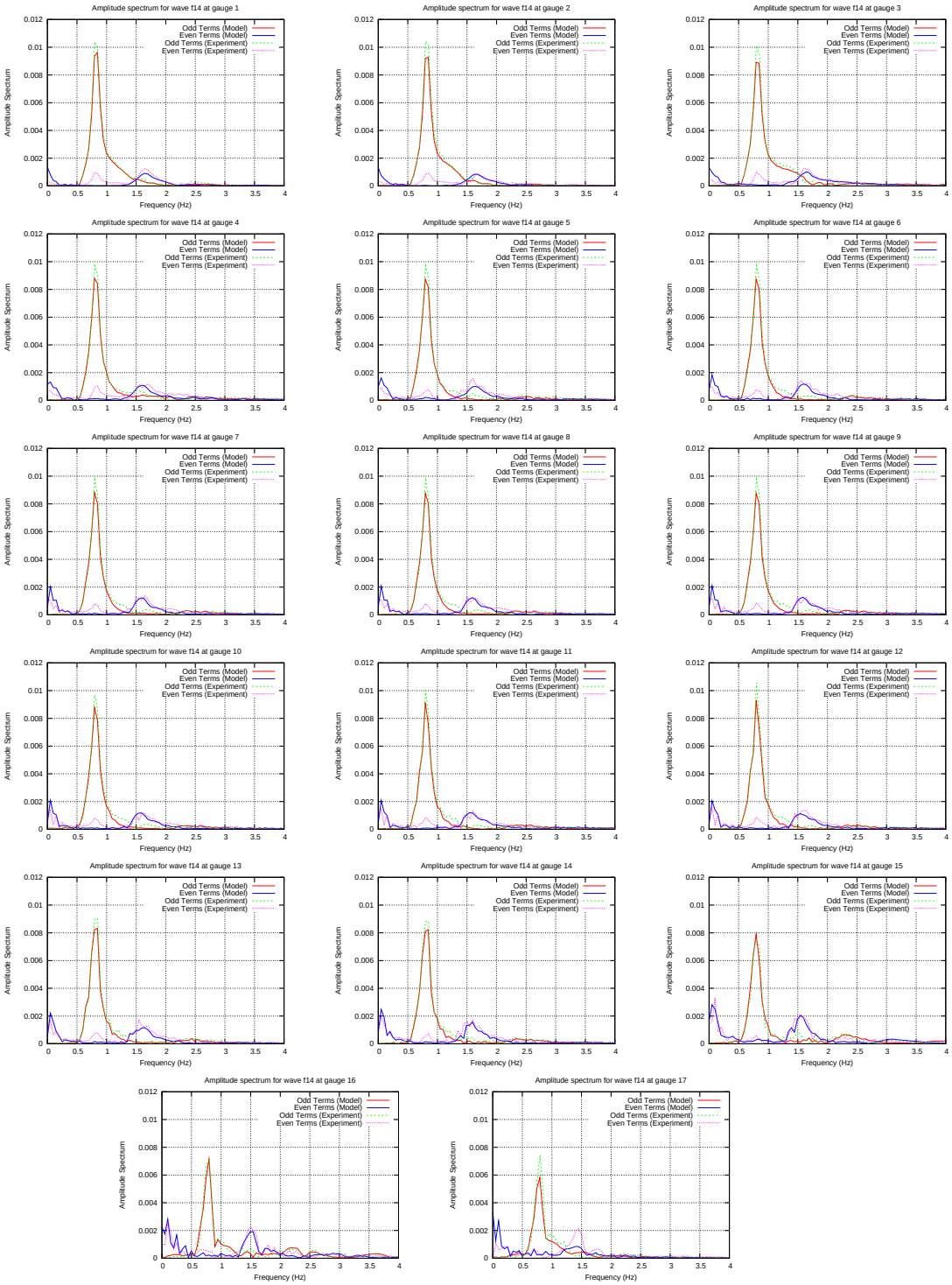


Figure B.4: Graphs showing the observed and modelled amplitude spectra at each wave gauge for case F14 decomposed into even- and odd-order terms.

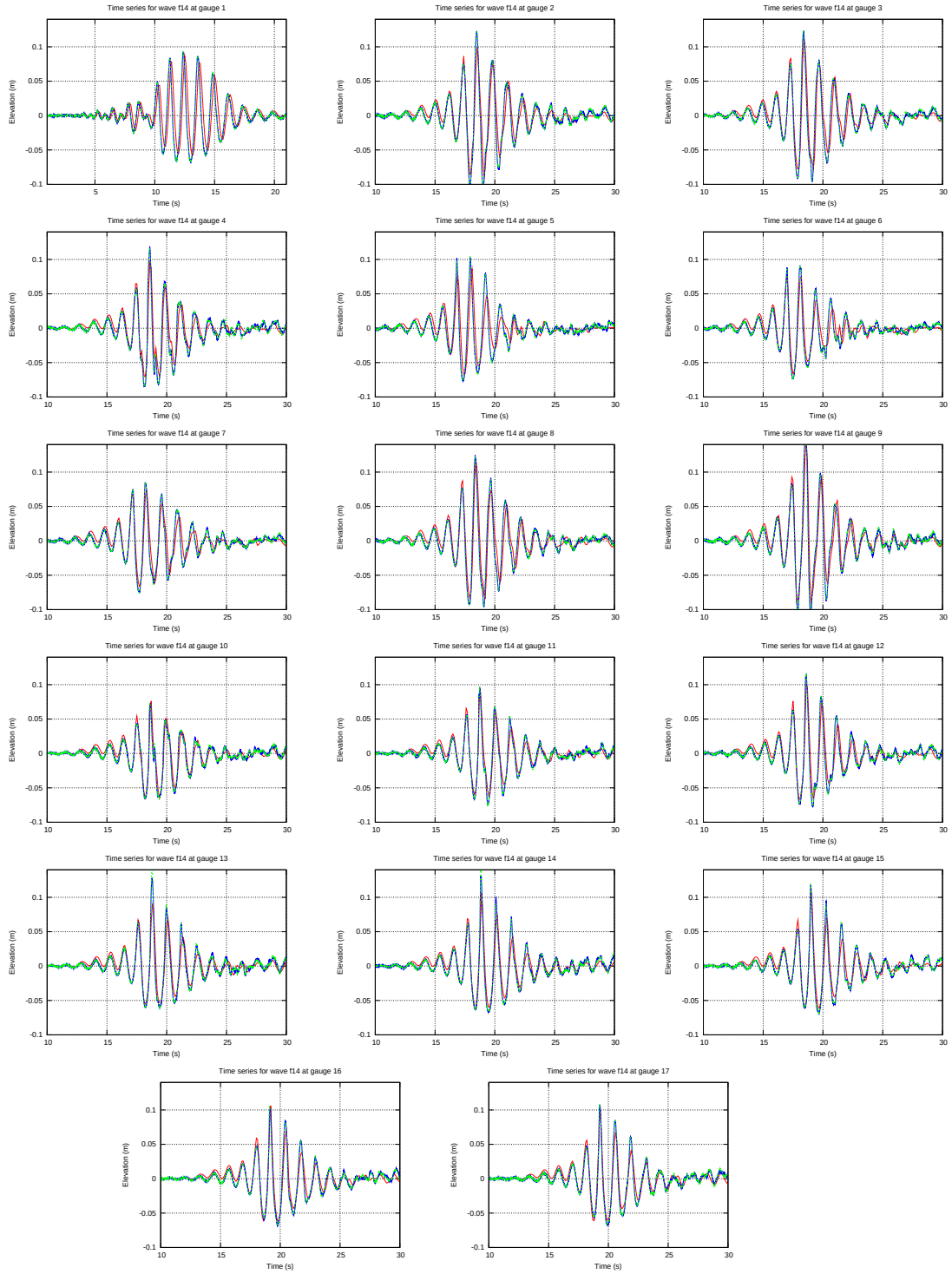


Figure B.5: Graphs showing the observed (blue and green lines) and modelled (red line) elevation time series at each wave gauge for case F14 with the beach and cylinder.

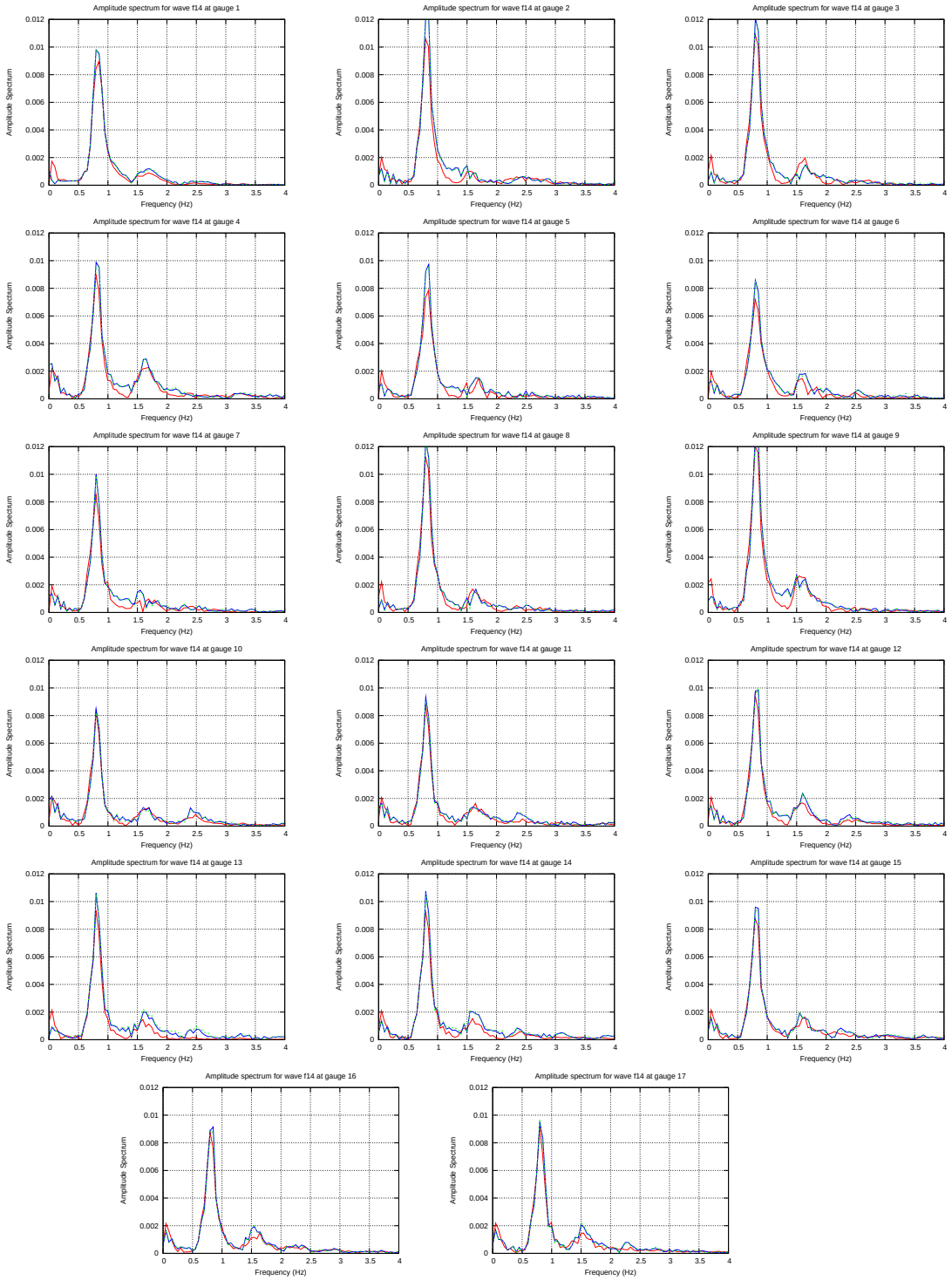


Figure B.6: Graphs showing the observed (blue and green lines) and modelled (red line) amplitude spectra at each wave gauge for case F14 with the beach and cylinder.

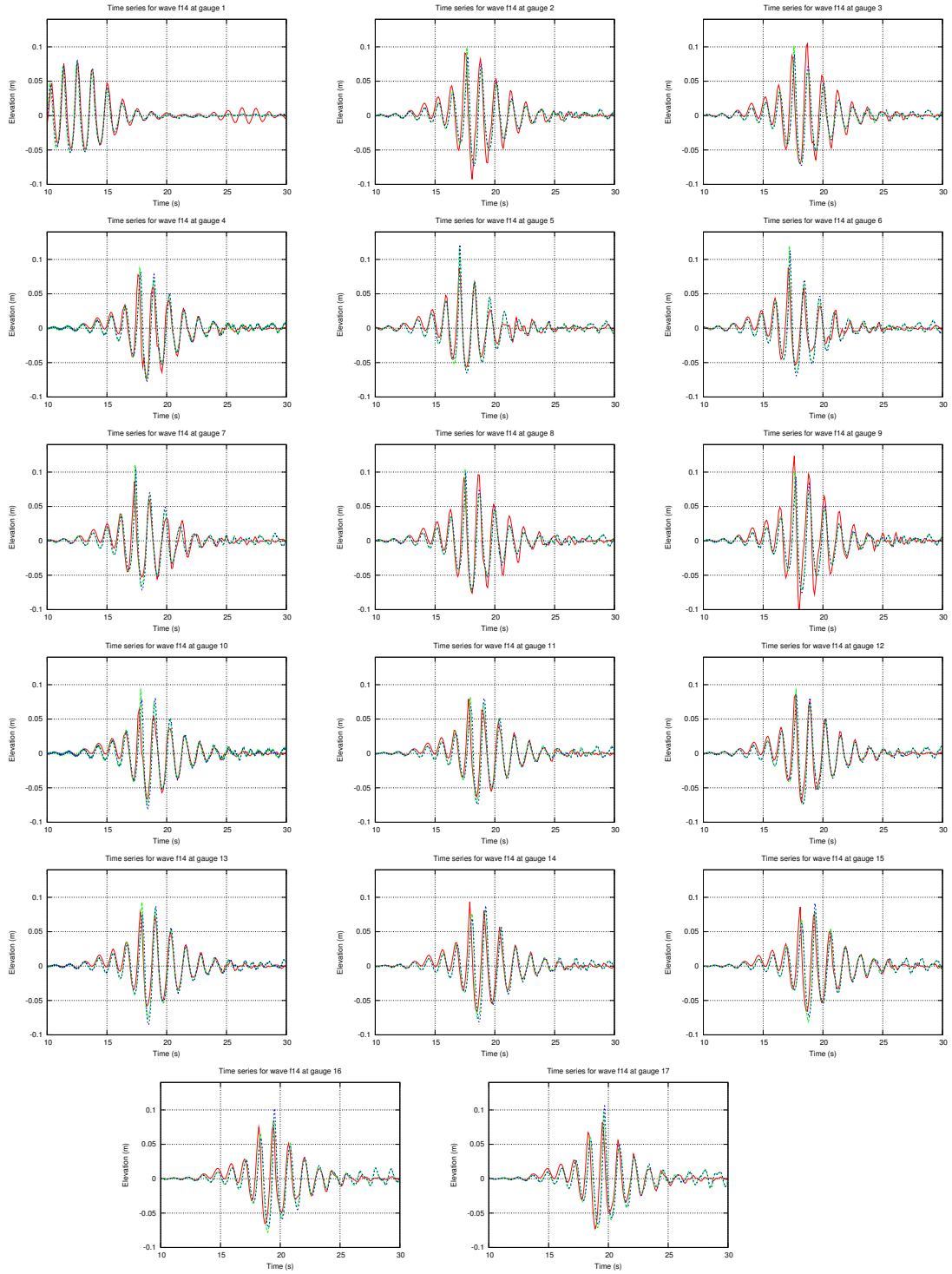


Figure B.7: Graphs showing the observed (blue and green lines) and modelled (red line) elevation time series at each wave gauge for case F14 with the cylinder on the flat bed.

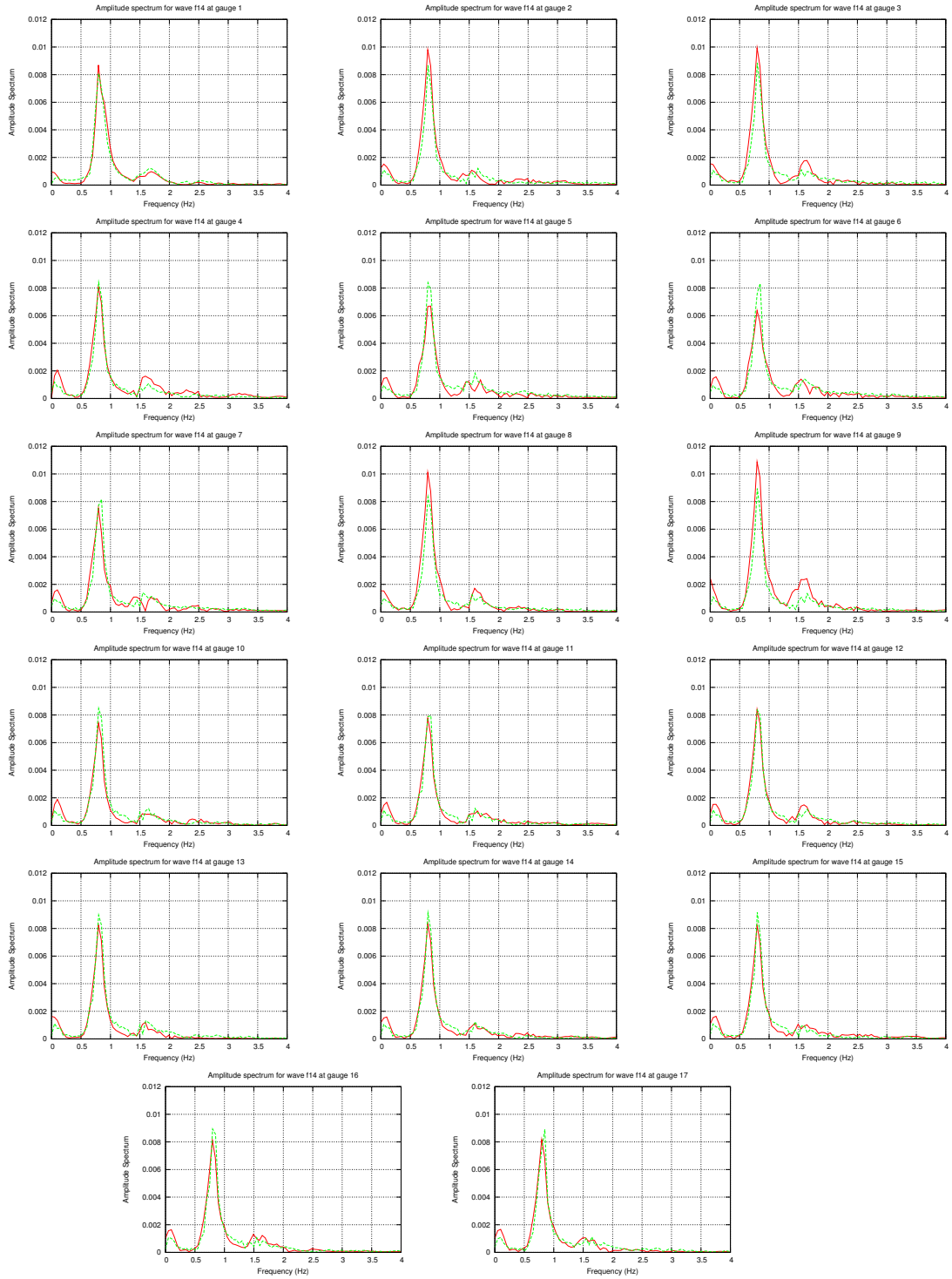


Figure B.8: Graphs showing the observed (blue and green lines) and modelled (red line) amplitude spectra at each wave gauge for case F14 with the cylinder on the flat bed.

# BIBLIOGRAPHY


Allsop, W.; Kortenhaus, A.; Morris, M.; Buijs, F.; Hassan, R.; Young, M.; Doorn, N.; van der Meer, J.; van Gelder, P.; Dyer, M.; Redaelli, M.; Utily, S.; Visser, P.; Bettess, R.; Lesniewska, D. & ter Horst, W. (2007). "Failure mechanisms for flood defence structures." Tech. rep., HR Wallingford.

Bardina, J. E.; Huang, P. G. & Coakley, T. J. (1997). "Turbulence modeling validation, testing and development." Tech. rep., NASA Ames Research Center. NASA Technical Memorandum 110446.

Beji, S. & Battjes, J. A. (1993). "Experimental investigation of wave propagation over a bar." *Coastal Engineering*, 19 151–162.

Berselli, L. C. & John, V. (2006). "Asymptotic behaviour of commutation errors and the divergence of the Reynolds stress tensor near the wall in the turbulent channel flow." *Mathematical Methods in the Applied Sciences*, 29 1709–1719.

Boccotti, P. (2000). *Wave Mechanics for Ocean Engineering*. Elsevier. ISBN 978-0-444-50380-0.

Buschmann, M. H. & Gad-el Hak, M. (2007). "Recent developments in the scaling of wall-bounded flows." *Progress in Aerospace Sciences*, 42 419–467.

Chadwick, A. J.; Morfett, J. C. & Borthwick, M. (2004). *Hydraulics in Civil and Environmental Engineering*. Taylor and Francis, 4 edn. ISBN 0415306094.

Dalrymple, R. A. & Rogers, B. D. (2006). "Numerical modelling of water waves with the SPH method." *Coastal Engineering*, 53 141–147.

de Medina, P. B. R. (2008). *Study and Numerical Simulation of Sediment Transport in Free-Surface Flow*. Ph.D. thesis, University of Malaga.

George, W. K. (2009). "Lectures in turbulence for the 21st century."

Gobbi, M. F. & Kirby, J. T. (1999). "Wave evolution over submerged sills: tests of a high-order Boussinesq model." *Coastal Engineering*, 37 57–96.

Gomez-Gesteira, M.; Rogers, B. D.; Dalrymple, R. A. & Crespo, A. J. C. (2010). "State-of-the-art of classical SPH for free-surface flows." *IAHR Journal of Hydraulic Research*, 48 Extra Issue 6–27.

Graf, W. H. (1971). *Hydraulics of Sediment Transport*. McGraw-Hill.

Greaves, D. M. (2007). "Viscous waves and wave-structure interaction in a tank using adapting quadtree grids." *Journal of Fluids and Structures*, 23 1149–1167.

Hafsteinsson, H. E. (2009). "Porous media in OpenFOAM." Tech. rep., Chalmers University of Technology.

Harlow, F. H. (1957). "Hydrodynamic problems involving large fluid distortions." *Journal of the Association For Computing Machinery*, 4 137–142.

Harlow, F. H. & Evans, M. W. (1955). "A machine calculation method for hydrodynamics problems." Tech. rep., Los Alamos Scientific Laboratory.

Harlow, F. H.; Evans, M. W. & Harris, D. E. (1956). "The Particle-in-Cell method for two-dimensional hydrodynamic problems." Tech. rep., Los Alamos Scientific Laboratory.

Head, K. H. (1982). *Manual of Soil Laboratory Testing. Vol 2: Permeability, shear strength and compressibility tests.* Pentech Press, 1 edn. ISBN 0727313053.

Issa, R. I. (1985). "Solution of the implicitly discretised fluid flow equations by operator-splitting." *Journal of Computational Physics*, 62 40–65.

Jeong, S. W.; Leroueil, S. & Locat, J. (2009). "Applicability of power law for describing the rheology of soils of different origins and characteristics." *Can. Geotech. J.*, 46 1011–1023.

Juretic, F. (2004). *Error analysis in finite volume CFD*. Ph.D. thesis, Imperial College, London.

Kothe, D. B. (1999). "Perspective on Eulerian finite volume methods for incompressible interfacial flows." Tech. Rep. LA-UR-97-3559, Los Alamos National Laboratory.

Kothe, D. B.; Mjolsness, R. C. & Torrey, M. D. (1991). "RIPPLE: A computer program for incompressible flows with free surfaces." Tech. rep., Los Alamos Scientific Laboratory.

Lara, J. L.; Losada, I. J. & Guanche, R. (2008). "Wave interaction with low-mound breakwaters using a RANS model." *Ocean Engineering*, 35 1388–1400.

Loehner, R.; Yang, C. & Oñate, E. (2007). "Simulation of flow with violent free surface motion and moving objects using unstructured grids." *International Journal for Numerical Methods in Fluids*, 53 1315–1338.

Losada, I. J.; Lara, J. L.; Guanche, R. & Gonzalez-Ondina, J. M. (2008). "Numerical analysis of wave overtopping of rubble mound breakwaters." *Coastal Engineering*, 55 47–62.

Mirtskhoulava, T. Y. (1988). *Basic physics and mechanics of channel erosion*. Tblisi. Translated by the author, 1991.

Morgan, G. C. J. (2008). *The solution of the depth-averaged equations of open channel flow in one-dimensional stream networks*. Master's thesis, University of Bath.

Morgan, G. C. J. & Zang, J. (2010). "Using the rasInterFoam CFD model for non-linear wave interaction with a cylinder." In *ISOPE2010, Beijing, China*.

Olivier, M. & Dumas, G. (2009). "Non-linear aeroelasticity for nano-air-vehicles applications using openfoam." In *4th OpenFOAM Workshop, Montreal, Canada*.

OpenCFD Ltd. (2008). *OpenFOAM Programmer's Guide, v. 1.5*.

Paterson, E. (2009). "Notes on the free-surface hydrodynamics special interest group discussions." Via personal communication.

Popinet, S. (2003). "Gerris: a tree-based adaptive solver for the incompressible Euler equations in complex geometries." *Journal of Computational Physics*.

Popinet, S. & Rickard, G. (2007). "A tree-based solver for adaptive ocean modelling." *Ocean Modelling*, 16 224–249.

Reis, M. T.; Neves, M. G. & Hu, K. (2009). "Wave overtopping of a porous structure: Numerical and physical modeling." *Journal of Coastal Research*, SI56 539–543.

Rusche, H. (2002). *Computational Fluid Dynamics of dispersed two-phase flows at high phase fractions*. Ph.D. thesis, Imperial College of Science, Technology and Medicine, University of London.

Sbalzarini, I. F.; Walther, J. H.; Bergdorf, M.; Hieber, S. E.; Kotsalis, E. M. & Koumaoutsakos, P. (2006). "PPM—A highly efficient parallel particle-mesh library for the simulations of continuum systems." *Journal of Computational Physics*, 215 566–588.

Schlatter, B. (1999). *A pedagogical tool using Smoothed Particle Hydrodynamics to model fluid flow past a system of cylinders.* Master's thesis, Oregon State University.

Seed, R. B.; Bea, R. G.; Abdelmalak, R. I.; Athanasopoulos-Zekkos, A.; Boutwell, G. P.; Briaud, J.-L.; Cheung, C.; Cobos-Roa, D.; Ehrensing, L.; Govindasamy, A. V.; Jr., L. F. H.; Inkabi, K.; Nicks, J.; Pestana, J. M.; Porter, J.; Rhee, K.; Riemer, M. F.; Rogers, J. D.; Storesund, R.; Vera-Grunauer, X. & Wartman, J. (2008). "New Orleans and Hurricane Katrina. I: Introduction, overview, and the east flank." *Journal of Geotechnical and Geoenvironmental Engineering*, pages 701–717.

Sidiropoulou, M. G.; Moutsopoulos, K. N. & Tsihrintzis, V. A. (2007). "Determination of Forchheimer equation coefficients $a$ and $b$." *Hydrological Processes*, 21 534–554.

TAW (1996). "Clay for dikes." Tech. rep., Technical Advisory Committee for Flood Defence (the Netherlands).

Temam, R. (2001). *Navier-Stokes equations Theory and numerical analysis*. American Mathematical Society. ISBN 0-8218-2737-5.

Troch, P. (2000). *Experimentele studie en numerieke modellering van golfinteractie met stortseengolfbrekers*. Ph.D. thesis, University of Gent.

Troch, P. & De Rouck, J. (1999). "An active wave generating–absorbing boundary condition for VOF type numerical model." *Coastal Engineering*, 38 223–247.

Tu, J.; Yeoh, H. H. & Liu, C. (2008). *Computational fluid dynamics: A practical approach*. Butterworth-Heinemann. ISBN 0750685638.

Ubbink, O. (1997). *Numerical prediction of two fluid systems with sharp interfaces*. Ph.D. thesis, Imperial College, London.

van der Meer, J. W.; Bernardini, P.; Snijders, W. & Regeling, H. J. (2006). "The wave overtopping simulator." In *ASCE, ICCE 2006, San Diego*.

Vanoni, V. A.; Brooks, N. H. & Kennedy, J. F. (1960). "Lecture notes on sediment transportation and channel stability."

Visser, P. J. (1998). *Breach growth in sand-dikes*. Ph.D. thesis, Technische Universiteit Delft.

Weller, H. G.; Tabor, G.; Jasak, H. & Fureby, C. (1998). "A tensorial approach to computational continuum mechanics using object-oriented techniques." *Computers in Physics*, 12, no. 6 620–631.

Westphalen, J.; Greaves, D. & Williams, C. (2007). "Comparison of free surface wave simulations using STAR CCM+ and CFX." In *10th Numerical Towing Tank Symposium, Hamburg, Germany*.

Zang, J.; Gibson, R.; Taylor, P. H.; Eatock Taylor, R. & Swan, C. (2006). "Second order wave diffraction around a fixed ship-shaped body in unidirectional steep waves." *J. Offshore Mech. Arct. Eng.*, 128, no. 2 89–99.

Zang, J.; Liu, S. X.; Eatock Taylor, R. & Taylor, P. H. (2009). "Wave run-up and response spectrum for wave scattering from a cylinder." *International Journal of Offshore and Polar Engineering*, 19, no. 3 183–188.

Zang, J.; Taylor, P. H.; Morgan, G. C. J.; Orszaghova, J.; Grice, J.; Stringer, R. & Tello, M. (2010). "Steep wave and breaking wave impact on offshore wind turbine foundations—ringing revisited." In *25th International Workshop on Water Waves and Floating Bodies*.

Zhu, Y. (2006). *Breach growth in clay-dikes*. Ph.D. thesis, Technische Universiteit Delft.